HERON is jointly edited by:
STEVIN-LABORATORY of the
faculty of Civil Engineering,
Delft University of Technology,
Delft, The Netherlands
and
TNO BUILDING AND
CONSTRUCTION RESEARCH.
Rijswijk (ZH), The Netherlands
HERON contains contributions
based mainly on research work
performed in these laboratories
on strength of materials, structures
and materials science.

ISSN 0046-7316

EDITORIAL BOARD:
A. C. W. M. Vrouwenvelder,
editor in chief
R. de Borst
J. G. M. van Mier
R. Polder
J. Wardenier

Secretary:
J. G. M. van Mier
Stevinweg 1
P.O. Box 5048
2600 GA Delft, The Netherlands
Tel. 0031-15-784578
Fax 0031-15-611465
Telex 38151 BUTUD

HERON vol. 36
1991
no. 4

Contents

AN EXPERIMENTAL STUDY OF SHEAR FRACTURE AND AGGREGATE INTERLOCK IN CEMENTBASED COMPOSITES

J. G. M. van Mier
M. B. Nooru-Mohamed
G. Timmers
Delft University of Technology
Department of Civil Engineering
Stevin Laboratory

Abstract 3
1 Introduction 5
2 Mode I and mixed mode I and II fracture of concrete 5
2.1 Non-linearities in mode I fracture 5
2.2 Mixed mode I and II fracture 10
2.3 Does mode II fracture exist? 14
3 Experimental technique 17
3.1 Biaxial test-rig 17
3.1.1 Loading frame 17
3.1.2 Load and displacement measurements . 23
3.1.3 Test control 27
3.1.4 Data acquisition system 28
3.1.5 Experimental problems 29
3.1.5.1 Influence of glue platens 29
3.1.5.2 Frame rotation 32
3.2 Specimens and materials 34
3.2.1 Plain concrete 34
3.2.2 Slurry infiltrated fibre concrete (SIFCON) 36
4 Plain concrete results 40
4.1 Introduction 40
4.2 Load-path description 42
4.2.1 Load-path 0: Uniaxial tension 42
4.2.2 Load-path 1: Shear at constant crack opening 45
4.2.3 Load-path 2: Tensile shear at zero axial load 45
4.2.4 Load-path 3: Unconfined and confined compressive shear 45
4.2.5 Load-path 4: Axial tension at constant shear force ... 45
4.2.6 Load-path 5: Axial tension at constant shear deformation 45
4.2.7 Load-path 6: Proportional loading 45

4.3 Influence of shear on the tensile envelope curve 46
4.4 Influence of crack opening on shear behaviour..... 50
4.4.1 Tensile shear..... 50
4.4.2 Compressive shear..... 52
4.5 Influence of confinement..... 55
4.5.1 Confinement normal to the crack plane 56
4.5.2 Confinement in the lateral shear direction..... 59
4.6 Size effect under biaxial loading 61
4.6.1 Size effect on strength 63
4.6.2 Load-path 4 results 65
4.6.3 Load-path 6 results 67
4.7 Path-dependency 71
4.8 Summary of failure modes..... 72

5 Shear fracture in SIFCON..... 74
5.1 Variables in the biaxial SIFCON experiments 74
5.2 Strength and ductility 76
5.3 Effect of fibre type 78
5.4 Effect of fibre orientation..... 79
5.5 Crack patterns..... 86
5.5.1 Shear cracks 87
5.5.2 Crack coalescence 88
5.5.3 Crack closure 91

6 Shear stiffness analysis..... 92
6.1 Comparison with aggregate interlock experiments 92
6.2 Shear stiffness reduction 95
6.2.1 Plain concrete..... 95
6.2.2 SIFCON..... 95
6.3 Shear retention factor..... 96

7 Conclusions 98

Acknowledgement 99

Notation 99

References 101

Publication in HERON since 1970

Abstract

In the present paper the results of an *exploratory* study with the recently developed biaxial tension/shear apparatus of the Stevin Laboratory of Delft University of Technology are presented. The apparatus is unique in the sense that square double-edge-notched concrete plates up to a size of 200 × 200 mm can be loaded in any combination of tension and shear in displacement control. The two loading axes are completely independent of one another. In the paper, both results of experiments on plain concrete and on slurry infiltrated fibre concrete (SIFCON) are presented.

The experiments can be divided into two main categories. In the first catagory, aggregate interlock has been studied for narrow cracks (between 10 and 400 μm) that can still transmit tensile loads normal to the crack plane. In the second catagory of experiments specimens were sheared off without precracking them (mode II), but in a few cases with simultaneous tensile loading (mixed mode I and II). The shear tests on specimens containing narrow cracks revealed an abundance of secondary cracking. The exact boundary conditions were very important here. Tests have been carried out with either zero confinement or with a very small confinement of − 1 kN perpendicular to the crack during shearing. Only for large crack openings, viz. larger than 200–250 μm, true sliding has been observed, and this seems to limit the range of applicabilty of the present aggregate interlock theories.

In the mode II tests in general a set of overlapping cracks would develop from the two notches in the specimen. This failure mode resembles the fracturing of four point shear beams with a narrow shear zone. Depending on the size of the specimen and the boundary conditions during shear, overlapping curved or straight cracks were found. A "true macroscopic shear failure", defined as an array of short inclined tensile cracks, was found in some proportional load-path tests ($\delta/\delta_s =$ constant) on plain concrete. Even then, this fracture mode could only develop when specimens were sufficiently small which implies that crack growth is very well confined. This type of failure was also obtained in tests on SIFCON, where shear cracks were found to develop in oriented weak planes between fibres in the specimen. The fact that distributed cracking was found in the small specimens (50 and 100 mm), but not in the larger 200 mm specimens, indicates that an unrestricted translation from results obtained in small specimens to large structures is not allowed. In fact this is the goal of many size effect laws that have been developed in the past. The biaxial test results were not in agreement with Bažant's size effect law, which may likely be explained from the shift in failure modes.

From the various load-path tests (in total 7 different load-paths were investigated), it was found that the behaviour of the specimens under biaxial loading is path dependent. In order to overcome the problems caused by path dependency, it is suggested to apply micro-mechanics models in order to come to a better understanding of the fracturing of the specimens and the intricate specimen/machine interactions.

As mentioned, a number of tension shear tests were carried out on SIFCON. Several researchers have suggested to use this material in structural engineering. The performance of the material in tension and compression is very good, leading to extremely ductile behaviour. The present tests showed however that the fracturing of SIFCON in shear is less favourable. The shear strength is rather small (viz. about 10–20% of f_{cc}) depending on the main fibre orientation with respect to the shear direction. The SIFCON is a rather anisotropic material, and oriented weak planes exist. Fracturing in these weak layers is easy, and macroscopic shear fractures were observed. For other fibre orientations, the performance is much better, and the response of the SIFCON resembles the behaviour of plain concrete with external confinement. The fibres can be regarded as an internal confinement in the case of SIFCON. It is concluded that a successful structural application of SIFCON will depend to a large extent on the ability of producing elements with isotropic fibre orientations.

Keywords: Testing, Biaxial Loading, Tension, Shear, Concrete, SIFCON, Mixed Mode I and II Fracture, Size Effect, Path Dependency, Aggregate Interlock, Mode II Fracture.

An experimental study of shear fracture and aggregate interlock in cementbased composites

1 Introduction

With the introduction of the Fictitious Crack Model for concrete fracture, much research has been devoted to the analysis of cementbased materials subjected to pure tension. In a sense this is a logical development because it represents the "simplest" fracture mode. However, in most structural applications pure tension (mode I) is an exception and in general combined tensile/shear stress states, or stated in fracture mechanics terminology mixed mode I and II fracture, prevails. The analysis of the sliding/friction mechanisms in concrete is a timely, but extremely difficult problem. Recent conferences (e.g. Shah et al. [1, 2], Elfgren and Shah [3], Van Mier et al. [4]) show that many researchers are active in the field, but at the same time it is clear that the main problem remains unresolved.
In the present study, a newly developed test technique at the Stevin Laboratory of Delft University of Technology has been used in an attempt to clarrify the shear/sliding mechanisms in various cementbased composites. Part of this work was done under an AFOSR contract (see acknowledgement), and the present paper contains the results of the extensive set of experiments that have been carried out on mortar, normal concrete, lightweight concrete and SIFCON (Slurry Infiltrated Fibre Concrete). After a short review of the literature (chapter 2), the experimental technique is described in chapter 3. The plain concrete results are the subject of a PhD thesis, Nooru-Mohamed [5], and the main results are included in this paper as well, chapter 4. For a better understanding of the shear/sliding mechanism, the experiments on SIFCON were quite helpful. These results are presented in chapters 5 and 6. Concluding remarks appear in chapter 7.

2 Mode I and mixed mode I and II fracture of concrete

This chapter contains a brief review of the state of the art on fracture mechanics of concrete, specifically mode I and mixed mode I and II fracture. Mode I results and models are included because the mixed mode situation cannot be considered independent of the mode I fracture.

2.1 *Non-linearities in mode I fracture of concrete*

The first attempts to apply fracture mechanics theories to heterogeneous materials such as concrete date back to the sixties, e.g. [6]. In these first attempts the applicability of linear fracture models to concrete was investigated. The main conclusion at that time was that the applicability of LEFM was restricted to hardened cement paste only, which, by its nature is a very homogeneous material (at the macro-scale). For mortar and normal concrete it was concluded that LEFM is *not* applicable.

Several years later, the fictitious crack model was presented by Hillerborg and co-workers [7]. Because of the heterogeneous nature of the material it was argued that a "zone of discontinuous microcracking" advances in front of a visible continuous crack as depicted in Fig. 1. This implies that the stress-redistributions do not occur conform LEFM theory, but more energy will be dissipated in the fracture process. The fracture toughness of the material increases due to the presence of the microcracks. Petersson [8] suggested that the best method for determining the fracture energy of heterogeneous materials such as concrete is a displacement controlled uniaxial tension test.

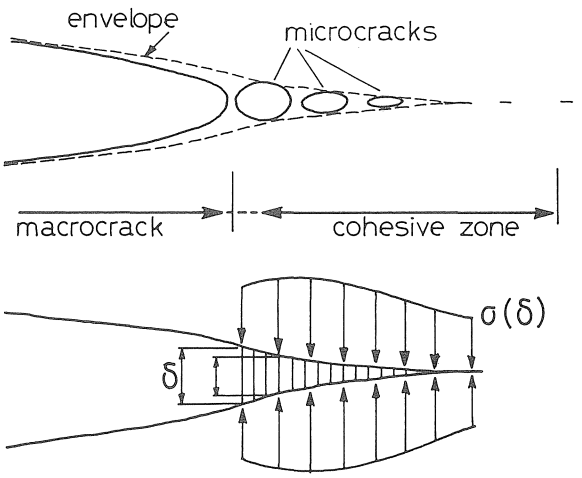

Fig. 1. Classical definition of a process zone in concrete: (a) microcracks advancing a continuous macrocrack, (b) and closing pressure over the cohesive zone.

Specified conditions for such a test are that the specimen should not be too large and that the test should be carried out between parallel end-platen. In Fig. 2, the tensile apparatus as available in the Stevin Laboratory is shown. In this approach it was tried to generate a uniform microcrack zone in a double notched specimen. The stress-crack width diagram obtained from a test contains all necessary information to determine the fracture energy per unit fracture surface [9].

A main problem of the Fictitious Crack Model (FCM) is that the physics of the fracture process are not taken into account in an adequate manner. In effect the assumed *"zone of discontinous microcracking in front of a macroscopic and continuous crack"* is taken into account by assuming a fictitious crack length. The crack propagation criterion in the FCM is the exceedence of the tensile strength of the material. Note that LEFM has been modified along similar lines in the past few years, with the difference that the singularity at the crack tip is maintained in the LEFM based effective crack models (see for example [10]).

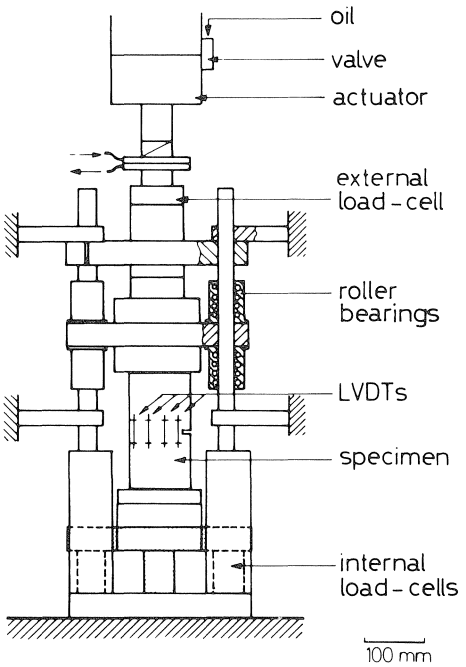

Fig. 2. Set-up for deformation controlled uniaxial tensile testing in the Stevin Laboratory.

An extensive survey of the literature by Mindess [11] showed that there is much controversy about the extent and true nature of the process zone (following the above definition) in concrete. Process zone sizes of a few micrometer to 500 mm have been reported. Furthermore, the size of the process zone seemed to depend to a large extent on the resolution of the measuring technique but also on the structural conditions under which it can develop, i.e. stress gradients. At the fracture conference in Vienna in 1988, Van Mier and Nooru-Mohamed argued that the non-linearities in the fracturing of concrete could be explained from a two stage fracture process, which depends to a large extent on the geometry of the test specimen [12]. In their tests it was shown that overlapping crack tips could explain the long stable tail of the softening diagram in the stress-crack opening diagram, see Fig. 3. This would imply that no such thing as a "zone of discontinous microcracking ahead of a continuous macrocrack" would exist. In 1990 Hu and Wittmann [13] showed, by using the so-called double cutting technique developed in the field of ceramics, that the additional toughening in cracks in concrete should be explained by some process taking place in the wake of the visible crack. However, the double cutting technique does not allow for an accurate measurement of the mechanism, and two options are possible: (1) the crack front is non-uniform over the depth of the specimen, or (2) frictional interlock or bridging takes place in the macrocrack. The first mechanism, viz. non-uniform crack fronts, was found by Bascoul and coworkers [14] and later confirmed by others (e.g. [15, 16, 17, 18]). The non-uniform crack fronts were found by impregnating cracked specimens. The tests carried out by

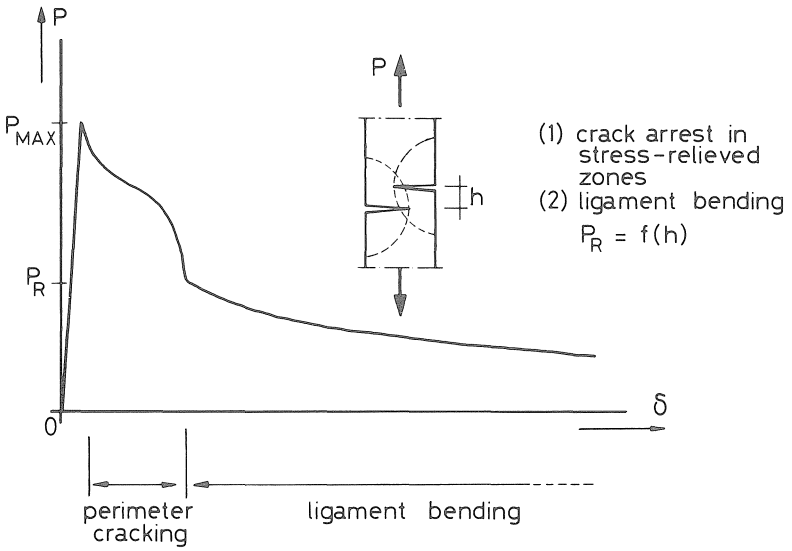

Fig. 3. Fracture mechanism in uniaxial tension, After [12].

Bascoul et al. and Swartz and Refai [15] were three point bend tests. In these experiments the specimens were impregnated under loading, and thereafter fractured completely. By using coloured dye, the shape of the crack front could easily be determined as shown in Fig. 4. Van Mier [16] used a vacuum impregnation technique to visualize cracking in prismatic specimens loaded in uniaxial tension up to a prescribed average axial crack opening. After impregnating the cracked specimen with a fluorescenting epoxy, the specimen was sawn into six slices (Fig. 5) and the internal cracking could be studied under UV light. Up to axial crack openings of 50 μm, the crack fronts were non-uniform. At larger crack openings, the specimens were completely cracked, but still some load could be transfered. In Fig. 6 the extent of internal cracking in a specimen loaded up to 100 μm average axial crack opening is shown. The load carrying capacity can be explained from crack face bridging, which manifests itself mostly in the form of

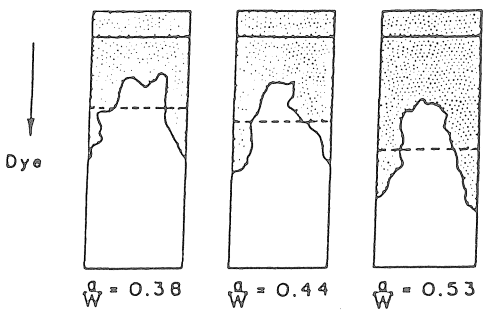

Fig. 4. Non-uniform crack fronts in plain concrete beams, after [15].

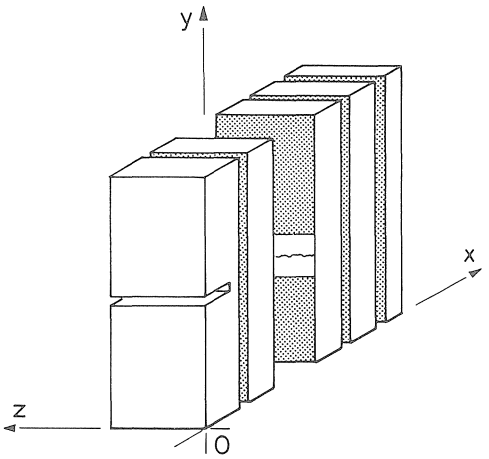

Fig. 5. Slicing prismatic specimens for internal crack detection after loading the specimens in uniaxial tension and vacuum impregnating the cracked specimen. Identification of internal crack detection planes yz through coordinate x, after [16].

two overlapping crack tips with an intact ligament in between. Crack face bridging in three different concretes is shown in Fig. 7. The two overlapping crack tips shield each other, and the fracture of the ligament between the overlapping cracks is a very stable process. Recently the failure of a ligament was followed in a specimen under load [19], and a strong correlation between the size of the crack face bridges and the load carrying capacity of a concrete with a given maximum aggregate size has been found [18].

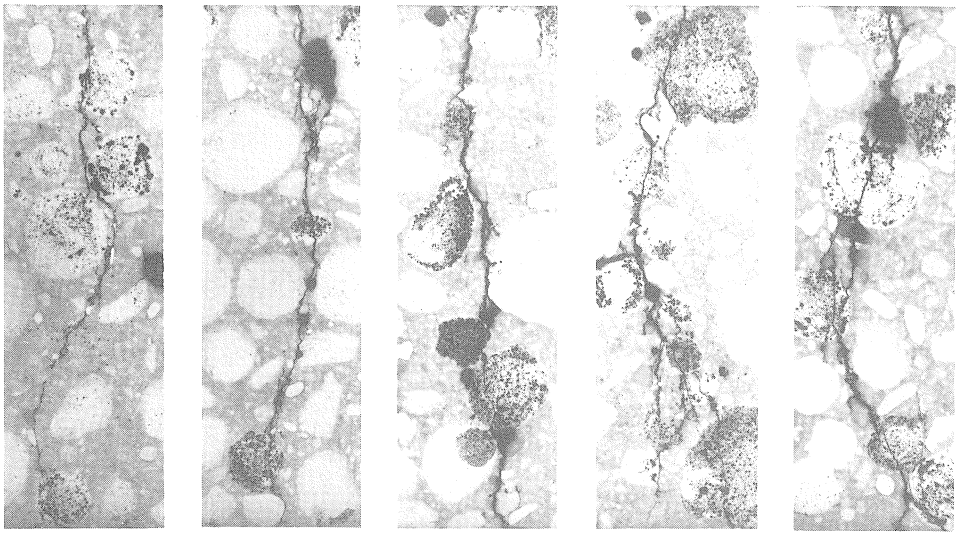

$x = 22.5$mm 37.4 52.3 67.3 82.1

Fig. 6. Internal cracking in a lytag specimen, loaded in tension up to an average axial deformation of 100 μm. The locations of the surfaces are indicated with an x-coordinate (see Fig. 5), after [16].

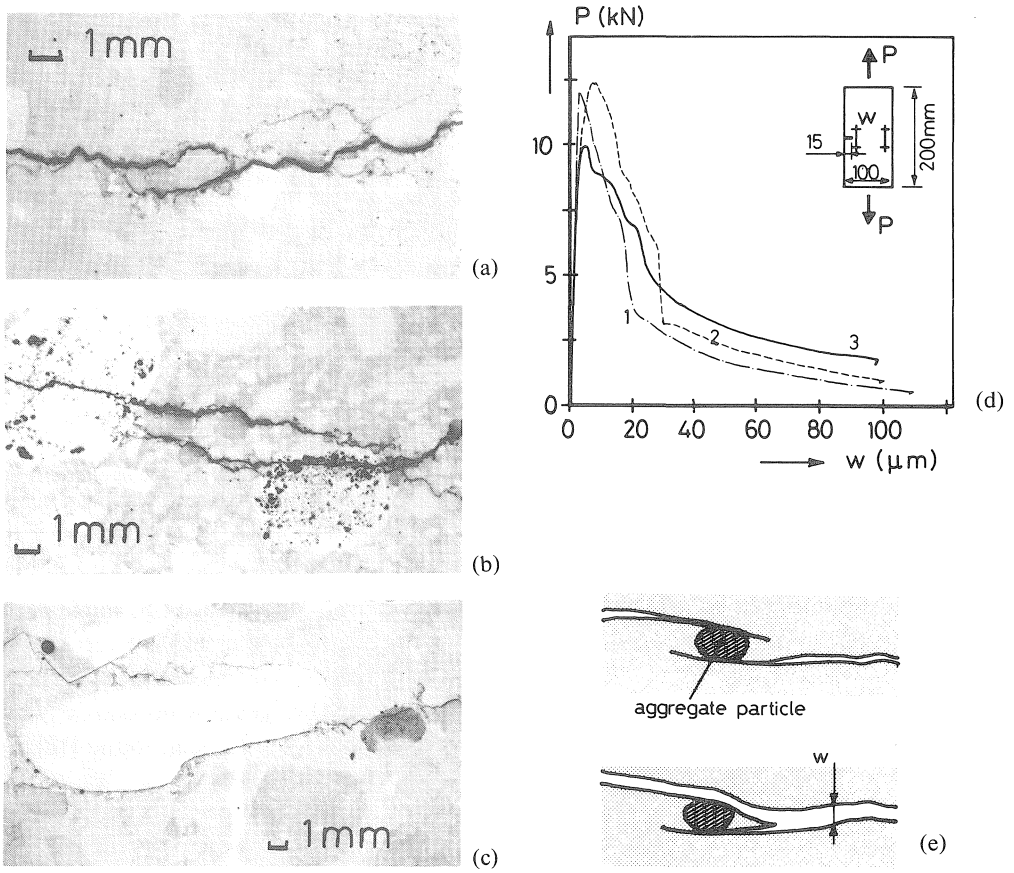

Fig. 7. Crack face bridging at $\delta = 100$ μm for respectively 2 mm mortar (a), 12 mm lytag (b), 16 mm normal concrete (c); P-δ diagrams (d), and bridge failure mechanism (e), after [17, 19].

The typical shape of the crack face bridges, i.e. two overlapping crack tips, which generally develop around stiff aggregates, was recently simulated in a numerical micromechanics model for fracture of concrete, see Schlangen and Van Mier ([20] and Fig. 8). The overlapping crack tip mode was found to be a natural consequence of the heterogeneity of the material. The individual crack branches tend to avoid each other. Similar results were recently also obtained by Vonk et al. [21].

2.2 *Mixed mode I and II fracture*

Most cracks in concrete structures develop under combined modes, and mixed mode I and II (tension and in-plane shear) loading seems to prevail. In LEFM criteria for mixed mode I and II fracture have been proposed, but many of the models have been developed for metals. Criteria for composites are gradually emerging, see for example

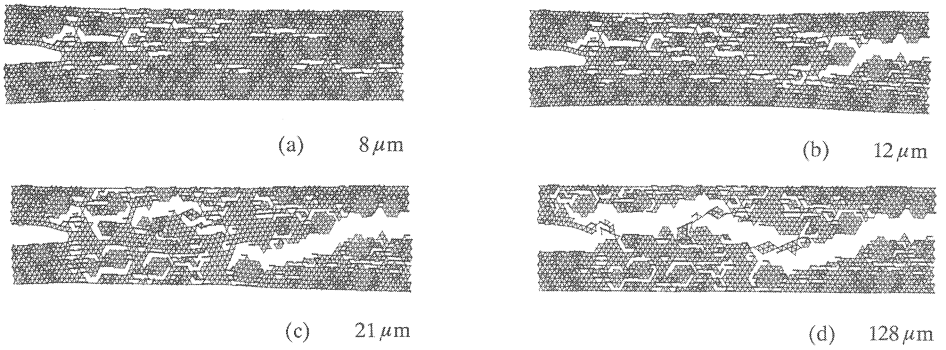

Fig. 8. Simulation of crack face bridging using a simple lattice model [20]. Four stages of crack growth are shown at different axial crack openings. The results are in good agreement with the experiments of Fig. 7.

Gdoutos 1984 and Carpinteri and Swartz, 1991 [22, 23]. Of course the main problem for concrete is its heterogeneity. As shown in the previous section, mode I fracture is a highly non-linear phenomenon, and this will undoubtedly have some effect on mixed mode situations as well.

Many of the attempts to develop a mixed mode criterion for concrete are in effect extensions of mixed mode criteria in LEFM. Many researchers have attempted to develop a specimen where a mode II component is present in the uncracked state, and generally the design of a specimen is based on a linear elastic analysis of the proposed geometry. An extensive review of existing geometries is given in Hordijk, Van Mier and Reinhardt, 1989 [24], see Fig. 9a; additional geometries can be found in [4]. In many

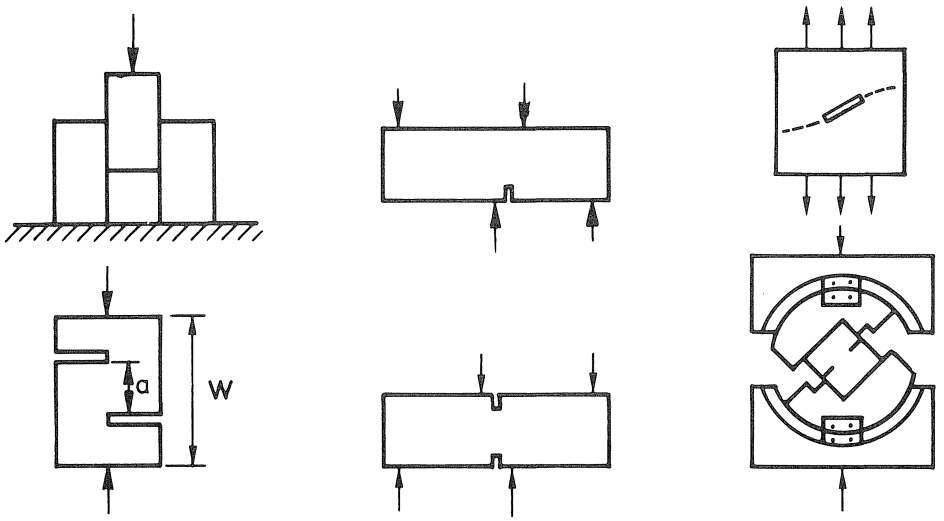

Fig. 9a. Various specimen geometries and loading configurations for mixed mode I and II and mode II testing of concrete [24].

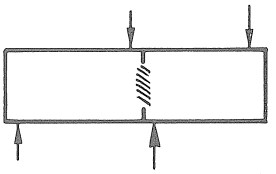

Fig. 9b. Mode II (shear) crack in a four point shear specimen with narrow shear zone, after [25].

cases it has been found that cracks initiate in mode I, and that a true mode II mechanism could not be obtained. This can probably be explained from the fact that cracks initiate near stress concentrations caused by the heterogeneous material structure. The draw back of designing mixed mode I and II specimens or mode II specimens on basis of linear analyses of the uncracked state is that as soon as a small crack develops severe stress-redistributions occur. The new stress state may deviate considerably from the linear state.

Mode II or shear cracking is the limit case when no tensile stresses are present. Bažant and Pfeiffer [25] claimed that they observed pure mode II fracture, defined as an array of inclined tensile cracks (Fig. 9b), in double edge notched four point shear tests of concrete. The results are considered rather controversial. For example, Ingraffea [26] suggested that the failure mode in Bažant and Pfeiffers tests is not correct and that rather a splitting type of failure must have occurred as shown in Fig. 10. Indeed, under carefully controlled conditions, the predicted failure mode by Ingraffea was observed

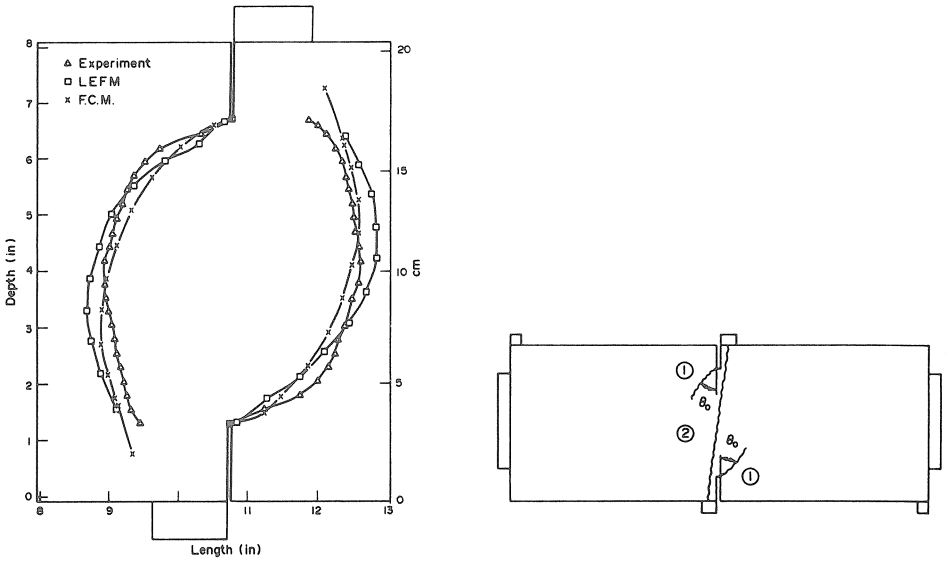

Fig. 10. Primary cracking and fatal splitting crack in four point shear specimen with narrow shear zone, [27]: (a) without and (b) with axial force.

by Swartz and Taha [27]. Again this demonstates that it is not straightforward to obtain mode II fracture in concrete, and one may be misled when not carefully controlled experiments under pure boundary conditions are carried out.

It seems that most structural situations are governed by mode I crack initiation and propagation. If mode I fracture prevails, shear may become important only after a crack has developed. The research should then focus on the effect of friction in cracks. Carpinteri [28] measured that a 30% increase of fracture energy occurs under mixed mode loading. These results were derived from tests on single edge notched four point shear beams. Again the effect of boundary conditions was underestimated by Carpinteri, and Schlangen and Van Mier [29, 30] showed that the increase of fracture energy under mixed mode loading could be traced back to friction in the supports in Carpinteri's experiments. When the four point shear beam is loaded between "true" hinges (note: Schlangen and Van Mier used pendulum bars as hinges), a mode I crack develops along a curved path. However when some frictional restraint is present in the supports, secondary cracking may occur on the other side of the specimen, Fig. 11b. As shown in Fig. 11a, the load-deformation diagram depends on the boundary conditions in the experiment: fixed supports yield a much higher descending branch than observed in a test with "true hinges". By measuring the load distribution in the pendulum bars, it could be concluded that the loading of the specimen was almost frictionless. In a carefully conducted test, the ratio F2/F1 in the bars should remain constant at 1/10. When friction is present, smaller or larger deviations from this value would occur, and the loading of the specimen would deviate from the intented loading scheme, therefore leading to different fracture modes.

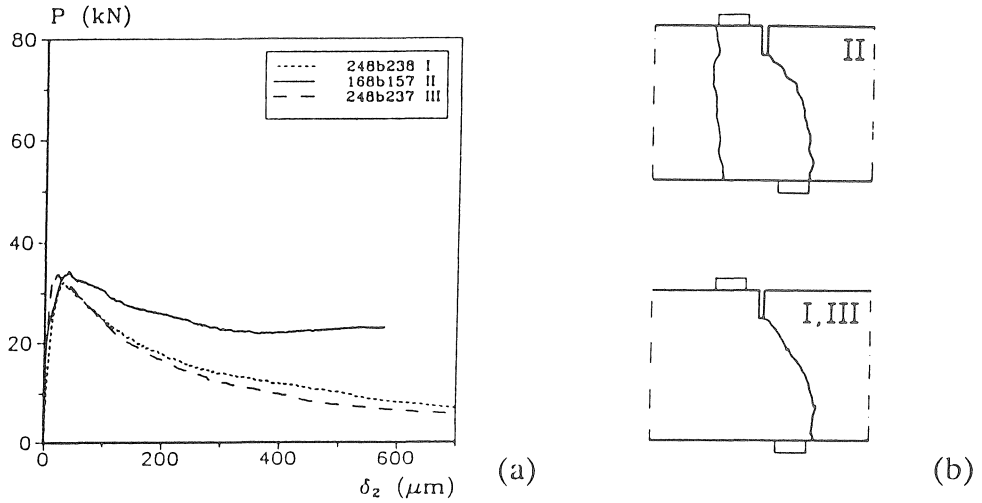

Fig. 11. Effect of boundary conditions on the cracking in single-edge-notched four point shear specimens: test I with rotating supports; test II with fixed supports. (a) P-δ diagrams, and (b) final crack patterns. After [30].

On the basis of all research carried out in the past, it seems that in many structural situations cracks will initiate in mode I. The effect of shear seems restricted to deviating the cracks from a straight path. Next to this, the bridging zone in the crack may cause different stress-redistributions and it is not very clear what processes take place when shear is applied. The limit case of fully openend cracks (without bridging) subjected to shear has been explored in the past, by for example Walraven [31], who developed a sophisticated grain model for the analysis of the shear stiffness of rough cracks in concrete. For small crack openings the situation is much more complicated in view of the presence of the briding stress, and it seems that the Aggregate Interlock theories are not applicable anymore in this regime. Note that most cracks in concrete structures are partly opened cracks which still allow for some stress transfer.
The lack of understanding of the behaviour of small cracks under shear is the major reason for initiating the present investigation. In most of the tests described in this report specimens were pre-cracked in mode I, whereafter a mode II (in plane shear) load was applied. It is tried to determine the frictional characteristics of a cracked specimen, where the crack openings are very small (10–400 μm), and where still cohesive stresses are present normal to the crack plane, see Fig. 12.

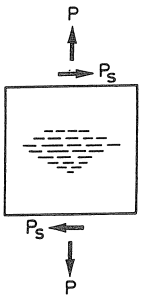

Fig. 12. Shear loading on a partially cracked specimen.

2.3 *Does mode II fracture exist?*

The question from the title of this paragraph is very intriguing and has been tempted many researchers to investigate the mode II (in plane shear) fracture of concrete. In the previous paragraph, reference was made already to the shear fracture tests of Bažant and Pfeiffer, which actually showed to be a curious mixed mode experiment. In effect it may be expected that (at the grain level) mode I fracture completely governs the behaviour of the specimen.
The question remains, under which conditions may a "true" mode II failure be obtained, and what is the amount of energy dissipated in the process. How do we define mode II fracture? The "shear crack" (which may be a single crack or a conglomerate of individual inclined tensile cracks in a narrow band, see Fig. 9) should remain in the plane of the

shear loads, and no secondary cracking should occur. This is a very severe restriction, and does not seem to apply to many of the geometries shown in the previous paragraph. A number of situations where "true" shear fractures may occur according to the above definition are (1) under dynamic loading, (2) in fiber reinforced concrete, and (3) under triaxial compression.

Recent results by Davies [32] indicate that when fracture occurs very rapidly, the cracks follow the direction of the maximum shear stress, rather than the direction of the maximum tensile stress. This phenomenon was observed in double notched and punch-through shear cubes. The stress-directions were determined from a linear elastic analysis of the uncracked specimen. These results are very interesting because they indicate that eventually mode II fracture may happen in heterogeneous materials, probably when the shear fracture energy equals the mode I fracture energy under dynamic loads.

Shear fracture, in the form of a band, has been observed in triaxially compressed concrete as well, see for example [33] (Fig. 13). The restriction should be made that the

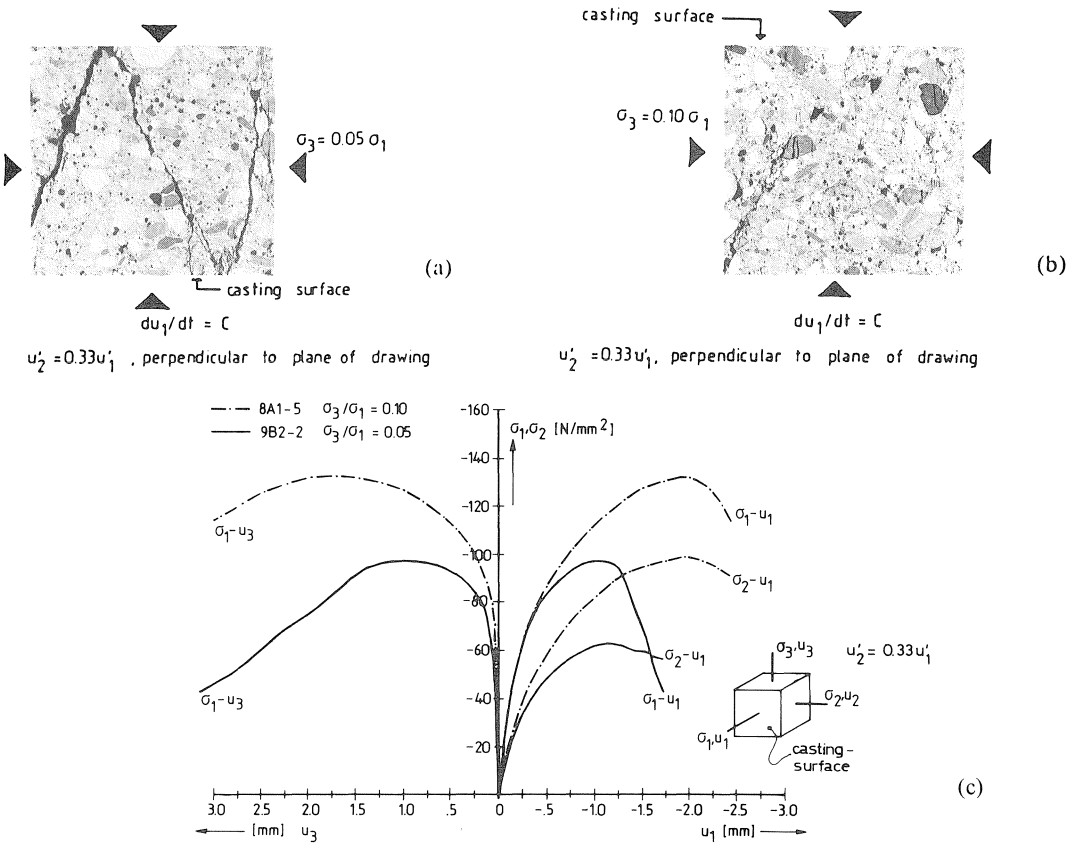

Fig. 13. Shear bands in triaxially loaded concrete: (a) $u_2 = 0.33\ u_1$, $\sigma_3 = 0.05\ \sigma_1$; (b) $u_2 = 0.33\ u_1$, $\sigma_3 = 0.10\ \sigma_1$; (c) load-displacement diagrams, after [33].

confining stress is not too high (viz. not larger than approximately 30% of the maximum principal stress) to allow for brittle failure. For higher confining stresses, a more ductile behaviour is measured, and no localization in shear bands has been observed to date. When the energy needed to obtain a stable shear band is equalled to the surface under the stress-strain curve, it is found that the mode II fracture energy might be over 100 times as large as the tensile (mode I) fracture energy, depending on the amount of confinement. The localization in compression, including boundary and size effects can be simulated with a simple numerical micromechanics model which was recently developed by Vonk et al. [21].

Secondary cracking seems to be prevented when a good confinement of those parts of the specimen outside the shear fracture zone is present. In fact several researchers have tried to design mode II fracture specimens where an optimal confinement is derived from the geometry itself, e.g. [34, 35]. In many cases, as argued before, these geometries seem to preform well at crack initiation, but as soon as a small crack grows in the specimen, severe stress redistributions have been observed to lead to secondary tensile cracking. Another possibility of confining the parts of the specimen outside the shear fracture zone is the addition of fibres to the concrete. In this way, shear fracture in the sense of "an array of inclined tensile cracks" has recently been observed by Arslan, Hughes and Barr [35] in polypropylene and steel fibre reinforced concrete, see Fig. 14. As earlier proposed by Yin et al. [36], the fibres act as some internal confinement.

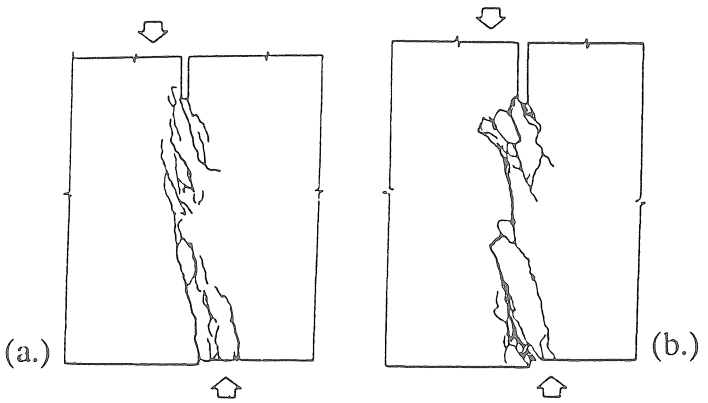

Fig. 14. Shear fracture in (a) polypropylene fibre reinforced concrete (0.10%); and (b) in steel fibre reinforced concrete (2%), after [35].

In the limit case, SIFCON, Slurry Infiltrated Fibre Concrete, may be considered. The material has extreme high steel fibre contents, viz. depending on the size and shape of the fibres up to 10–15% by volume. The structure of the material is extremely anisotropic, and weak planes may exist. Recently it was shown [37] that the shear strength of these weak layers is very low, not exceeding 10% of the compressive strength of the

material. The shear fractures are arrays of inclined tensile cracks, similar to the fracture shapes in ordinary FRC. In the present study, the results of tension/shear experiments on SIFCON will be discussed in detail in chapter 5.

3 Experimental technique

In this chapter the experimental technique is explained, and specimens, materials and manufacturing procedures for the specimens are described.

3.1 *Biaxial test-rig*

As mentioned in the previous chapter, various specimens have been proposed for studying mixed mode fracture of concrete. In the experiments in the Stevin Laboratory it is tried to determine the shear stiffness of cracked concrete. The research focusses on small cracks when still cohesive forces are transfered over the crack. A large problem is that softening is partially a material property and partly a structural property (see [38]). Especially just beyond the peak in a tensile stress-crack opening diagram, the crack growth is non-uniform, and part of the specimen may be cracked, whereas other parts are still uncracked. The boundary conditions of the experiment (e.g. stiffness of the test rig, rotating specimen boundaries, specimen size) determine to a large extent how a specimen will fracture. The effect of shear in this regime is not easy to determine. More simple is the situation again at larger crack openings, $\delta > 50$ to 100 μm, when bridging is the main stress transfer mechanism between the crack faces. In this case, the shear loading of a uniform bridging zone is straightforward, and an effective shear stiffness can easily be determined. Both situations are investigated in the experimental programme.

3.1.1 Loading frame

The biaxial test-rig that was used, was developed by Reinhardt et al. [39]. The loading frame and a substantial part of the test control system, was developed and built by the Measurement and Instrumentation group of the Stevin Laboratory, except of course the basic parts such as the SCHENCK servo-controller unit and the Personal Computer. The biaxial test-rig consists of two independent stiff square loading frames. The exploded view of the machine is shown in Fig. 15. The outer frame A is a coupled frame and it is capable of moving along the horizontal direction. The inner frame B can move along the vertical direction. The two frames A and B can move completely independent of one another. The outer frames and the inner frame are fixed to the overall frame via 8 vertical and 4 horizontal plate springs as shown in Fig. 16. When the machine was built, it was assumed that the plate springs prevent the frames from rotating (Note: in the meantime it has become clear that due to the non-uniform fracturing of a specimen, testing between non-rotating platens is almost impossible). The plate springs have a limited bending capacity (1 N = 1.08 μm/m). On each side of the plate spring two strain

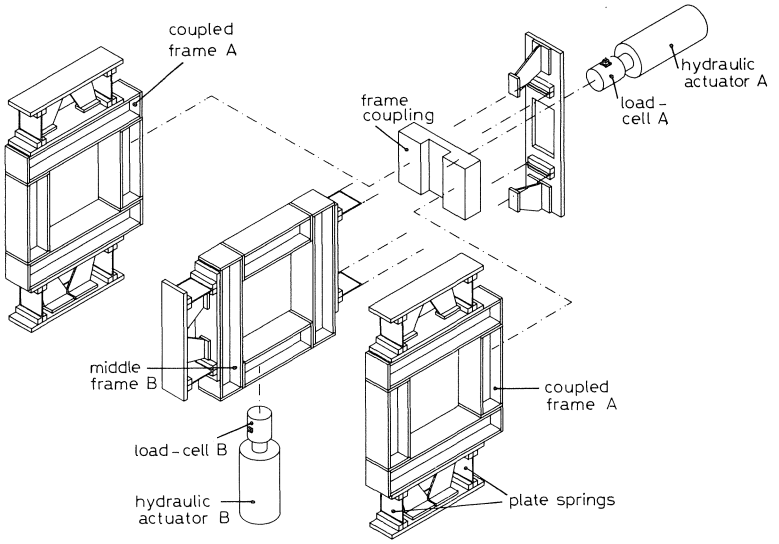

Fig. 15. Exploded view of the biaxial test-rig.

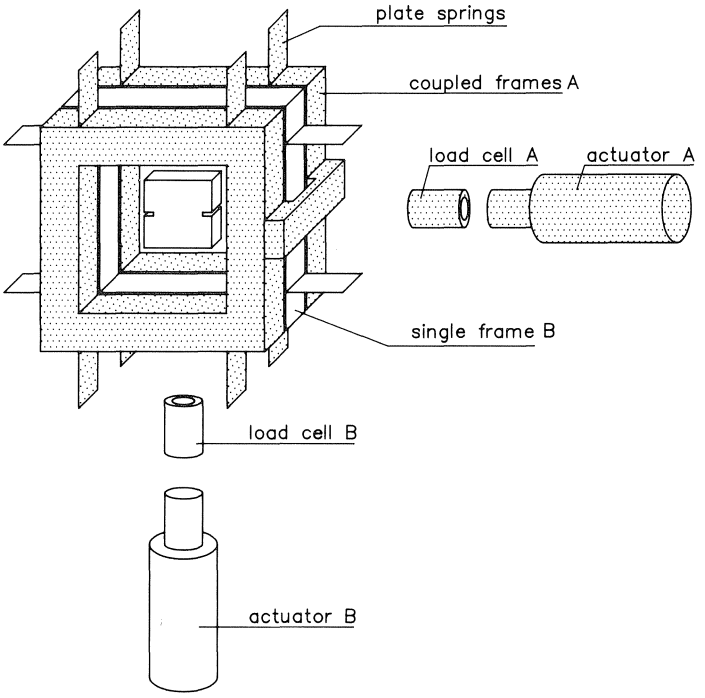

Fig. 16. Assembled frames.

gauges are mounted and connected in a full Wheatstone bridge configuration (6 Volt potential) to the data acquisition system. The plate springs were instrumented because this gave the opportunity to verify if the loading of the specimen was indeed equal to the load measured with the load-cells that were fixed between the frames and the hydraulic actuators. Moreover, any eccentricity which may occur during a test in the frame assembly could be traced back from the plate spring readings.
Two hydraulic actuators (A, B) and two load cells (A, B) are situated outside the loading frames in order not to hinder the overall stiffness of the loading frame. The frame assembly is shown in Fig. 17.

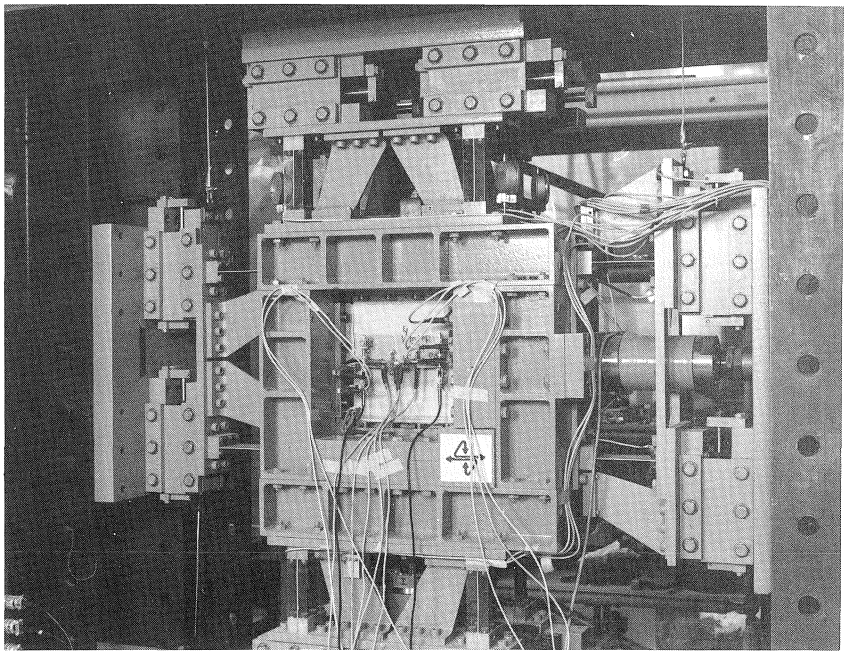

Fig. 17. Photograph of the biaxial test-rig.

The specimen was fixed to the double and single frame using F-88 (Tridox) self curing non-epoxy plastic adhesive cement. To properly glue the specimen into the machine there must be enough space surrounding the specimen. There were two types of displacements possible in the frame. A large displacement to the frames could be inflicted via roller bearing units connected to guiding bars (Fig. 18). The roller bearing guiding unit was blocked during the execution of a test, and small displacements were possible due to the plate springs which have a limited bending capacity. To glue the specimen into the machine, a small compressive force ($\pm$ 5 kN) was applied. After the specimen was properly glued to the loading platens, and the adhesive was allowed to set for approximately 90 minutes, the roller bearing units of the double and single frames

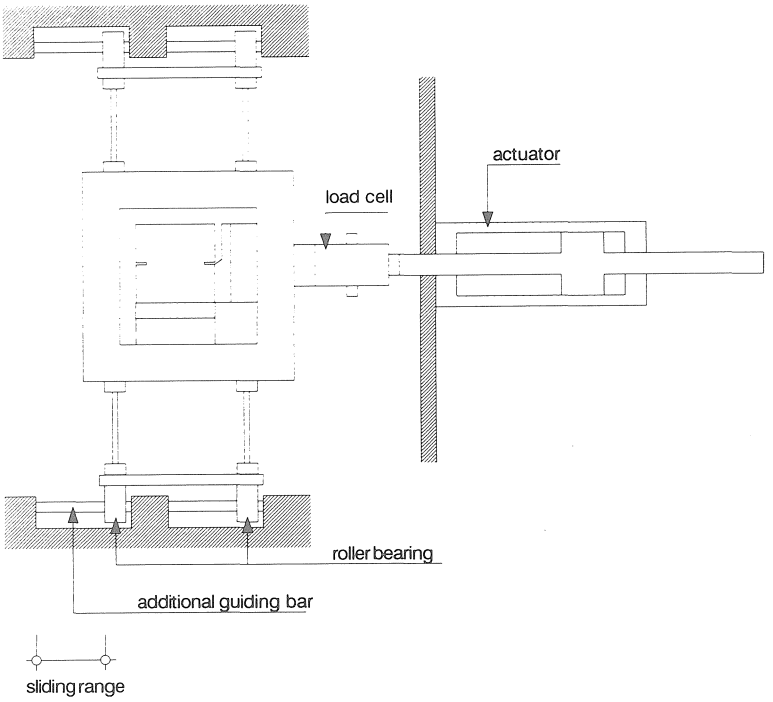

Fig. 18. Roller bearing guiding unit for large displacements of the frame.

were fastened using bolts. Damage to the plate springs, caused for example by undesired movements of the frames, was prevented through several security devices which are made of steel plates as shown in Fig. 15.

In Figs. 19a and 19b, a sectional view of the loading frame is shown at two different stages of loading. A 200 mm square Double-Edge-Notched (DEN) specimen was glued to the frames. As can be seen from the figures, the top of the specimen is glued to the inner frame and the bottom of the specimen to the coupled outer frame. The inner frame can slide in between the coupled frame as shown in Fig. 19a. The specimen is loaded by moving the middle frame upward. A tensile stress develops in the concrete specimen, because the coupled outer frames are fixed in the vertical direction. A tensile crack always nucleates in the notched region which is located at half height of the DEN specimen (Fig. 19b), where crack growth can be followed at a known location. This enables deformation controlled testing. When the specimen cracks, and the crack opening is sufficiently large, bending of the horizontal plate springs will occur as shown in Fig. 19b.

The DEN specimens are fixed to the frames via steel loading platens. For a uniaxial tensile test only two loading platens are required, however, for a biaxial test two additional loading platens are needed in order to apply a lateral in-plane shear load. They are glued to parts of the left and right edges of the specimen as shown in Fig. 20. Also

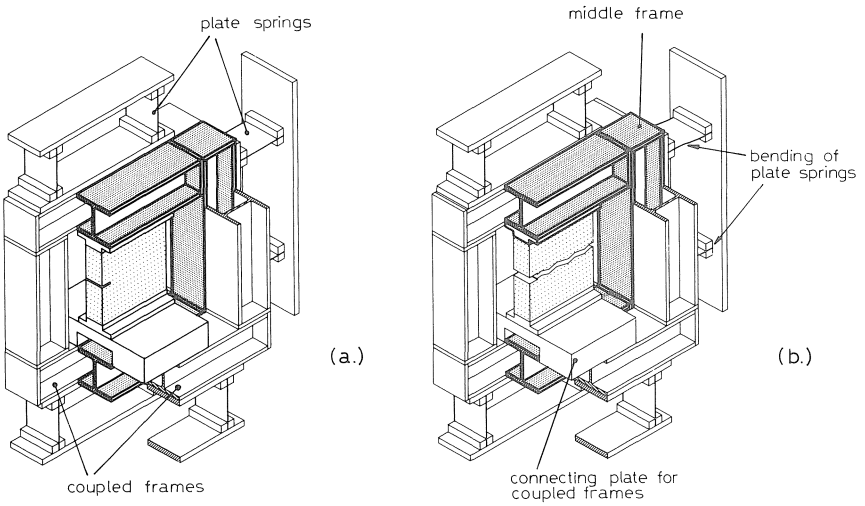

Fig. 19. Sectional view of the biaxial test-rig in two stages: (a) before and (b) after cracking. Note the bending of the plate springs in figure (b).

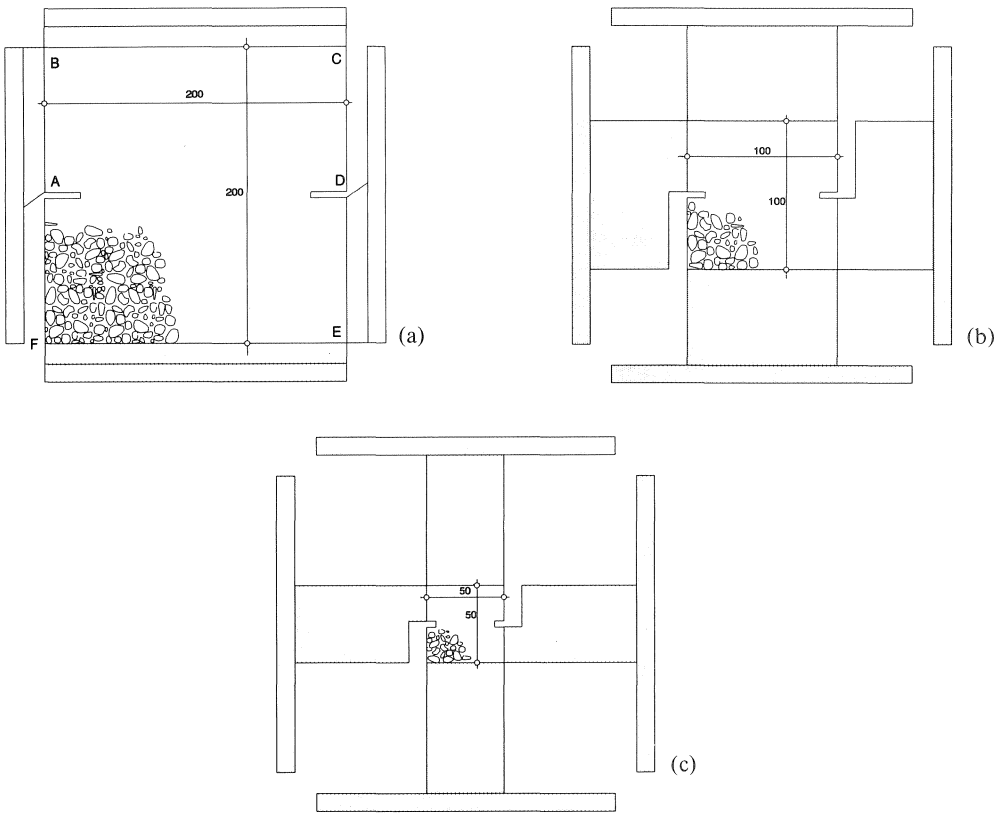

Fig. 20. Glue platen assembly for 200, 100 and 50 mm specimens.

shown in this figure are the complete loading platen assemblies for the three different specimen sizes tested in the present investigation. The glue platens at the edges A-B-C and D-E-F of the 200 mm specimen (Fig. 20a) are fixed to the inner frame B and the outer coupled frame A respectively. Any shear force acting at the specimen edge D-E is counter balanced by the reaction exerted at the edge A-B, since the inner frame is fixed along the horizontal direction. Some modification in the loading platen assembly is required in order to accommodate the specimens with two other sizes (100 and 50 mm) in the test-rig. Accordingly, two different loading platen arms made of stainless steel were designed to fix the specimens into the frames as shown in Fig. 20b and c. Especially for the 50 mm specimen this results in rather slender loading platens. The influence of the loading platen arms on the specimen behaviour under biaxial loading is not yet known. The effect of boundary rotations in uniaxial tensile tests has been analysed before, see [40, 41, 42].

The *assumed* boundary condition for a DEN specimen is shown schematically in Fig. 21. The boundary conditions were such to allow for parallel end platen movement in the vertical and horizontal directions during a test. In principle the test resembles a shear-box experiment, frequently used in rock testing.

In the SIFCON experiments, two additional steel platens were glued to the free sides of the specimens in order to avoid glue fractures between the specimen and the loading platens. Glue fracturing was very critical when high shear loads were applied, but it was found that by using the additional glue platens the undesired glue fractures could be avoided. In the photograph of Fig. 24, where a fully instrumented SIFCON test is shown, the two additional steel platens are visible.

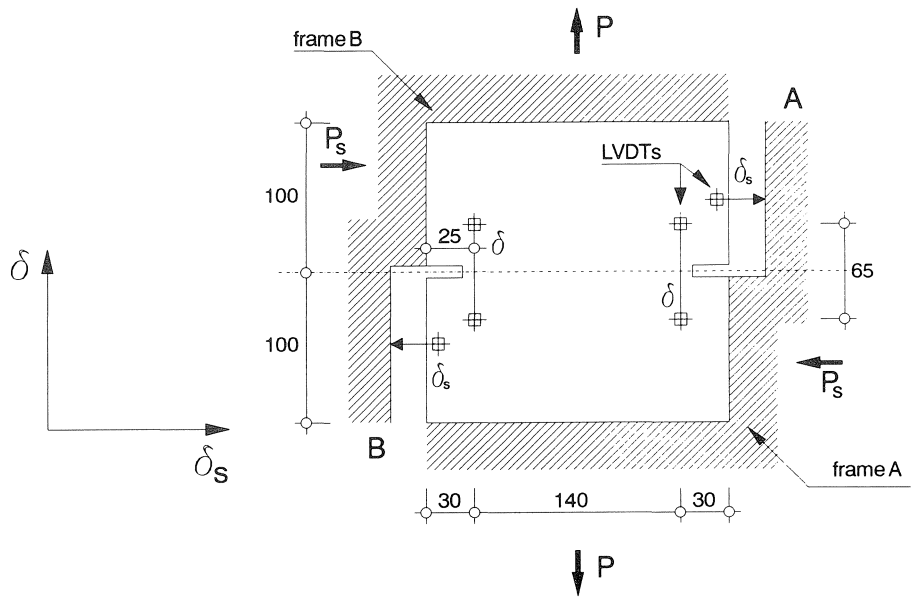

Fig. 21. Boundary condition for a Double-Edge-Notched specimen subjected to combined tension and shear.

3.1.2 Load and displacement measurements

The machine contains two hydraulic actuators and two load-cells as shown in Figs. 15 and 16. The capacity of the actuators is 100 kN in compression and tension with a maximum stroke of 40 mm. The actuator is connected to the load cell via spiral washers. The capacity of the load-cells is restricted to 50 kN. The loads are measured using the calibrated load cells (40 μm/m/kN and 20 μV/V/kN) with four strain gauges in full Wheatstone bridge configuration. The signals from the vertical and horizontal load cells were amplified via two standard amplifiers (SCHENCK MV 318) to the servo controllers. A 10 V signal corresponds to a load of 50 kN. The maximum loading capacity is restricted to 50 kN because of the limited strength of the plate springs that are used for fixing the loading frames.

For the vertical deformation measurements (crack opening), two or four LVDTs (Sangamo, A6G1) with a gauge length of 65 mm were used. The position and the number of LVDTs varied depending on the type of tests performed. In the beginning of the investigation, in plain concrete test series 14 to 18 (the various test series are identified in section 3.2), two vertical LVDTs were placed at the middle of the specimen, one at the front and the other at the rear face of the specimen as shown in Fig. 22. Later, starting from test series 28, four LVDTs were used for test control in the vertical direction, two at each face of the specimen near the notch as shown in Fig. 23a for a 200 mm

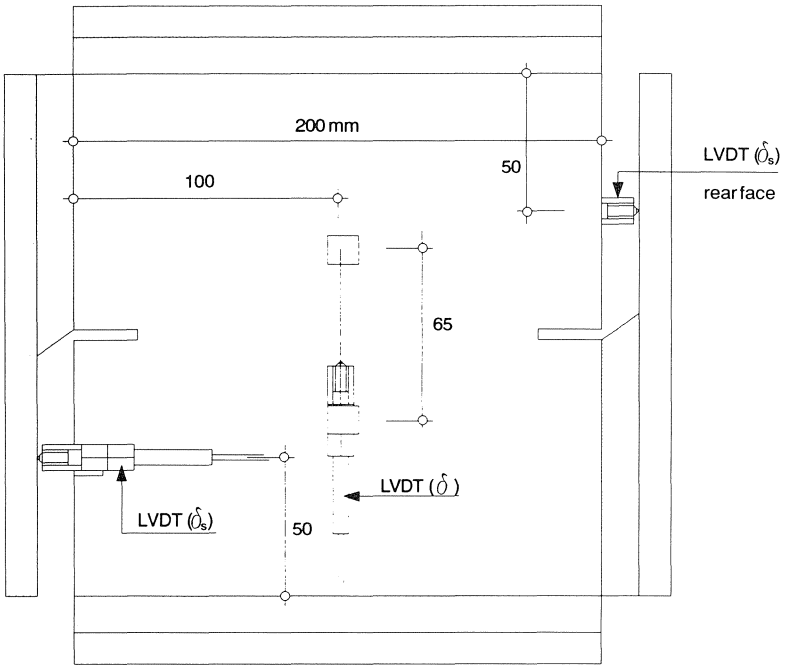

Fig. 22. Locations of LVDTs for test control in test series 14 through 27: two LVDTs (δ) for vertical control, and two (δ_s) for lateral (shear) displacement control.

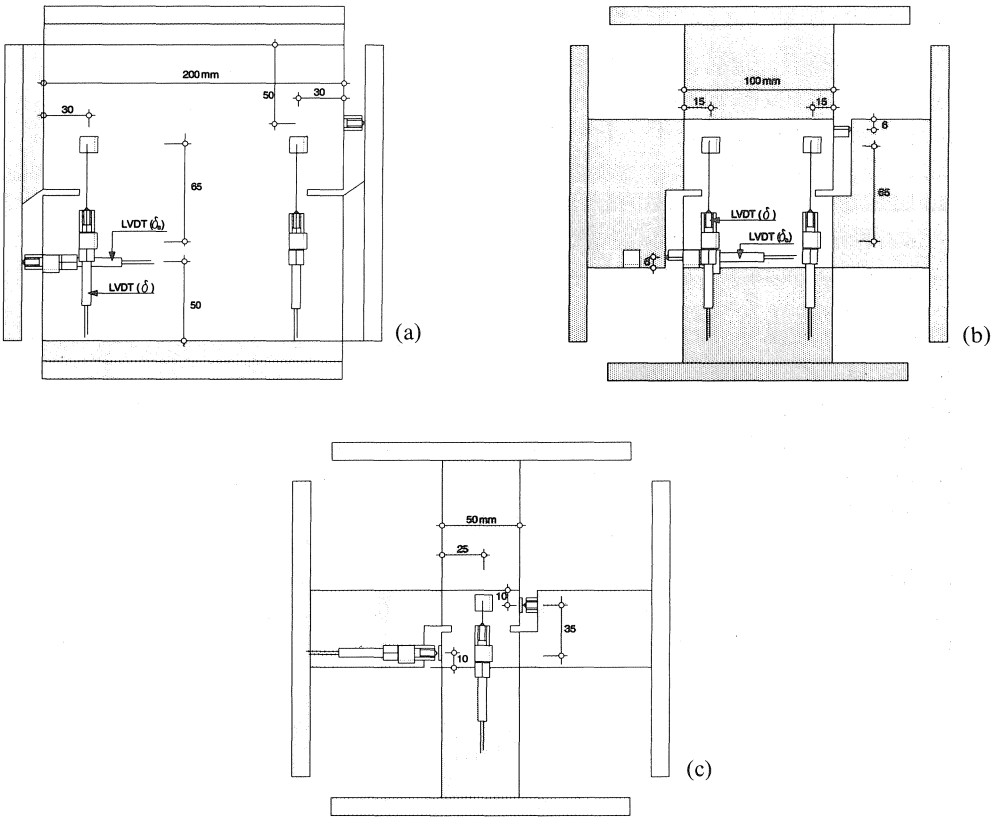

Fig. 23. Locations of vertical and horizontal LVDTs for specimens of three different sizes, plain concrete test series 28 through 48, and SIFCON tests.

specimen. Depending on the particular load-path, the fracture mode can change and quite frequently the crack would grow outside the control region when the control LVDTs were fixed at the middle of the specimen. It proved to be better to place the LVDTs near the notch in order to obtain a stable test. Note that this could be done for the 200 and 100 mm specimens only. For the 50 mm specimens two LVDTs with a gauge length of 35 mm were used as shown in Fig. 23c, but here no cracking could occur outside the control length simply because the specimen size would not allow this. The LVDTs were calibrated using a device containing a Mitutoyo micro-screw (range 50 mm; accuracy 5 μm). The LVDTs have a linear stroke of ± 1 mm with a nonlinearity of 0.3% (calibration: a 10 V signal corresponds to 400 μm vertical/horizontal deformation). The photograph in Fig. 24 shows the front face of a fully instrumented 100 mm (SIFCON) specimen. The LVDTs are clearly visible.

For the lateral (shear) deformation measurements two LVDTs (Sangamo, A6G1) were used. At the front face of the 200 mm specimen one LVDT was mounted at the center

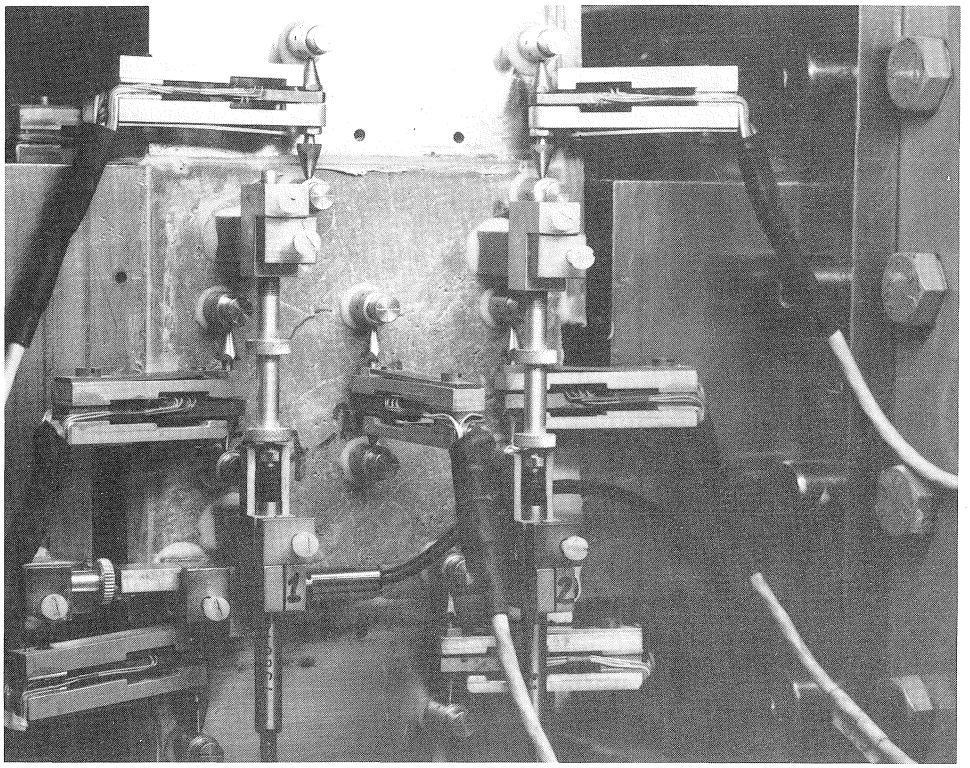

Fig. 24. Photograph of a fully instrumented 100 mm SIFCON specimen.

of the bottom half as shown in Fig. 23a; the second LVDT was fixed in a diagonally opposite position at the rear face of the specimen. The global shear displacement δ_s was defined as the average displacement between the two specimen halves measured by the two horizontal LVDTs. In Figs. 23b and 23c the positions of the horizontal LVDTs for the 50 and 100 mm specimens are shown.

In addition to the LVDTs, a number of extensometers (mechanical-electrical transducers of the cantilever type of size 15 × 50 mm, developed and constructed by the Measurements and Instrumentation group of the Stevin Laboratory), were used to measure local deformations. To convert the mechanical displacement into an electrical signal, two strain gauges were used in this extensometer as shown in Fig. 25. They were connected to the data acquisition system in a full bridge configuration with a 6 V potential. The extensometer has a range of 0–2 mm, a resolution of 1 μm, and a linearity of 0.5%. The same calibration device mentioned above was used to calibrate the extensometers.

The number of extensometers used varied depending on the type of test and the size of the specimen. Six extensometers with a gauge length of 35 mm (three extensometers at the front and the back face of the specimen), were used in test series 14 to 32 (plain con-

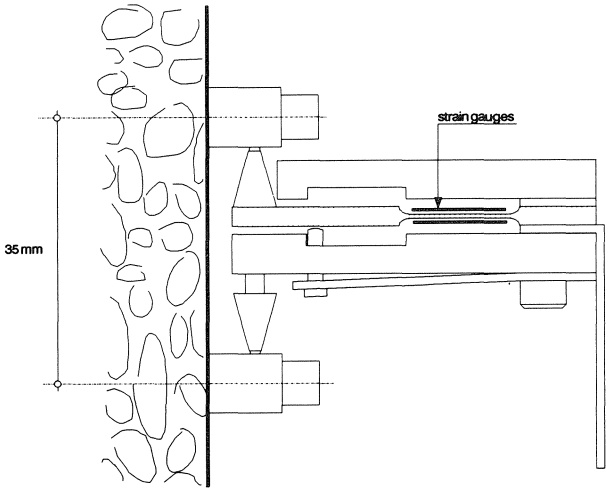

Fig. 25. Schematic diagram of an extensometer developed by the Measurement and Instrumentation Group of the Stevin Laboratory.

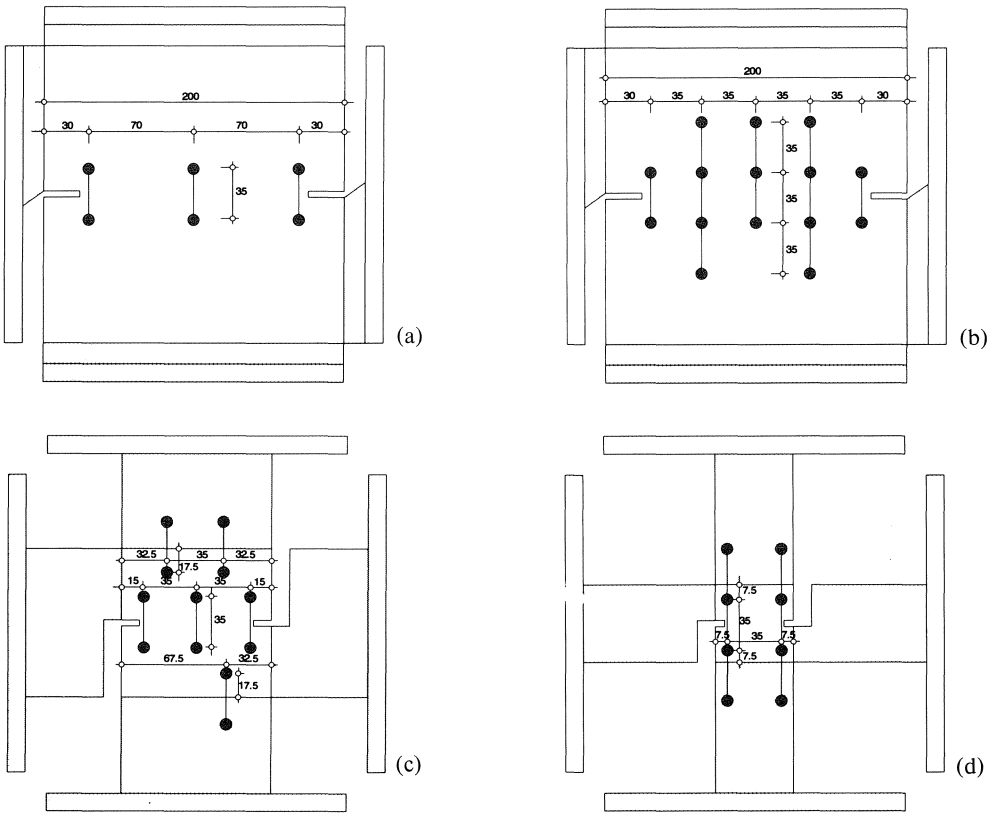

Fig. 26. Various extensometer arrangements for specimens of three different sizes.

crete) and the SIFCON tests, see Fig. 26a. In a later test series (46–48, plain concrete), a large number of extensometers was used in order to capture the growth of overlapping cracks. This was the dominant fracture mode under the specific load-path followed and for the three different specimen sizes used in this series. As shown in Figs. 26b, 26c and 26d, the number of extensometers used for the 200, 100 and 50 mm specimens was 20, 14 and 12 respectively. In the experiments on the 50 and 100 mm specimens (for plain concrete and SIFCON), additional extensometers were placed over the glue layers in order to verify if no cracking occurred in or near the glue layer. When cracking was detected in or near the glue layer the experimental result was rejected because this would normally lead to undesired stress redistributions within the specimen. In Fig. 24, the extensometers for monitoring glue fracture can be seen.

3.1.3 Test control

The SCHENCK hydropuls system as available in the Stevin Laboratory is an energy transmission system: the electric energy is transformed into hydraulic and mechanical energy that can be regulated. Eventually this mechanical energy can be used to load a test specimen. The loading can be applied to a specimen in a desired manner with a closed loop servo controlled system.

The hydraulic power is supplied to the loading installation through the hydraulic power unit, which consists of an electrical motor, an oil pump cooler, a filter, electrical switches etc. The hydraulic power unit regulates the oil in the main supply line at a pressure of 220 bar and a flow rate of 40 l/min. The hydraulic pressure unit and the total current is regulated by SCHENCK DU 312 and in case of an emergency this unit is capable of shutting off the hydraulic supply and the flow of current in the closed loop system. However, it is modified by the measurement group of the Stevin laboratory such that in case of an emergency only the hydraulic supply is terminated and the electrical current remains in the circuit. The purpose of this is to avoid damage to the test specimen due to the termination of the power supply. The SCHENCK steering monitor DP 317 controls the hydraulic supply from the main hydraulic line to the actuator. Also it is capable of linking the steering monitor to external devices such as a computer. In this manner a fully automated system was built, capable of testing along pre-determined load-paths.

Tests can be performed either in load or in deformation control. But, for a stable uniaxial tensile test (stable crack growth), deformation control is essential. Two independent regulation circuits are available, and it is possible to control the vertical and horizontal deformations separately in a test. Moreover, tests can also be performed with deformation control in the vertical direction and load control in the horizontal direction and vice versa.

The average signal of the control LVDTs is amplified via a standard amplifier (SCHENCK MV 318) to the servo controller unit. The servo controller unit consists of a two part unit, an adaptable digital controller (SCHENCK RA 311) and a standard control signal unit (SCHENCK FP 312). To this servo controller a function generator

was connected, which consists of two identical linear time base generators A and B. In a deformation controlled test, the average vertical deformation δ (in Volt) was used as the feedback signal. A comparison was made between the feedback signal and the program signal from the function generator and a control signal was supplied by the servo-controller to the servo valve (type MOOG D-7030, $\Delta p = 70$ bar, flow rate = 5 l/min) through a power amplifier (SCHENCK RL 311).
Depending on the type of test, either the average vertical deformation δ or the average global shear deformation δ_s was used as the feed back signal in the closed loop servo control. Of course tests could also be carried out in load-control, and in some of the load-paths investigated a constant load was kept normal to the crack plane during shear. In Fig. 27 the complete closed loop sytem is shown schematically.

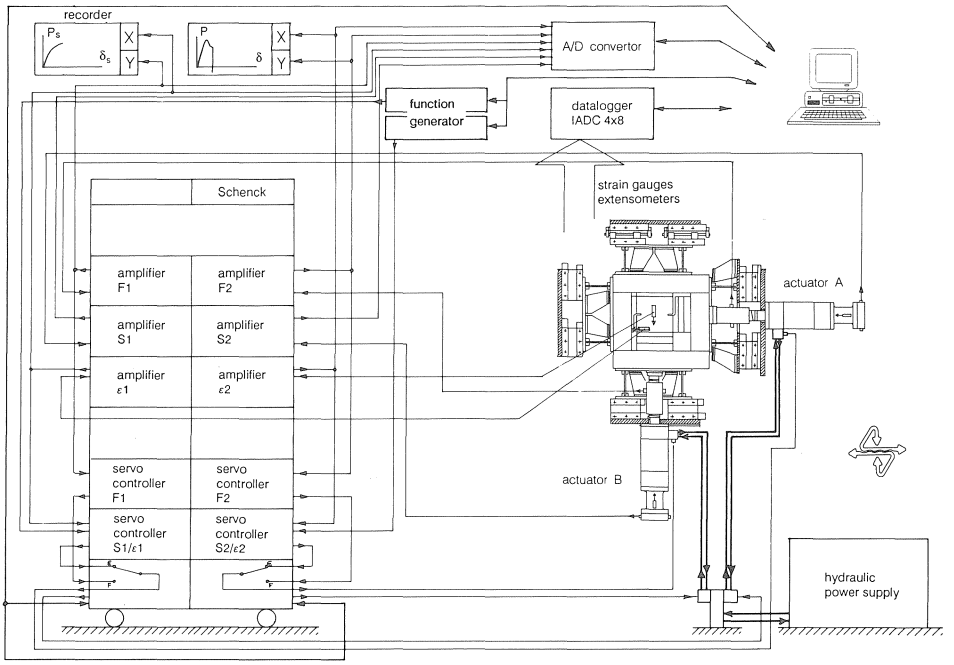

Fig. 27. Overview of the complete biaxial loading system.

3.1.4 Data acquisition system

The measurements during a test can be divided into three categories: (1) the load cells (vertical and horizontal), (2) the LVDTs (vertical and horizontal) and (3) the extensometers and strain gauges. All of these signals were in an analog form. First the signals from the load cells and the LVDTs were amplified to the SCHENCK regulation circuit. The output signals corresponding to two loads and two deformations (LVDT) were fed

to an HP Vectra ES/12 Personnel Computer via a 12 bit fast analog/digital converter. Next to this, the load P and the vertical deformation δ were plotted directly on a XY recorder (type HP-7046A); the shear load P_s and the shear deformation δ_s were plotted on a $X_t Y_1 Y_2$ recorder (type PHILIPS PM-8132). A 32 channel programmable data logger (designed by the Measurement and Instrumentation Group of the Stevin Laboratory) was used to retrieve the data from the extensometers and strain gauges. A 6 Volt bridge power was applied to either a full, half or quarter bridge Wheastone configuration, with an internal resistance of 120 Ω. For the present data acquisition only full bridge configurations were used. The total time needed for scanning 32 channels was 976 ms. A micro-computer was required to program the data logger. Transmission of commands and data was provided by a simple RS 232 serial channel. The output from the data logger was stored on a floppy disk (0.7 MB).

Dedicated software was developed which allowed fully automatic testing. The Personal Computer controls the datalogger, the SCHENCK regulation system, the A/D converter and the function generator as shown in Fig. 27. During a test, all measuring devices would be scanned at fixed time intervals. The load was applied continuously and no stops were made for scanning of the measuring devices. The data logger was programmed to scan every 10 seconds from the beginning of a test, with the capability of changing the scan time (usually to 30 or 60 seconds in the descending branch). The floppy could accommodate 600 scan steps. In general a change in scan time was required to include a complete test on a single floppy (0.7 MB).

A typical scan consists of signals from two loads (P, P_s) [mV], two deformations (δ, δ_s) [mV], six to twenty extensometers [μV], and twelve strain gauges [μV] from the vertical and horizontal plate springs. During a test, the vertical and horizontal forces and deformations, the scan-number and the elapsed time were printed for each scan. All data were stored immediately on disk. Through a simple program the stored data were transformed into an advanced Symphony spread sheet format and the results of the test were obtained on the same day. Only recently, a custom built programme has been completed for plotting the results in any desired format.

3.1.5 Experimental problems

When fracture properties of materials are to be determined, it is extremely important to have the desired boundary conditions. In all the tests, the plate boundaries were kept parallel to each other (Fig. 20). With a critical mind the experimental errors in the machine were studied. Some eccentricities in the machine were already known and are discussed in [12]. For example it was found that cracking always initiated at the front left notch. As observed before, non-uniform crack opening is prevalent in heterogeneous materials such as concrete. Due to that, rotations of the frame are unavoidable even though plate springs were designed to avoid them.

3.1.5.1 Influence of glue platens

Fig. 28 shows the uniaxial P-δ diagram for two DEN specimens (200 mm) glued

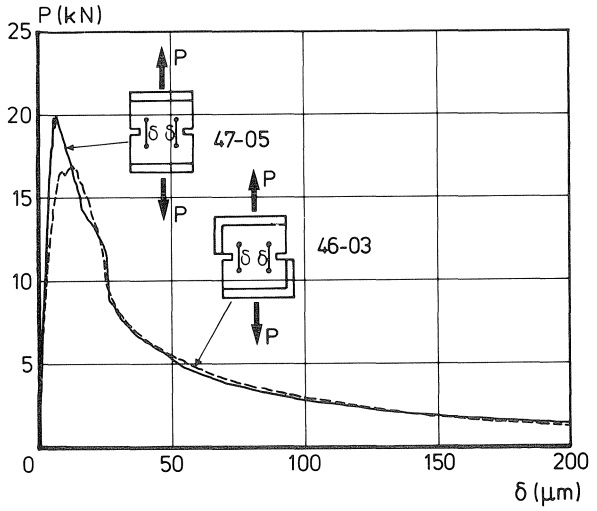

Fig. 28. *P-δ* diagrams for two 200 mm specimens loaded in uniaxial tension between two or four loading platens respectively.

between two and four loading platens respectively. The results indicate that the specimen 47-05 with two loading platens gave a higher tensile strength than the specimen 46-03 glued between four platens. This was consistent throughout the entire test series. Previous analyses indicated the same trend [43]. Gluing of the lateral loading platens results in a more eccentric loading on a the specimen as compared with the case of two glue platens. The specimen with two platens gave a sharp peak compared to the one with four platens which gave a rounded peak. Additional eccentricities may be created when a specimen is glued between four platens.

The eccentricities related to non-uniform cracking can be observed from plots of the local deformation δ_i versus δ in Fig. 29. The axial load P was plotted in the same graph for the specimen with two loading platens. Numbers 1 to 8 correspond to 8 extensometers used for measuring local deformations at the front and rear faces. Fig. 29a, which shows the results for the specimen glued between *two* platens, indicates that the crack initiated near extensometer 1 and subsequently at the locations of extensometers 5, 2, 6, 3, 7 and 8 (this can be deduced from the order of the intersection points with a straight line, for example at $\delta = 10$ μm). This method for following crack growth is valid, as was found in a study where reflection photo-elasticity was used as crack detection method [12]. The eccentricity in the machine caused the crack to initiate at the left-notch, at the location of extensometer 1. The deformation measurements demonstrate the non-uniform crack opening in uniaxial tensile tests and confirm the observations made before by Van Mier [33] and Hordijk et al. [44]. Note that correcting the machine for small eccentricities is almost impossible. The slightest non-uniformity will cause eccentric crack modes.

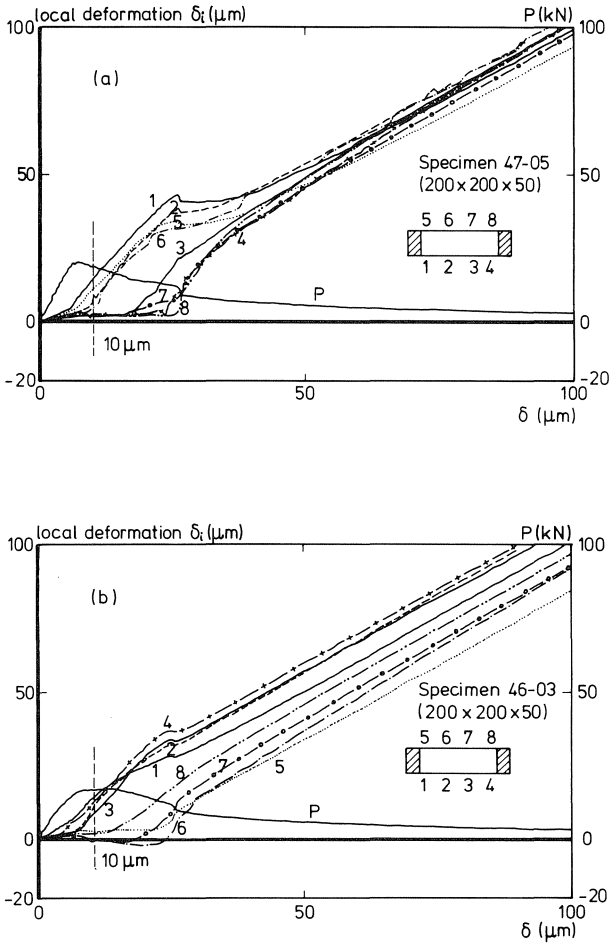

Fig. 29. Plots of local deformations δ_i versus control deformation δ for two uniaxial tensile tests with respectively two glue platens (a), and four glue platens (b). The specimen size is 200 mm.

A different phenomenon was observed in specimen 46-03 with *four* sides glued. Fig. 29b shows the δ_i-δ plot. Obviously the fracturing process is completely different to that of specimen 47-05. In Fig. 29a the largest local deformation also occurred (for example at $\delta = 10$ μm) at extensometer 1 as discussed before, subsequently large deformations occurred at extensometers 4, 2 and 3 between the first and the second load drop. However, extensometers 5 and 6 were in compression in this process, and it seems that out of plane bending occurred in this particular specimen.

From the above discussion it is obvious that the fracture evolution becomes different when the specimen is glued either between two or four loading platens. The effects of eccentricities in the frames seems more pronounced when four platens are glued.

3.1.5.2 Frame rotations

The frames in the biaxial loading rig can probably rotate in a number of ways, in spite of the fact that it was designed as a stiff machine where specimens are loaded between parallel travelling boundaries, see Reinhardt et al. [39]. A possible situation is shown in Fig. 30, where the inner frame rotates and the outer frames remain stationary. If this is the case, then the lateral shear deformation measurement δ_s defined as the relative horizontal displacement between the two frames, may include some part of the frame rotation. Therefore, at this stage it can not be concluded that δ_s is the true shear deformation. Yet, the value will be close to the true value because the machine is almost completely symmetric. In order to measure the in-plane frame rotation an independent frame of reference is required. Because of the almost perfect symmetry of the biaxial test-rig, it is assumed that the shear displacement corresponds to the true shear displacement between the two specimen halves. Future tests with an independent reference frame are planned.

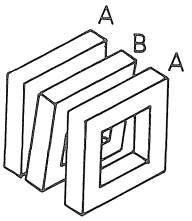

Fig. 30. Hypothetical out-of-plane rotation of frame B with respect to frame A.

Initially, relative out-of-plane displacements of the frames were measured using four dial gauges as shown in Fig. 31. A 100 mm specimen (46-20) was glued in the machine between four loading platens, and four dial gauges were mounted on top of the steel frames as indicated in Fig. 31. A lateral shear load P_s was applied to the specimen in displacement control until $P_s = -2.5$ kN; subsequently, the lateral test control was changed to load control and an axial tensile load was applied in displacement control.

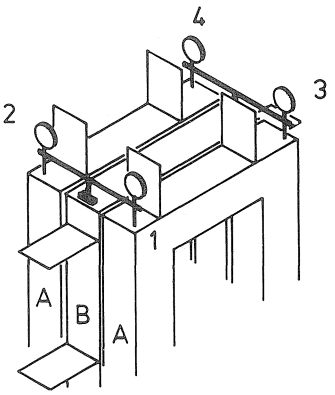

Fig. 31. Placement of the four dial gauges for measuring out-of-plane rotations.

(This corresponds to load-path 4 discussed in chapter 4). Fig. 32 shows the gauge readings versus scan number for this test. In the same plot, the lateral deformation δ_s and the vertical deformation δ are plotted. As can be seen in Fig. 32, δ_s is linear up till scan number 53. During this stage, the gauge readings were almost zero except for gauge 1. This means that there is not much out-of-plane frame movement during the first shearing regime. However, as soon as the axial force is activated, the gauge readings differed significantly, which suggests that much of the frame movement occurred during the initial period. The largest difference in gauge readings were recorded at scan number 100 between gauges 2 and 3. This suggests that both the coupled frames, (front and rear) were not moving by the same amount with respect to the inner frame. Moreover, at the 100th scan the difference in local deformations on the specimen, corresponding to the position of the gauges 3 and 2 were the largest. At this stage, the movements of the frame more or less correspond to the deformation distribution measured at the front and rear surface of the specimen. *In fact, at this stage it is not clear, whether the specimen follows the machine or vice versa. The above result clearly shows the intricate relationship between the specimen and the machine in a fracture test.*
Note that the deformation distribution is more uniform again for larger crack openings. At this stage of loading, as argued in chapter 2, crack face bridging is the main cause of the cohesive stress transfer normal to the crack. The crack face bridges seem to be uniformly distributed over the crack area, see [17].

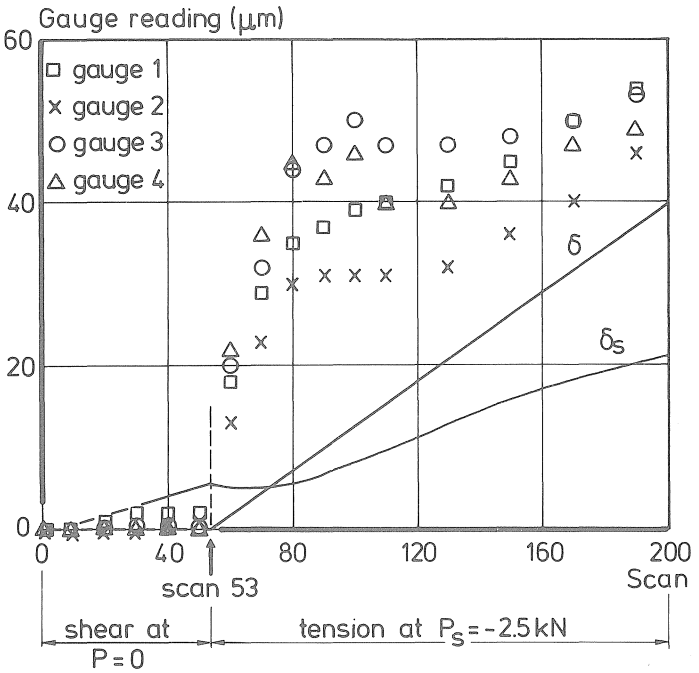

Fig. 32. Average crack opening (δ), crack sliding (δ_s) and the frame displacements measured with the four dial gauges of Fig. 31.

3.2 *Specimens and materials*

When the work with the new biaxial apparatus was initiated in 1987, first a relatively large number of uniaxial experiments was carried out, see [12, 45]. This was done because some doubts were raised about the uniformity of the fracture process, as described in more detail in chapter 2. These preliminary uniaxial experiments were mainly carried out on square concrete plates of size 200 × 200 × 50 mm^3, which is the maximum size of the specimens that can be loaded in the present test set-up. This large size was chosen in order to exaggerate the structural effects caused by boundary conditions and specimen geometry. In the following paragraphs an overview of the materials and specimens used in the *biaxial* test-series on plain concrete and SIFCON is given.

3.2.1 Plain concrete

Most of the experiments were conducted using a mortar with 2 mm maximum aggregate size. In addition to the mortar, normalweight and lightweight high strength concrete of maximum aggregate size d_{max} of 16 and 12 mm respectively were used in order to study the effect of material structure on the biaxial tension/shear behaviour. The aggregate used in the lightweight concrete was sintered fly-ash (lytag).
The different mix designs are shown in Table 1. The strength results ana the maximum aggregate size corresponding to each batch are shown in Table 2. Five plates of size 300 × 300 × 50 mm^3 were cast in a stiff wooden battery mould in the vertical direction.

Table 1. Mix design for the three concretes used in the investigation

	normalweight concrete		lytag
d_{max}	2 mm	16 mm	12 mm
mix proportion	(kg/m^3)	(kg/m^3)	(kg/m^3)
Portland cement	500	375	330
water	250	187.5	110.5
super plasticizer (type Melment L10)	-	-	5.0
air content (%)	2.24	1.3	3.75
River gravel and sand (sieve size [mm])			
0.125- 0.25	303	128	158
0.25 - 0.50	197	165	237
0.50 - 1.0	515	202	158
1.0 - 2.0	500	256	158
2.0 - 4.0	-	256	79
4.0 - 8.0	-	365	-
8.0 -16.0	-	457	-
Lightweight aggregate			
4.0 - 8.0	-	-	264
8.0 -12.0	-	-	484

Two days after casting the plates were demoulded and cured under water. The water basin was kept in the laboratory at an ambient temperature of approximately 18 °C. At an age of 14 days, the plates were sawn (using a rotating diamond saw) into square Double-Edge-Notched (DEN) specimens of size 200 × 200 × 50 mm^3 with a notch depth of 25 mm and a width of 5 mm as shown in Fig. 33a.

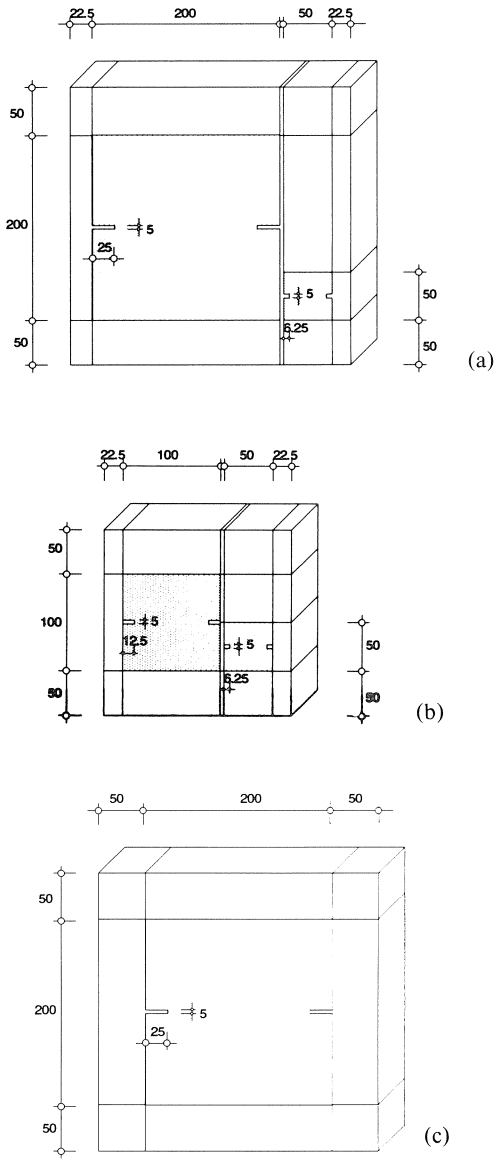

Fig. 33. Sawing of Double-Edge-Notched specimens from square plates of 50 mm thickness.

In a later test series (viz. batch nos. 46, 47 and 48) the size effect in mixed-mode fracture was studied. Each batch consisted of six plates of size 300 × 300 × 50 mm^3 and 200 × 200 × 50 mm^3. The plates were cast in two different battery moulds and were cured as mentioned above. After 14 days, the plates were sawn into specimens of dimension 200 × 200 × 50, 100 × 100 × 50 and 50 × 50 × 50 mm^3 (each having a constant notch to depth ratio $a/d = 0.125$) as shown in Fig. 33b, c. Directly after sawing, the specimens were placed in a fresh water basin again. At an age of 28 days, the specimens were taken out of the water and left in the laboratory to dry until testing at an ambient temperature of 17–18 °C and 50% RH. Note that the drying time varied depending on the age of loading, which ranged from 42 to 216 days.
In Table 2, the 28 day cube compressive strength and the splitting tensile strength of the three materials are given. The strength results were obtained from 150 mm cubes as specified in the Dutch codes VB 74/84.

Table 2. Compressive strength, splitting tensile strength and specimen numbering for the various batches

batch	number of specimens (code)	d_{mqx} [mm]	f_{cc}* [MPa]	f_{spl}* [MPa]	size** [mm]
14	5(14-01/05)	2	46.59(1.37)	3.38(0.27)	200
15	5(15-01/05)	2	47.86(0.20)	3.68(0.07)	200
17	5(17-01/05)	2	46.49(1.58)	3.95(0.24)	200
18	5(18-01/05)	2	48.17(0.36)	3.56(0.27)	200
26	6(26-01/06)	2	46.68(0.48)	3.58(0.13)	200
27	6(27-01/06)	16	52.47(1.03)	3.61(0.15)	200
28	6(28-01/06)	12	49.59(0.41)	3.16(0.18)	200
29	6(29-01/06)	12	60.17(0.35)	4.15(0.64)	200
30	6(30-01/06)	16	58.75(2.62)	3.97(0.33)	200
32	6(32-01/06)	2	46.53(0.69)	3.47(0.28)	200
46	6(46-01/06)				200
	6(46-07/12)	2	49.66(2.23)	3.76(0.29)	100
	12(46-13/24)				50
47	6(47-01/06)				200
	6(47-07/12)	2	46.19(0.32)	3.78(0.23)	100
	12(47-13/24)				50
48	6(48-01/06)				200
	6(48-07/12)	2	46.24(0.37)	3.67(0.29)	100
	12(48-13/24)				50

* Numbers between brackets denote the standard deviation in [MPa].
** Only the largest size is mentioned. The specimens are square plates with a thickness of 50 mm.

3.2.2 Slurry Infiltrated Fibre Concrete (SIFCON)

Slurry Infiltrated Fibre CONcrete is a relatively new material. The material was first introduced by Lankard and Newell (see [46]), and applied successfully for the repair of bridge decks. Currently the material gained considerable attention in the research community, and investigators are looking for possible structural applications. In view of

this, the biaxial tension/shear experiments are meaningfull as they address the shear capacity and shear stiffness of cracked SIFCON.
Crucial in testing SIFCON is the manufacturing method of the specimen. In the present study the SIFCON specimens were manufactured in the same battery moulds that were used for casting the plain concrete specimens. First the fibres were sprinkled in the moulds. Two types of fibres, both manufactured by Bekaert, were used: viz. the straight OL 25/0.5 fibres and the hooked ZL 30/0.5 fibres. The numbers denote the length and the diameter (in [mm]) of the fibres respectively. Because the SIFCON plates were only 50 mm thick, the fibres would allign preferentially in horizontal directions. In Fig. 34 two photographs from a transparent plexiglass mould filled with ZL fibres are shown. In Fig. 34a, the front view is shown. The casting direction is vertical, and it can be seen that the fibres are alligned in horizontal planes. The side view of the plexiglass mould in Fig. 34b shows that a strong wall effect is present over the thickess of the plates. The cement

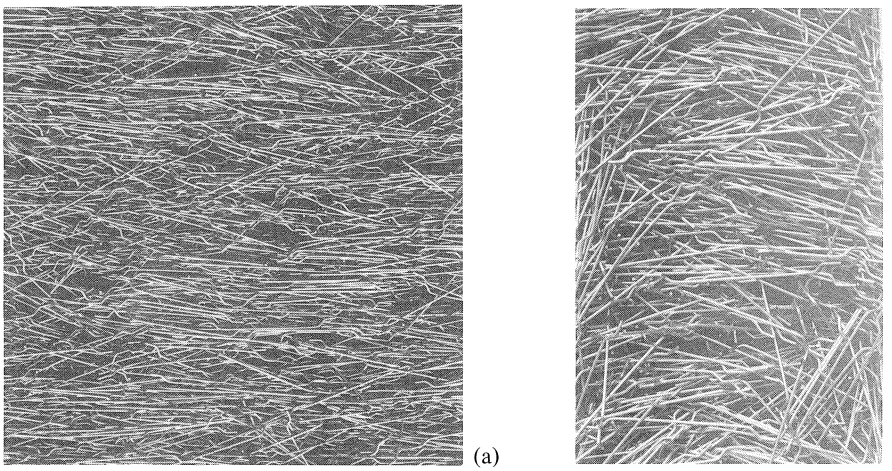

Fig. 34. Alligned fibre structure (ZL fibres), front view (a) and side view (b).

slurry (a normal sand/cement mix containing 978.6 kg/m^3 Portland cement type B; a w/c ratio of 0.39 (by wt.); 11.7 kg/m^3 Melment super plasticizer; and 822.4 kg/m^3 of sand with a maximum aggregate size of 125 μm) was poured along the sides of the moulds, allowing the air to escape from the centre of the plates as shown in Fig. 35. This manufacturing method implies that the plates are filled from bottom to top. In an experiment with a mould where one of the sides was replaced by a plexiglass plate it was found that following this method all air was removed quite easily, thereby reducing the vibration times.
During casting, the battery mould (now containing four plates only) was placed on top of a vibrating table. The moulds were fixed to assure that the vibrational energy was transfered directly to the fibre mass in the moulds. This was achieved by clamping the specimens on the table via supports that were placed directly on top of the fibre mass.

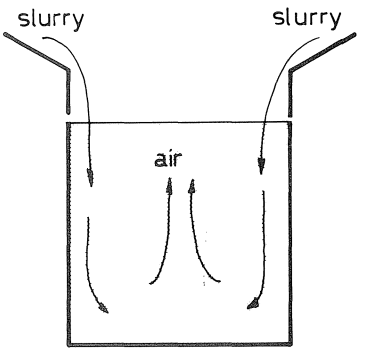

Fig. 35. Pouring the slurry in the narrow moulds.

Two views of the fibre distribution in the specimens after pouring the slurry are shown in Fig. 36. In Fig. 36a, a saw cut has been made parallel to the main fibre direction ($\alpha = 0°$, see Fig. 5.1), and in Fig. 36b, a section perpendicular to the main fibre direction is shown ($\alpha = 90°$). The anisotropy of the fibre structure will be obvious.
As mentioned two different types of fibres were tested: Dramix ZL 30/0.5 and Dramix OL 25/0.5. The ZL fibres have small hooks at the end to improve the bond between the fibres and matrix. The geometry of the fibres can be seen in Fig. 34. Because of the different shapes of the OL and ZL fibres, the mould contains different quantities: 11.47% and 9.57% (by volume) for the OL and ZL fibres respectively. The fibre volumes are the average quantities of four batches for each fibre type. The numbers indicate that - as expected - the hooked ZL fibres form a more entangled network than the straight OL fibres. The complete details, including the compressive and splitting tensile strengths, of the eight SIFCON batches are given in Table 3. Note that preceding these eight batches, several test castings were made (No. 1-9) before satisfactory results were obtained.

Table 3. SIFCON batches

batch No.	fibre type	fibre quantity [% by volume]	f_{cc} [MPa]	f_{spl} [MPa]
10	OL	11.00	- (-)	6.25(0.36)
11	OL	11.75	- (-)	6.43(0.96)
12	OL	11.25	70.2(7.66)	6.84(1.23)
13	OL	11.88	66.2(2.56)	5.57(0.75)
16	ZL	9.52	70.2(2.41)	6.07(1.10)
17	ZL	9.37	70.1(0.85)	6.65(0.19)
18	ZL	9.72	69.7(0.58)	6.81(0.96)
19	ZL	9.65	71.8(1.56)	5.96(0.49)

Note: f_{cc} = compressive strength and f_{spl} = splitting tensile strength from 150 mm cubes; both determined 28 days after casting. Curing under water at 20 °C. The strength values are the average values of three tests, the numbers between brackets denote the standard deviation.

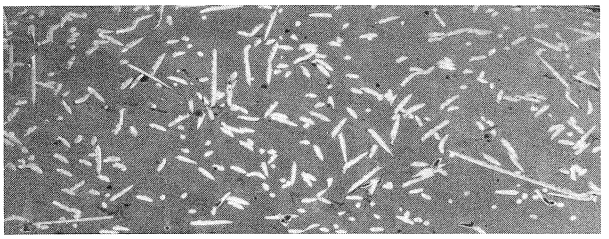

(a)

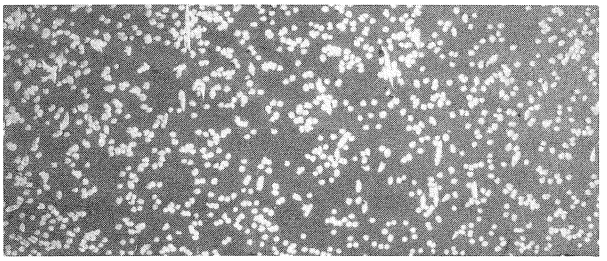

(b)

Fig. 36. Anisotropy in SIFCON specimens: sawcut at $\alpha = 0°$, and (b) at $\alpha = 90°$.

Each batch consists of four plates of size 300 × 300 × 50 mm^3 and six 150 mm cubes. The cubes were used for the determination of the reference compressive and splitting tensile strength following the Dutch codes VB 74/84. In the test castings, the vibration times were relatively long, but by using the method of Fig. 35 could eventually be reduced to approximately 6 minutes. Two days after casting the specimens were demoulded and placed in a fresh water basin in the laboratory (ambient temperature of approximately 18 °C). At an age of 14 days, the specimens were sawn to the required size. Two Double-Edge-Notched (DEN) specimens were sawn from each plate as shown in Fig. 37. The size of the SIFCON specimens was 100 × 100 × 50 mm^3. This size was selected because of its ease in handeling in the biaxial machine. Because the material was extremely anisotropic (Fig. 36), the loading was applied at various angles with respect to the fibre orientation. This was achieved by simply sawing the specimens in inclined positions from the plates. Note that the sawing of the SIFCON specimens is a tedious and time consuming task. In the beginning, in many specimens fibres were partly debonded at the edges during sawing. This was later (partly) prevented by carefully clamping the specimens between wooden plates during sawing. After sawing the specimens remained under water until an age of 28 days, whereafter they were allowed to dry in the laboratory atmosphere (appr. 50% RH). The age at testing was always larger than 49 days.

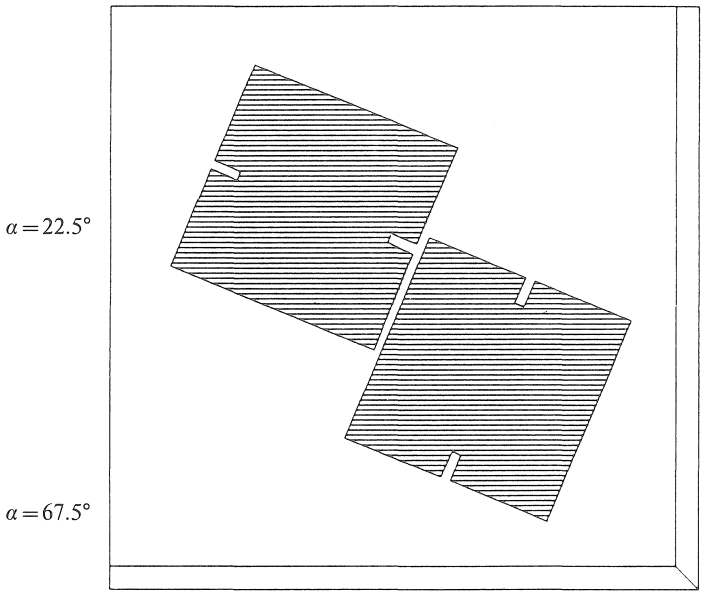

Fig. 37. Sawing DEN specimens with inclined fibres from square plates of 50 mm thickness; example of 22.5° and 67.5° specimens.

In addition to the SIFCON specimens, two batches of plain slurry were casted. In this case no reference compressive and splitting tensile strength were determined. Only a number of displacement controlled uniaxial tensile tests were carried out. In contrast to the SIFCON specimens, a number of the plain slurry specimens were kept in the water basin up till three days before testing. This was done because previous experiments showed that plain cement paste is very sensitive to shrinkage cracking if it is allowed to dry out at early ages, see [47].

4 Plain concrete results

4.1 *Introduction*

Nucleation and growth of cracks under combined tensile and shear loading has been studied with the biaxial test-rig of the Stevin Laboratory. Up till now seven different load-paths have been examined in order to better understand fracture mechanisms under biaxial loading. The unique feature of the test set-up in the Stevin Laboratory is that the two loading axes can be regulated completely independent of each other. Both displacement controlled and load controlled testing is possible as descibed before in chapter 3.

Testing concrete under mixed-mode I and II conditions is of great practical interest. Many existing structures are cracked, and in most cases shear stresses may be present

due to stress-redistributions in the cracked structure. In the past many attempts have been made to study the shear resistance of cracked concrete. As a result aggregate interlock theories have been derived for fully open cracks, see for example [31]. In the present experiments, the shear response of partially opened cracks is studied. The phrase partially opened indicates that still tensile stresses can be transferred in the direction normal to the crack plane. Of course, compared to the behaviour of fully opened cracks, the physics of the shear process will change, and next to pure sliding, secondary cracking may occur.

The early mixed-mode studies in the Stevin Laboratory were set-up with the aim of extending the Fictitious Crack Model of Hillerborg and co-workers [7] for mixed mode loading. To this end quadratic push-off type specimens were used by Reinhardt and co-workers [39]. Main goal of their study was to determine the shear characteristics of a specimen containing a uniform crack-band. As argued before in chapters 2 and 3, recent experiments have shown that uniform loading of a process-zone is impossible. The heterogeneous nature of the material will always lead to non-unifom fracturing. The push-off type specimen was selected in [39], because analyses by Watkins and Liu [48] had shown that an almost uniform state of shear stress could be obtained for specific ligament sizes. The first experiments revealed however S-shaped crack patterns, indicating that stress-rotations occur almost immediately after crack nucleation. The assumed mixed mode fracturing seems governed by the weakest link in the material: the tensile strength.

With all the problems of non-uniform fracturing, specimen/machine interactions and the dominance of tensile fracturing in heterogeneous materials as concrete, it was decided to select a more simple specimen geometry. The quadratic double-edge-notched plate was selected. The specimen size was initially taken as large as the machine could contain, in order to come to a better understanding of the intricate specimen/machine interactions. In later tests the size was reduced. Because of the dominance of the tensile stress in fracture tests on concrete it was decided to choose first load-paths where a crack was generated in tension, and subsequently shear was applied under a variety of boundary conditions. Later also the important question of the existence of mode II (shear) fracture was addressed, and several tests were carried out without pre-cracking the specimen.

In this chapter the results of the experiments on plain concrete are presented. First, in section 4.2 the terminology used throughout this chapter is summarised. As mentioned, seven different load-paths were studied. An overview of these load-paths is given also in section 4.2. In the following sections (4.3 through 4.6) the effect of shear on the tensile envelope curve, the influence of initial crack opening on shear resistance, the effect of confinement and specimen size are discussed. In section 4.7 the path-dependency of mixed mode fracture is debated. The shear stiffness of the cracked concrete was also studied, but these results are shown in chapter 6, together with the SIFCON shear results.

The study has a true exploratory character. Hardly any information is available on the shear behaviour of partially cracked concrete.

4.2 *Load-path description*

Seven different biaxial load-paths were studied up till now. In many cases the specimens were precracked in deformation control, whereafter under a variety of boundary conditions shear was applied either in displacement of in load control. The simplest load-path investigated was displacement controlled uniaxial tension.
Throughout this paper the following terminology has been used:

- *Compressive and tensile shear:* In classical mechanics literature shear can either be positive or negative. In the experiments on concrete usually non-planar and non-symmetric fractures develop in the specimen. When in-plane shear is applied, the behaviour may be different depending on the direction of the shear load. Therefore tensile and compressive shear are distinguished following the definition of Fig. 38.
- *Crack opening:* The total deformation measured can be subdivided in an elastic part δ_e and the crack opening δ_c. Therefore the true crack opening is the total deformation δ corrected for the elastic contribution δ_e. In this paper the total deformation has not been corrected for the elastic deformation.

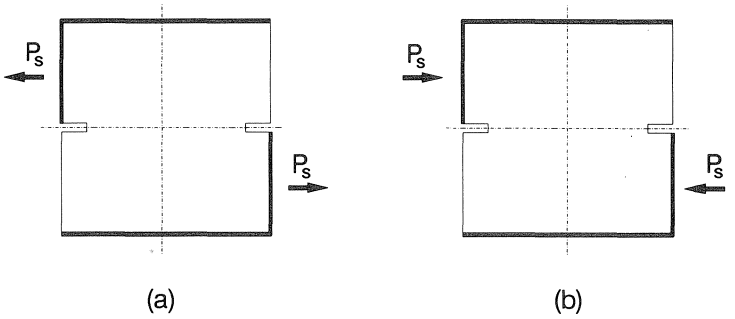

Fig. 38. Definition of tensile and compressive shear directions.

Below follows an exposure of the load-paths investigated to date. The load-paths are shown schematically in Fig. 39 in terms of $P - P_s$, $P - \delta$ and $\delta - t$ histories. The loading rates are mentioned in Fig. 39. Note that during an experiment, the loading rates (displacement control) were usually doubled two times in the post-peak regime.

4.2.1 Load-path 0: Uniaxial tension

The specimen, glued between the loading platens, is subjected to uniaxial tension. The tests are always carried out in displacement control (Fig. 39a). Two different situations are distinguished with regard to the loading platen configuration. In the simplest test, the specimen is glued at the top and bottom to two steel platens, see Fig. 40a. Because the specimen is fixed in a normal biaxial test on four sides, a number of load-path 0 tests has also been carried out on specimens glued to four loading platens as shown in Fig. 40b.

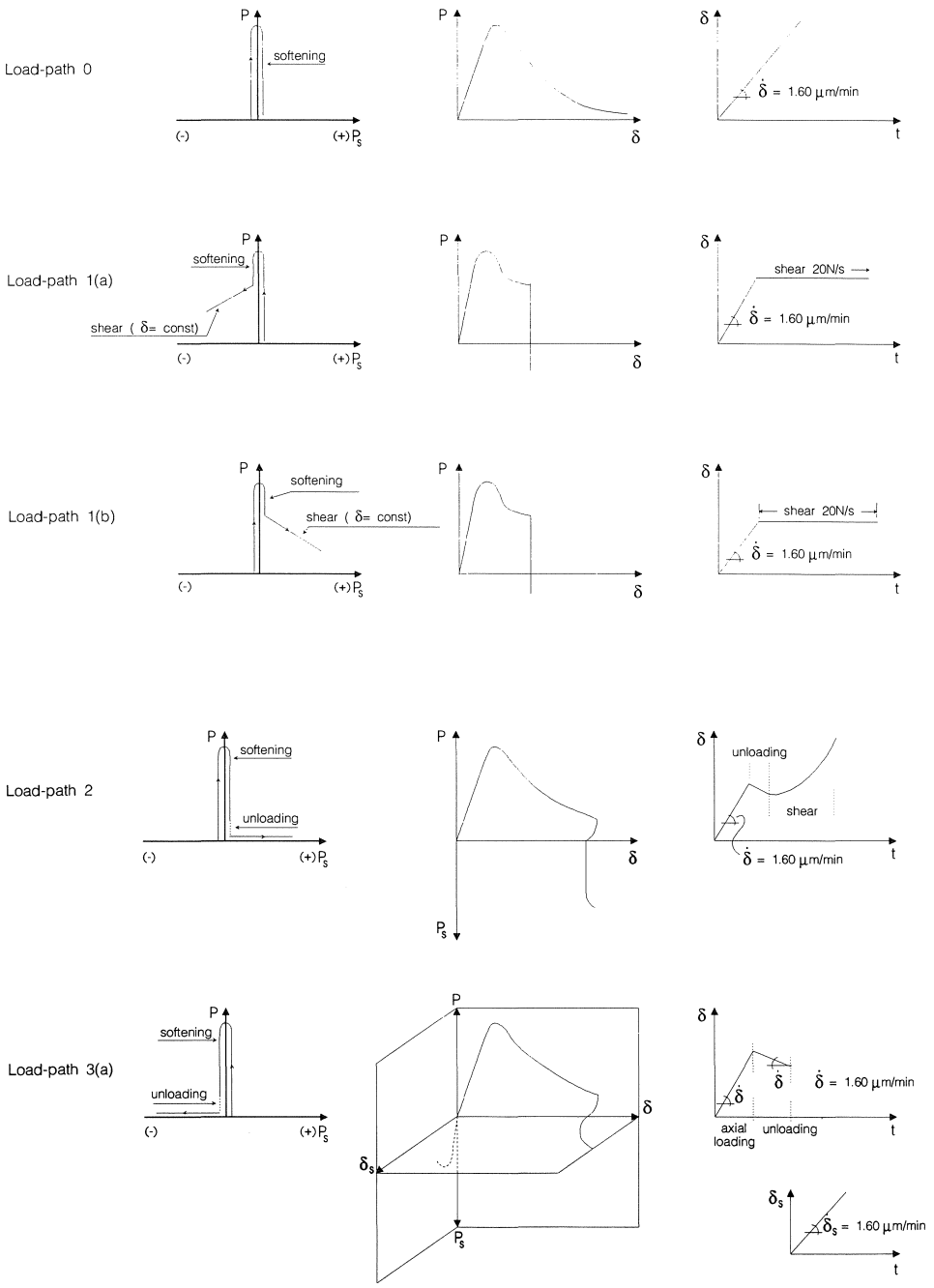

Fig. 39a–e. Schematic representation of load-paths 0, 1a, 1b, 2 and 3a.

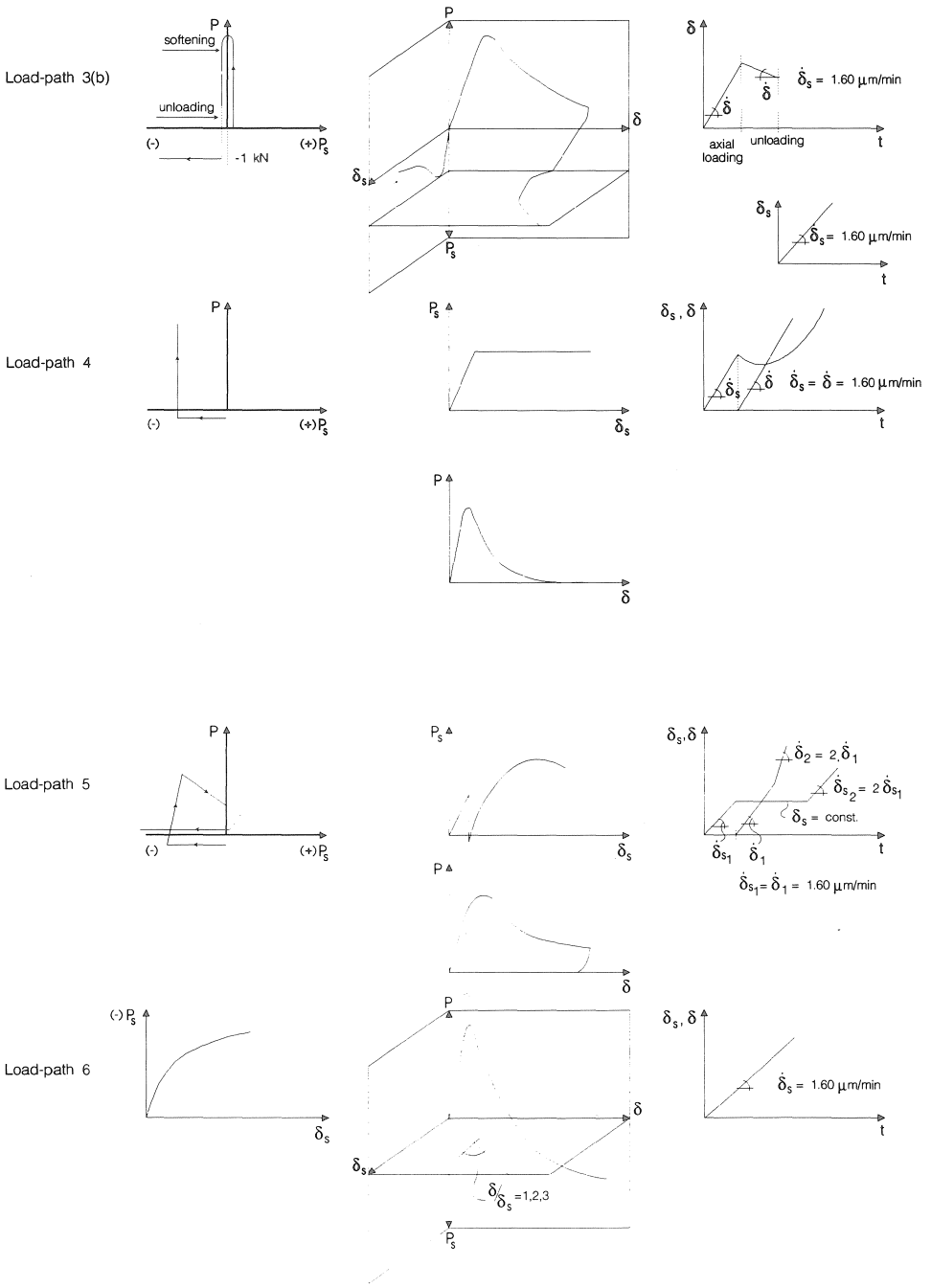

Fig. 39f–i. Schematic representation of load-paths 3b, 4, 5 and 6.

4.2.2 Load-path 1: Shear at constant crack opening

The specimen is first loaded in axial tension up to a prescribed crack opening δ_0. Subsequently the crack opening δ_0 is kept constant, and shear is applied in load control (Fig. 39b, c). The shear load P_s is applied at different levels of axial crack opening. In load-path 1a, the shear is compressive, in load-path 1b tensile shear is applied.

4.2.3 Load-path 2: Tensile shear at zero axial load

The specimen is first subjected to tension, in displacement control. After loading it to a prescribed axial crack opening, the specimen is unloaded to $P = 0$. Subsequently, the axial test control is changed to load contol, and shear is applied while maintaining $P = 0 =$ constant. The shear load is applied in load control (see Fig. 39d).

4.2.4 Load-path 3: Unconfined and confined compressive shear

Again the specimen is precracked to a given axial crack opening δ_0 in displacement control. Subsequently the specimen is unloaded, either to $P = 0$ (load-path 3a, unconfined) or to $P = -1000$ N (load-path 3b, confined), see Fig. 39e and f respectively. As soon as the axial load is reached, shear is applied in displacement control while the axial load is kept constant. In load-path 3b, the axial confinement of -1000 N corresponds to a small confining stress of -0.13 MPa normal to the crack plane.

4.2.5 Load-path 4: Axial tension at constant shear force

A compressive shear load is applied to the specimen in displacement control until $P_s = -5$ (load path 4a), -10 kN (load-path 4b) or $P_{s,max}$ (load-path 4c). During shear, $P = 0 =$ constant. $P_{s,max}$ is the maximum shear load the specimen can sustain. Following this, the specimen is fractured in tension, in displacement control, while maintaining $P_s =$ constant at one of the above loading levels (see Fig. 39g).

4.2.6 Load-path 5: Axial tension at constant shear deformation

This load-path is similar to load-path 4, except that in both directions displacement control is maintained. Again P_s is applied until a prescribed value: $P_s = -5$ kN (load-path 5a), $P_s = -10$ kN (load-path 5b) and to maximum shear (load-path 5c). During shear, $P = 0 =$ constant. Subsequently the specimen is fractured in displacement control in tension, while maintaining the lateral shear displacement constant (see Fig. 39h).

4.2.7 Load-path 6: Proportional loading

A specimen is loaded such that the ratio of axial deformation δ and shear displacement δ_s remains constant throughout the experiment. The δ/δ_s ratio's for load-paths 6a, 6b and 6c are 1.0, 2.0 and 3.0 respectively (see Fig. 39i).

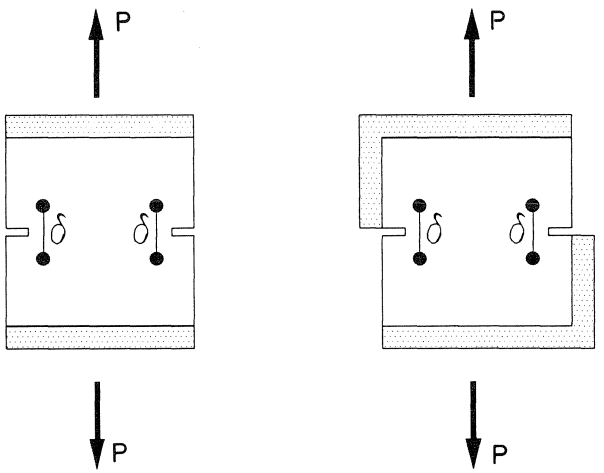

Fig. 40. Uniaxial tensile test (load-path 0) between two (a) and four loading platens (b).

4.3 *Influence of shear on the tensile envelope curve*

In the first experiments it was investigated whether the application of a shear load would affect the tensile softening curve. To this end two different load-paths were followed, now designated 1a and 1b. In these early tests, the shear load was applied in load control, and no stable fracturing in shear could be obtained. Therefore, well before the specimen was expected to fail, it was unloaded and in several tests cyclic unloading was repeated a number of times.

Two examples of tension-compression tests on 200 mm DEN specimens are shown in Figs. 41 through 43. In these figures the P-δ curves (Fig. 41), the load-path $P-P_s$ (Fig.

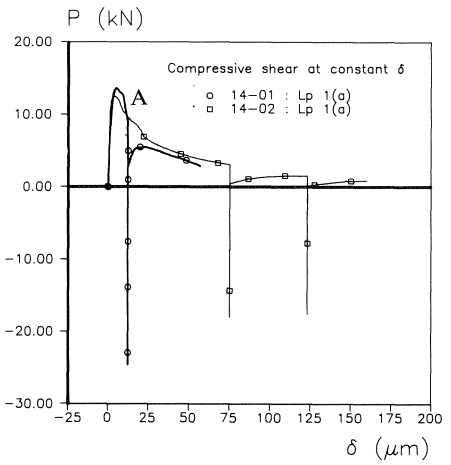

Fig. 41. P-δ diagrams for two compressive shear tests at δ_0=constant (load-path 1a).

42) and one of the crack patterns after test termination (Fig. 43) are shown. Results are given of two different experiments (1401 and 1402). The changes in loading sequence are shown in the inset of Fig. 41. First a specimen was pulled, in displacement control, to a prescribed axial deformation δ_0. As soon as this point on the tensile softening curve was reached (A), compressive shear was applied while maintaining $\delta_0 =$ constant. Because the crack was not allowed to open during shear, a compressive confinement would develop in the axial loading direction as can be seen from Fig. 41. Upon (shear) unloading at constant δ_0, the axial compressive load was released, and at some stage the axial softening envelope was reached again. At this moment the lateral shear was zero, and the specimen was loaded further along the envelope curve. The curves shown in Fig. 41 indicate that the static envelope curve is reached again after the shear loading. This would mean that at these levels of shear loading no additional damage is done to the specimen. Note that the compressive shear load P_s could not be increased over 50 kN, which was the loading limit imposed by the design of the biaxial machine. The impression was that the specimen could carry a substantially higher shear load. As can be seen from Fig. 42, the state of stress in the specimen during application of shear is compression-compression. A rough estimate is that the specimen would fail as soon as

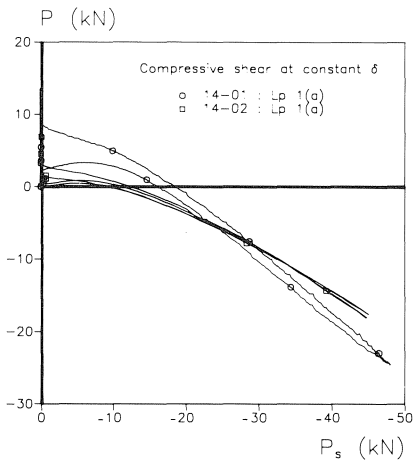

Fig. 42. Load-paths P-P_s for the two tests of Fig. 41.

the maximum biaxial stress in the specimen was reached. Comparison with for example Kupfer's results [49], shows that the current stress levels are still very low: approximately -2 and -6 MPa in the axial and lateral directions respectively. For the concrete tested, the biaxial strength is estimated above -50 MPa on the basis of Kupfer's results. Even if the biaxial strength envelope would be reduced due to the tensile crack that was present in the specimen, than still these stress levels are considered very low.
The two results of Fig. 41 are almost identical. Shear loading and unloading at different values of δ_0 does not seem to affect the tensile softening envelope.

The crack pattern traced from the specimen 1402 after test termination is shown in Fig. 43. In both experiments a single crack developed, and no additional cracking seemed to occur under shear loading. Of course this is no surprise because the stress state in the specimen changes from tension-compression to compression-compression as soon as shear is applied.

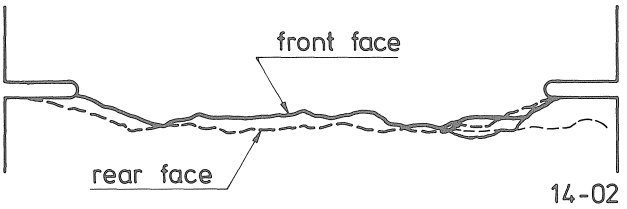

Fig. 43. Crack patterns for experiment 1402, load-path 1a.

As mentioned, the shear displacements were not measured in these pilot tests. Consequently no information on shear stiffness reduction can be obtained from these experiments.

Because of the limitations in the biaxial test-rig, the specimens could not be failed under compressive shear (load-path 1a). Therefore it was decided to carry out some experiments under tensile shear. An example of a tensile shear experiment is given in Fig. 44. This particular specimen (1504) was loaded in displacement control to $\delta_0 = 11.6$ μm and 23.4 μm respectively. At these points, the lateral shear was applied in tension (in load-control) while maintaining $\delta_0 =$ constant. In the first shear cycle, only moderate levels of shear-load were allowed in order to avoid premature failure of the specimen. During the experiment crack growth was monitored using reflection photo-elasticity. A

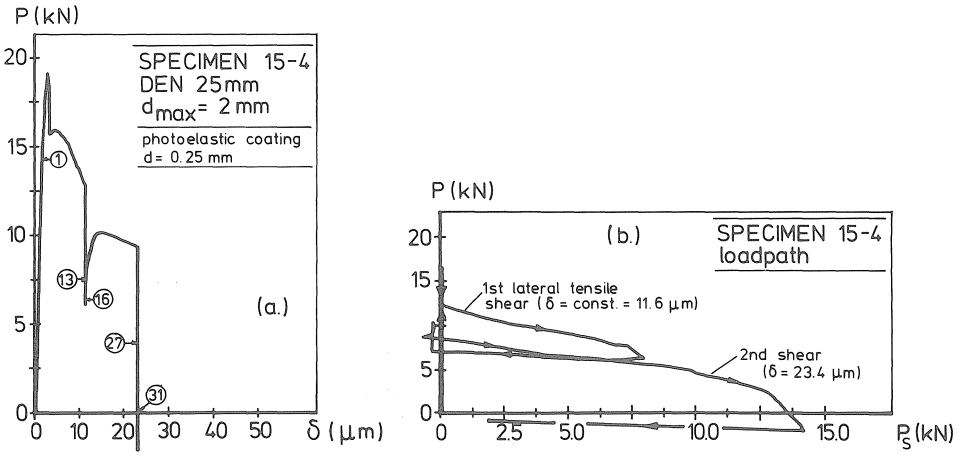

Fig. 44. P-δ and P-P_s diagrams for tensile shear test 1504 at δ_0=constant (load-path 1b).

reflective coating of photo-elastic material was glued to the specimen's surface. Under polarized light, the isochromatics changed at places where cracks developed. Although the resolution of the technique is not very high, it can be used for correlating the extent of surface cracking with the load-deflection behaviour of the specimen. The method was used successfully for monitoring crack growth in DEN specimens loaded in uniaxial tension (see [12] and [50]). In test 1504, the first fringes were observed near the left notch when the specimen was still in the ascending branch. At $\delta = 10$ μm, a complete crack traversed the specimen between the left and right notch (Fig. 45a), and as soon as tensile shear was applied the small diagonal crack shown in Fig. 45b developed. At the same moment a small diagonal crack nucleated from the top of the left notch. Under increasing shear, the crack at the left notch extended further as can be seen from the other crack patterns (Fig. 45c-e). Final failure was not along the left diagonal crack but through unstable extension of the diagonal crack near the right notch. The load-crack opening diagram $(P - \delta)$ of Fig. 44a shows that after a shear cycle, the tensile envelope curve is followed again. This illustrates that no additional cracking occurs in the plane of the primary (tensile) crack. Moreover, the result indicates that the shear resistance of the partially opened crack is still relatively high, and failure of the specimen through diagonal cracking prevails.

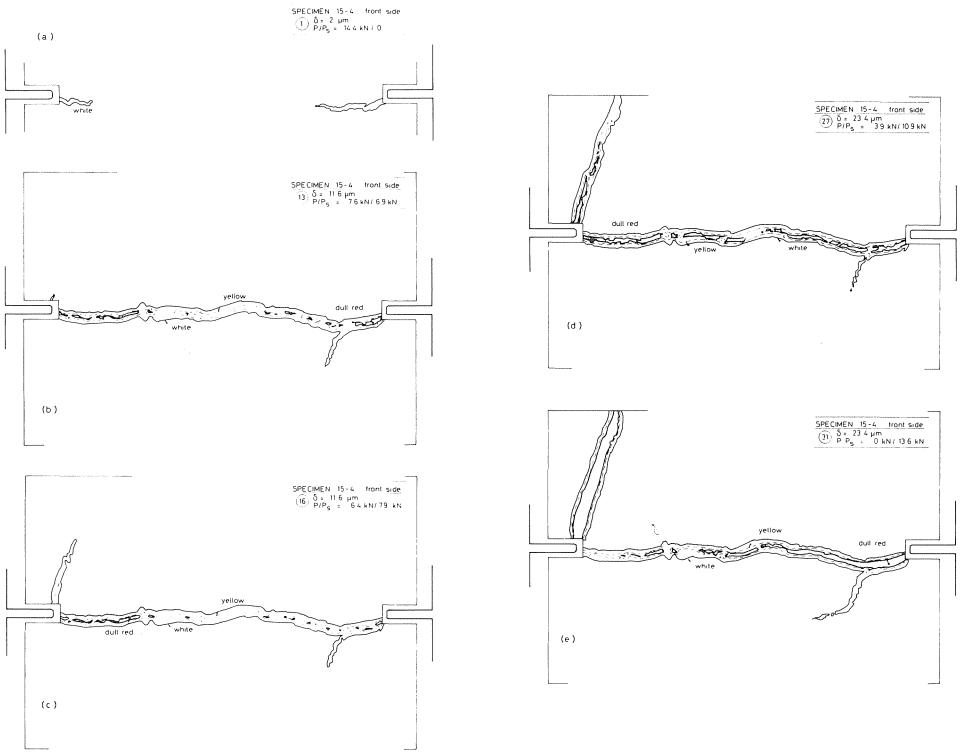

Fig. 45. Cracking during test 1504. The respective stages of loading are indicated in the right upper corner of each figure, and correspond to the numbers in Fig. 44.

Note that the crack in the specimen nucleated at the front face. This was explained before in chapter 3. The relative in-plane and out-of-plane stiffnesses of the specimen/machine system and possibly the introduction of some additional eccentricities when the specimen is glued between four loading platens, may lead to this out-of-plane bending. During the experiment 1504, crack growth was also monitored (using the same reflection photo-elastic method) at the back side of the specimen. Here it was found that at the onset of shear loading, the axial tensile crack had developed only partly, see [50]. The diagonal cracks at the back side developed at approximately the same locations as compared to those at the front side of the specimen.
Several load-path 1b experiments were carried out, and three different results are given in [5]. In all cases, a diagonal tensile crack nucleated either near one of the notches, or from a sharp kink or discontinuity in the primary tensile crack. The load-deformation response for the experiments was however quite similar.
The inclination of the "shear cracks" indicates that a rotated biaxial tension/tension state of stress governs the failure of the specimen. The load-path $P-P_s$ (Fig. 44b) indicates that final rupture occurred in the tension-compression regime. Again this should be expected (qualitatively) on the basis of Kupfer's results [49].

4.4 *Influence of crack opening on shear behaviour*

The effect of crack opening δ_0 on the shear resistance and shear stiffness of cracked concrete was investigated using load-paths 2 and 3. In load-path 2, tensile shear was applied in load control after a specimen of size 200 mm was precracked to a given crack opening δ_0. During shear the load normal to the crack plane was kept constant at zero. This allowed for an unrestrained opening of the crack during shear.
In load-path 3, compressive shear was applied in displacement control (note that the machine was modified in between of the load-path 2 and 3 experiments in order to allow for displacement controlled shear loading). Again the specimen was precracked to a given axial crack opening and unloaded to either 0 kN or to -1 kN confinement normal to the crack plane.
The load-path 2 experiments revealed the shear resistance of concrete containing narrow cracks between 10 and 400 μm. The load-path 3 experiments yielded information concerning the shear stiffness of the cracked concrete under confined and unconfined conditions.

4.4.1 Tensile shear

The results of the load-path 2 experiments are shown in Figs. 46 and 47. In Fig. 46a the axial load-displacement diagrams are shown, in Fig. 47 the crack patterns for all experiments. The diagrams can best be explained by following a specific test. For example in test 1704, axial loading was applied till $\delta_0 = 65$ μm. At this stage the specimen was unloaded to $P = 0$, and the displacement control was changed to load control. In Fig. 46a both the loading and unloading curve are shown. Following the axial loading, lateral

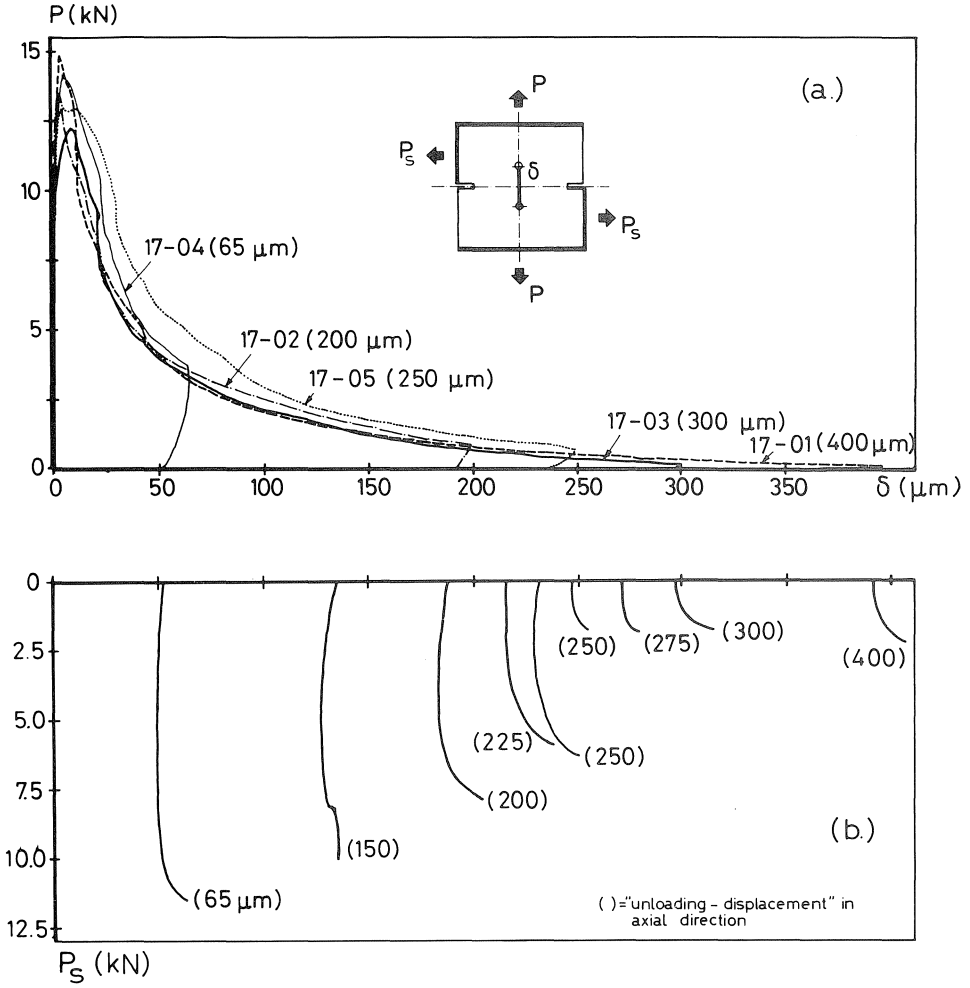

Fig. 46. P-δ (a) and P_s-δ plots (b) for tensile shear experiments at $P = 0 =$ constant (load-path 2).

shear was applied in load control, and the curve of Fig. 46b is measured. During shear, some uplift occured as can be seen from the increase of axial deformation. The specimen would fail as soon as the maximum shear load was reached. Fig. 46a shows that diagonal cracks developed in specimen 1704 during the shearing regime. The horizontal crack between the notches developed during the axial tensile loading. Obviously, the shear resistance of this narrow crack (note: the axial crack opening at shearing was somewhat smaller at $P = 0$, viz. 55 μm), was relatively large and failure of the specimen occurred through diagonal cracking rather than through sliding.

The shear behaviour was consistent throughout all experiments, except that at crack openings larger than 250 μm, the failure mode changed from diagonal cracking to sliding. This can easily be seen from the crack patterns in Fig. 47. Surprisingly the

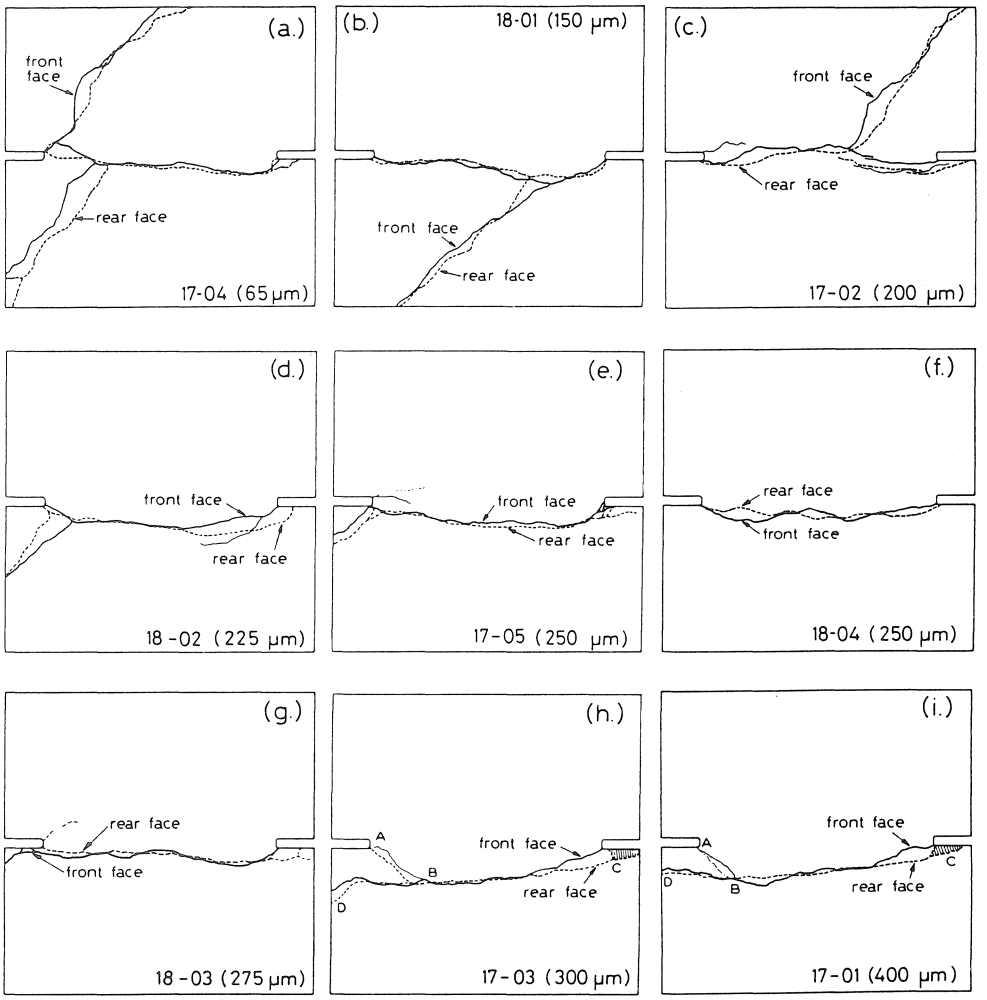

Fig. 47. Crack patterns for the load-path 2 experiments of Fig. 46.

change in failure modes near crack openings of 250 μm was accompanied by a sudden decrease in maximum shear-load. Note that two duplicate tests at $\delta_0 = 250$ μm were carried out. One of the specimens failed at a relatively high shear load, whereas the other failed at a low shear loading through sliding.

4.4.2 Compressive shear

The same phenomena were investigated in the load-path 3 experiments. However, now the shear load was compressive, and three different materials were tested at different ranges of axial crack opening, see Table 4. The test scheme was considerably reduced

because only two or three biaxial tests could be carried out in one week. The range of crack openings for the 2 mm mortar was chosen around the transition point of 250 μm in the tensile shear tests (load-path 2).

Table 4. Compressive shear tests (load-path 3)

crack opening	δ_0 [μm]	50	100	150	200	225	250	275	300	400
material	confinement during shear									
2 mm mortar	0					* *	* -	* *		
	−1 kN					* -	- -	* *		
16 mm concrete	0				* -				* -	* -
	−1 kN				* *				* *	* -
12 mm lytag	0	* -	* -	* *						
	−1 kN	* *	* *	* *						

Note: every variable combination is tested in duplicate; (-) test rejected because of too large off-set δ_s during tensile loading; (*) successful test.

For the 16 mm concrete, a wider range was chosen, viz. between 200 and 400 μm. It was not certain whether a similar transition would occur at exactly the same point for the 2 and 16 mm mixes. The lytag lightweight concrete was expected to behave very brittle. Therefore, δ_0 was chosen at relatively low levels for this material, viz. 50, 100 and 150 μm. It is now known that the lytag behaves, at least in tension, as a 4 mm mortar (see [19] and Fig. 7). The 4 mm maximum aggregate size refers to the size of the sand in the lytag mix.

The results for the 12 mm lytag are shown in Figs. 48a, b, c. The results for unconfined shear will be discussed here, a comparison with the confined tests will be given in section 4.5. In Fig. 48a and b the P-δ and P_s-δ_s curves for three lytag experiments are shown. The scatter in axial P-δ diagrams is relatively small; note that the three unloading displacements can easily be seen from Fig. 48a. The shear curves indicate that the shear resistance (maximum shear load) decreases with increasing axial crack opening, which should be expected on the basis of the load-path 2 experiments. Because relatively large off-sets (defined as the amount of shear displacement δ_s during axial tensile loading) were measured in some of the lytag experiments, only three results were considered acceptable. The other three unconfined tests showed unacceptable large shear displacements during the application of the axial tensile load, and these results were rejected. The off-set is most likely caused by small eccentricities in the test set-up. For example small eccentricities may appear during the glueing of the specimen in the machine or when deviations occur from the exact specimen dimensions. A result was rejected when the offset was larger than 30 μm, and from the total series 10 out of 36 results were not included in the analysis as can be seen from Table 4 (see also [51]). The δ-δ_s plots for the three unconfined lytag tests are shown in Fig. 48c. From this figure the following observations can be made. First, the unloading of a specimen after loading it to a certain axial crack opening is visible. This all happens along the $\delta_s = 0$ axis. When shear is applied, δ_s increases, and generally during the first 10 μm closure of

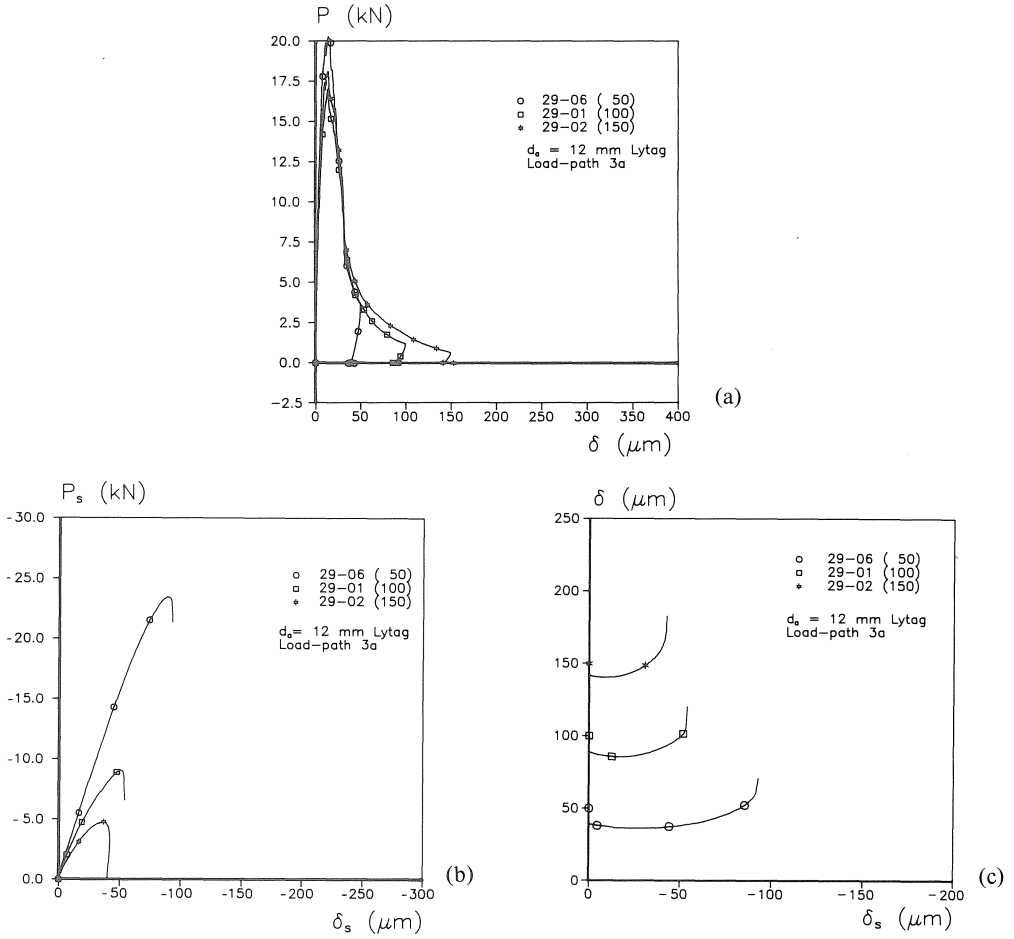

Fig. 48. P-δ (a), P_s-δ_s (b) and dilatancy plots δ-δ_s (c) for unconfined compressive shear tests on lytag (load-path 3a).

the axial crack is observed. Subsequently, the shear displacement increases under increasing shear load, but the crack opening remains almost constant. Only when P_s reaches its maximum value, a sudden increase of uplift is measured. Because no confinement is present normal to the crack plane, the specimen will fail as soon as uplift starts. In all unconfined tests a similar response was measured, see [5]. The crack patterns traced from the unconfined lytag experiments after failure are shown in Fig. 49. In all cases, a single crack plane was observed between the two notches.

The maximum shear loads in the unconfined tests were remarkably constant. If all experiments of the three different materials are considered, an average maximum shear load of approximately – 5 kN is measured. This value is comparable to the maximum load measured in the tensile shear tests (load-path 2), at least when failure occured through sliding (see Fig. 48b, and [5] for 2 mm mortar and 16 mm normal concrete). The

only exceptions are the 50 μm and 100 μm unconfined lytag tests (2906 and 2901, see Fig. 48a, b), which failed at a higher shear load level. Especially the shear loading of the 50 μm unconfined lytag test was relatively high, a level which could not be reached in the tensile shear tests for obvious reasons. The high shear load can probably be explained from the fact that the specimen was not completely cracked at the moment that shear was applied. Note that recent impregnation tests indicated that at $\delta_0 = 50$ μm, an intact core may be present in the specimens, see [17]. The results indicate that the sliding failure mechanism is prevalent in the unconfined *compressive* shear tests. Of course this remark is valid for the range of crack openings studied. In future, more experiments should be carried out at crack openings between 10 and 50 μm.
In none of the unconfined shear tests secondary cracking was observed as can be seen from the crack patterns (Fig. 49).

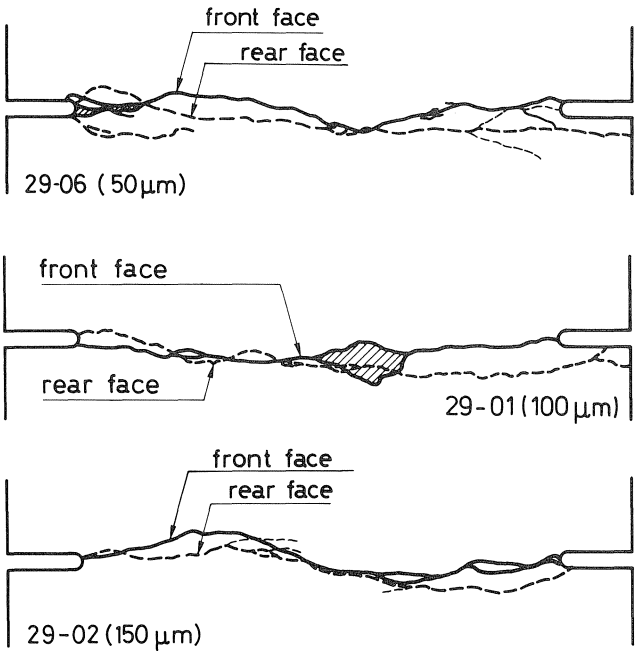

Fig. 49. Crack patterns for the three load-path 3a experiments of Fig. 48.

4.5 *Influence of confinement*

The various experiments that were carried out included tests with confinement normal to the crack plane under shear loading (load-path 3b), but also tests with "shear confinement" under axial tension (load-paths 4 and 5). In this paragraph these results will be presented. The load-path 3b results will be presented in section 4.5.1, the load-path 4 results in section 4.5.2.

4.5.1 Confinement normal to the crack plane

It is interesting to see how the failure of a specimen is governed by the presence of a confining stress normal to the crack plane. In the present tests a relatively low confinement acted normal to the crack, viz. - 0.13 MPa only. The confining stress was chosen at this low level in order to avoid that the specimen could not be failed in shear. Note that in the load-path 1a tests could not be failed in shear because of the biaxial compressive state of stress in the specimen.

In Figs. 50 and 51 results of the confined lytag tests are shown (load-path 3b). In this case all six tests were successful and these results are included in these figures. The axial load-deformation response is identical to the P-δ behaviour measured in the unconfined experiments (Fig 48a). Clearly visible is the constant confinement of – 1000 N after unloading, see Fig. 50a. Due to the application of the confining stress, the axial

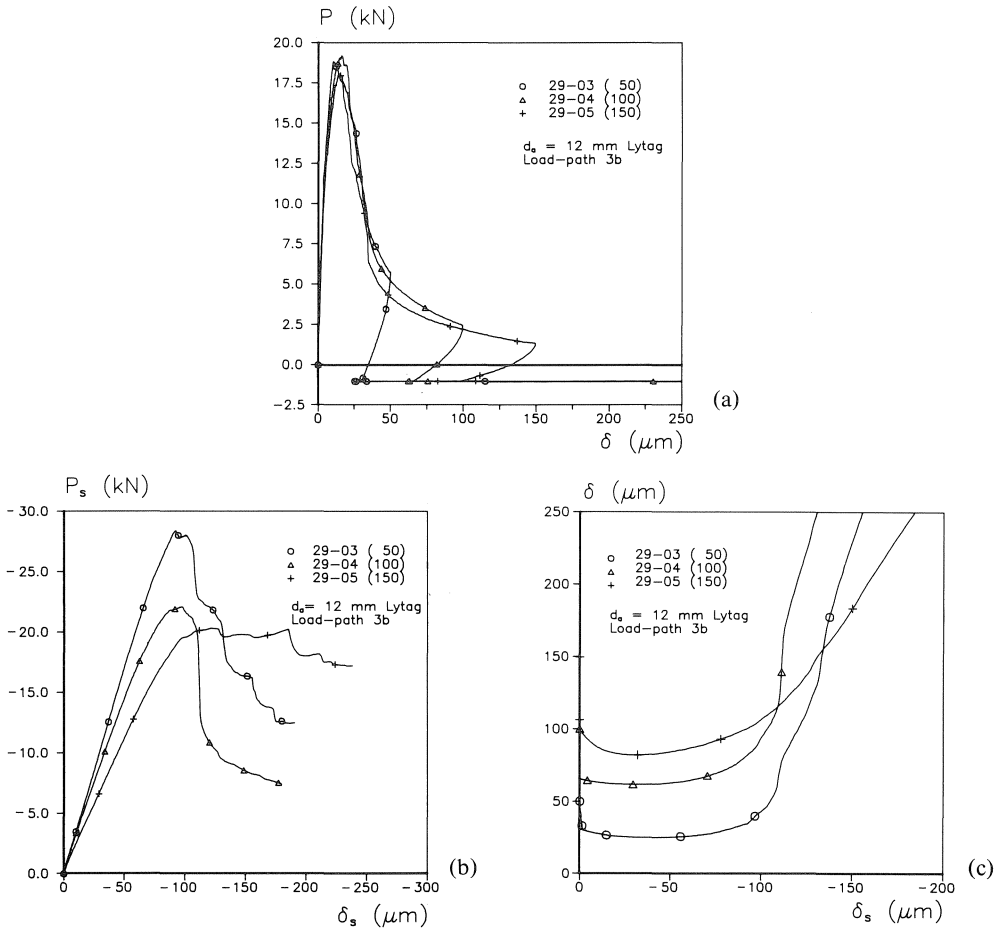

Fig. 50. P-δ (a), P_s-δ_s (b) and dilatancy plots δ-δ_s (c) for confined compressive shear tests on lytag (load-path 3b).

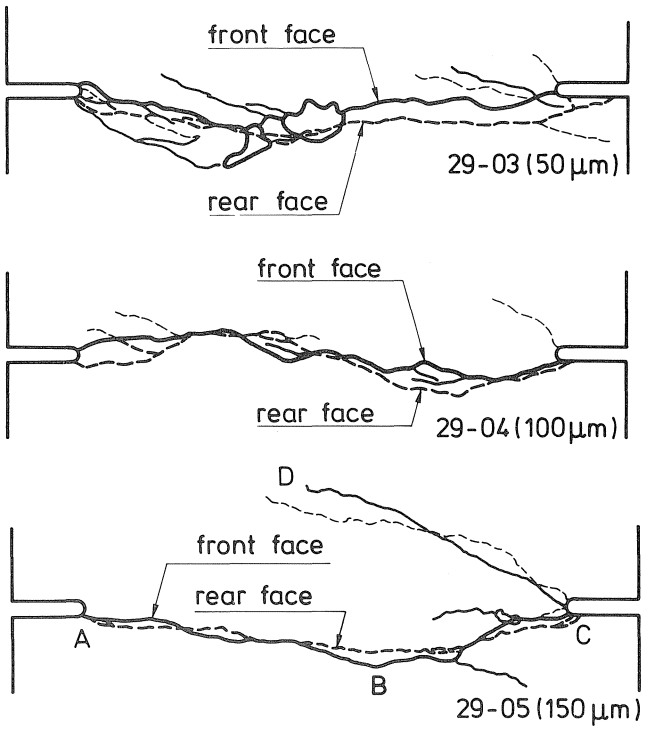

Fig. 51. Crack patterns for the three load-path 3b experiments of Fig. 50.

crack opening at onset of shear application was reduced by approximately 30% when compared to the value of δ_0. For the tests of Fig. 50, the axial crack opening immediately before shearing was 32.6, 30.0, 65.4, 65.2, 108 and 98.6 μm for specimen 3004 ($\delta_0 = 50$ μm), 2903 (50), 2904 (100), 3001 (100), 3003 (150) and 2905 (150) respectively. Again, after shear was applied, the axial crack would close slightly for very small shear displacements as shown in Fig. 50c. Following this closure, an increasing shear displacement was measured under increasing shear load, whereas the axial deformation remained almost constant. Only around peak ($P_{s,max}$), the axial crack opening would increase again. In comparison with the unconfined compressive shear test, this axial crack opening was controlled, and no explosive failure of the specimen would occur. Clearly the P_s-δ_s figures indicate that the fracturing in shear under confined conditions is more ductile, and the descending branch in the P_s-δ_s diagrams increased with increasing axial crack opening δ_0.

The reason for this latter effect can perhaps best be explained from the crack modes observed in the respective experiments. The crack patterns in the duplicate test were almost identical and only three crack patterns are shown in Fig. 51. Due to the application of the compressive shear load, extensive crack branching was observed. The details of the branches depend strongly on the geometry of the axial tensile crack. For example in the 150 μm specimen (Fig. 51c), crack A-B-C developed during the axial loading of

the specimen. Crack C-D nucleated as soon as shear was applied, and as will be shown in chapter 5, similar phenomena appeared in the SIFCON experiments. The branching developed either near the right notch, or somewhere from the middle of the tensile crack where a strong discontinuity or kink appeared, as for example visible in Fig. 51b. Surprisingly, the ductility (P_s-δ_s) increased with increasing axial crack opening. This phenomenon can most likely be explained from the mechanism of Fig. 52: depending on the local crack geometry a larger or smaller compressive strut may develop in the specimens. More or less parallel to this strut, a splitting crack will develop. If the crack patterns of Fig. 51 are studied carefully, it can be seen that the compressive strut size increases with axial crack opening. Probably this is purely accidental. On the other hand it might be argued that in the 50 μm specimens still axial stress was transfered through an intact core in the specimens (see [17]). In that case, the compressive shear load would be carried by the intact portion of the ligament between the notches and a more distributed cracking would prevail. In the 150 μm specimens, the separation of the crack faces was probably almost complete, and the shear resistance would depend completely on the carrying capacity caused by the local roughness of the tensile crack.

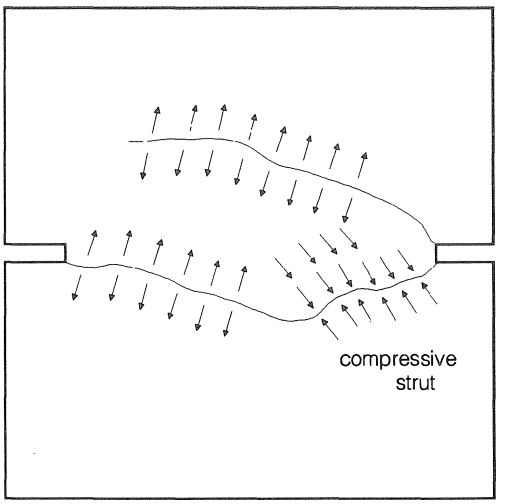

Fig. 52. Failure mechanism (schematic) in the confined compressive shear tests of Figs. 50 and 51.

The results of Fig. 50b indicate that the initial slope of the P_s-δ_s curves decreases with increasing axial crack opening. This same tendency was found for the unconfined tests as well, see Fig. 48. In the confined tests on the two other materials, this tendency was present as well (see [5]). The shear stiffness analysis will be given in chapter 6.

4.5.2 Confinement in the lateral shear direction

Load-path 4 was the first loading sequence where specimens were not precracked. In these experiments, first a lateral shear load was applied until a given level was reached. After this shear load level was reached, P_s was kept constant and the specimen was fractured in displacement control in the axial direction. The shear load acted now as a lateral confinement, although of course this was a rather unsymmetric confinement. The P- δ, P_s-δ_s and δ-δ_s curves for three load-path 4 experiments on 2 mm mortar are shown in Fig. 53. From Fig. 53a, the moment of application of the axial tensile load can easily be identified. The P_s-δ_s curve in this figure show large non-linearities when $P_s < -20$ kN, which is about 60% of the "shear strength" of the 200 mm DEN specimens. The definition of shear strength is somewhat dangerous, because undoubtedly

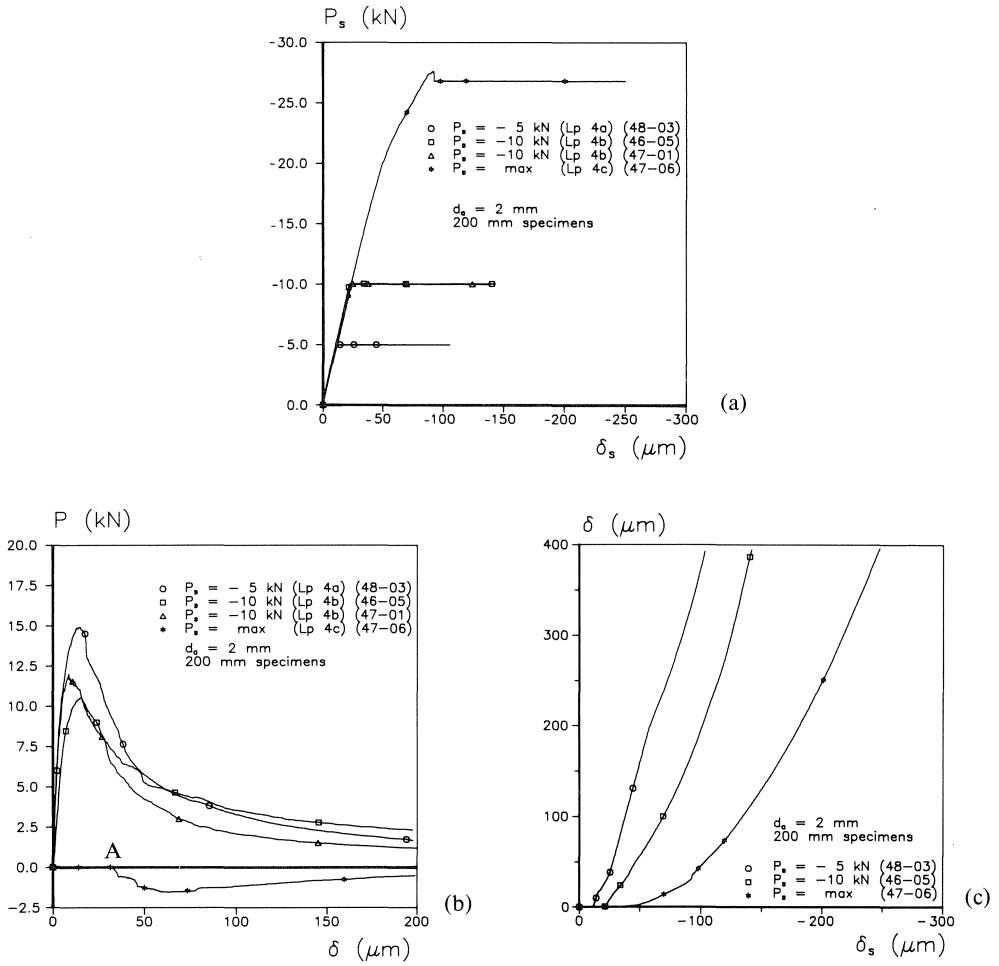

Fig. 53. P_s-δ_s (a), P-δ (b) and dilatancy plots δ-δ_s (c) at different levels of constant lateral shear confinement (load-path 4a, b and c).

a somewhat rotated biaxial state of stress will be present near the notches. The extensometers showed that in the load-path 4c specimen, cracks initiated from the left notch. Consequently, in this experiment axial deformations were measured during the shearing regime. The axial deformation that took place during shearing was relatively large as can be seen from the P-δ plot for load-path 4c in Fig. 53b (point A). From the local deformation measurements in the load-path 4a and 4b experiments, it was evident that no tensile cracking occured in the notched region during the application of the shear loads. This is confirmed by the linear P_s-δ_s curves for these two tests, see Fig. 53a. The corresponding P-δ curves of these three load-path 4 experiments are shown in Fig. 53b. Increasing the lateral shear load from -5 kN to -10 kN results in a decrease of

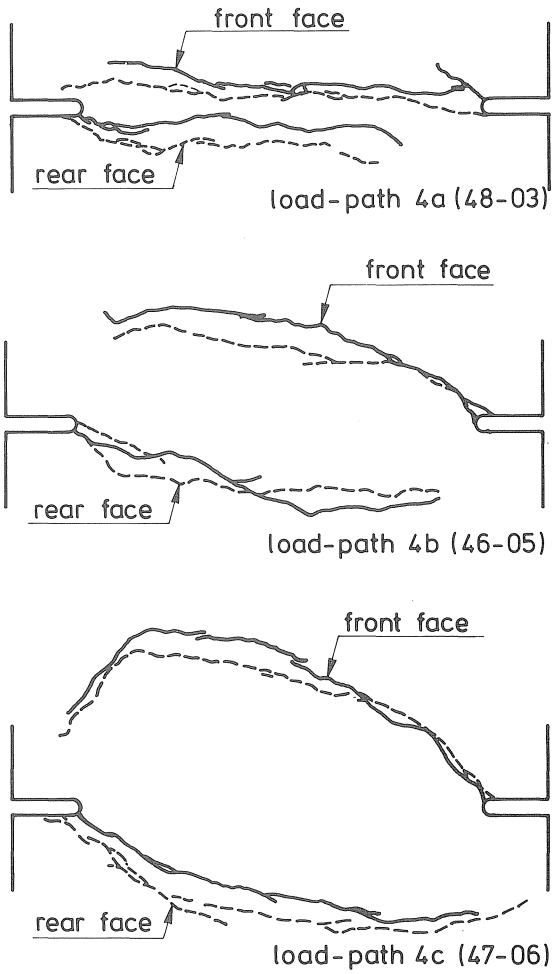

Fig. 54. Crack patterns for the load-path 4 experiments of Fig. 53.

tensile carrying capacity of approximately 30%. Further increasing the lateral shear to $P_{s,max}$ leads to an enormous decrease of carrying capacity, and in order to stabilize crack-propagation in the load-path 4c experiments, compressive stresses were needed. It may be concluded that the presence of a lateral compressive shear load has a significant effect on the tensile strength of the DEN specimen. Again, based on (qualitative) considerations this should be expected. The specimen is in a biaxial tensile-compressive state of stress, and Kupfer's results [49] clearly show that the failure envelope is considerably reduced under this biaxial loading.

In Fig. 54, the crack patterns traced from the specimen's surfaces after test termination are shown for the three tests of Fig. 53. The effect of a shear load on failure mode is significant: the size of the intact ligament between a set of overlapping cracks increases with increasing shear load. Note that in the case of load-path 4c ($P_s = P_{s,max} =$ constant), the two overlapping crack branches developed during the application of the shear load. During shearing, the axial load P was kept constant at 0 kN, and the axial deformations were unrestrained. This situation resembles the loading of a double notched four-point-shear-beam, as for example those tested by Bažant and Pfeiffer [25]. In [25], the development of a single shear crack was reported, but based on the present load-path 4 results, where shear is applied to failure, the findings of Bažant and Pfeiffer seem somewhat debatable. Most unfortunately a proper documentation of failure modes in [25] is lacking, and also no efforts were undertaken to carefully monitor crack growth during the experiment. It is the author's opinion that some of curved cracks may have developed in the Bažant and Pfeiffer tests, and that explosive failure of the ligament occurred. This secondary failure might (mistakenly) be regarded as a shear fracture. Future research is needed to further clarify this point.

4.6 *Size effect under biaxial loading*

Recently, the size effect on failure and localization of brittle disordered materials such as concrete has gained more interest. In conventional strength theory, the influence of the size of the structure on nominal strength σ_N is neglected. In a log σ_N-log (size) plot the strength criterion appears as a horizontal line as shown in Fig. 55. On the other hand, linear elastic fracture mechanics predicts that the structural strength is size dependent: $\sigma_N = C/\sqrt{d}$, where C is a constant and d is the characteristic size of the structure. In the log-log plot of Fig. 55, the LEFM criterion appears as a straight line with slope $-1/2$. As argued by Bažant [52] on several occasions, the size effect is the salient property of fracture of brittle disordered materials. The fracture of reinforced concrete structures and laboratory sized samples falls normaly between the conventional strength theory and predictions based on LEFM. Non-linear fracture mechanics is introduced which gives a smooth transition between the strength criterion and LEFM as shown in Fig. 55. Bažant further argues that existing code rules should be modified, and should be based on non-linear fracture mechanics in order to allow the translation of laboratory results to real structural sizes. Bažant proposed a size effect law as follows:

$$\sigma_N = Bf_t'(a_0\xi^{-1} + 1 + a_1\xi + a_2\xi^2 + a_3\xi^3 + \ldots)^{1/2r} \tag{4.1}$$

where $\xi = (d_a/d)^r$, d_a is the maximum aggregate size, and $B, f_t', r, a_0, a_1, \ldots$ are constants [52]. A simplified version of equation (4.1) was also proposed:

$$\sigma_N = Bf_t'[1 + (d/\lambda_0 d_a)^r]^{-1/2r} \tag{4.2}$$

This latter expression is probably sufficient for most structural applications. The size effect is caused by crack front blunting according to Bažant, which seems only a different terminology for the non-linear processes that take place around a crack in concrete as shown before in chapter 2. The size effect law suffers from two important

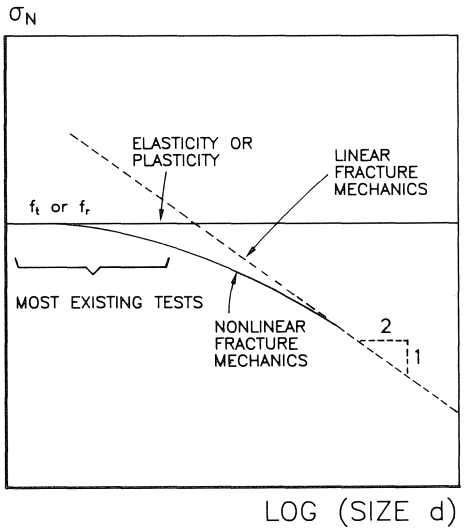

Fig. 55. Effect of structure size on strength, after [52].

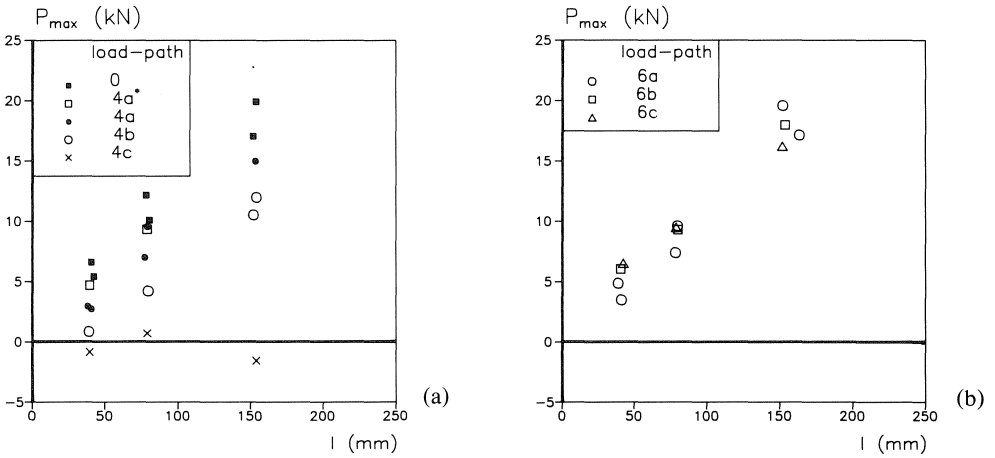

Fig. 56. Variation of strength for specimens of different size: (a) load-path 0 (uniaxial tension) and load-path 4 (confined tension), and (b) load-path 6 (proportional loading).

restrictions. First of all it can be applied only on geometrically similar specimens. The structure is scaled proportionally in two dimensions, whereas the third dimension (usually the thickness of the structure) must remain constant. The second restriction on the size effect law is that the load has to increase monotonically.
Using the biaxial test set-up, a number of experiments have been carried out in such a manner that verification of the size effect law is possible. Three different specimen sizes were tested, viz. double edge notched plates of size 50 × 50, 100 × 100 and 200 × 200 mm. The specimen thickness was always 50 mm. The notch to specimen size ratio was kept constant, viz. $a/d = 0.125$. As explained in chapter 3, the 200 mm square plate is the maximum specimen size that the biaxial machine can contain. For the two other sizes special loading platens were manufactured as explained in chapter 3 too. The two load-paths that could be compared with the size effect law were the uniaxial tension tests (load-path 0) and the proportional biaxial experiments (load-path 6). All other size tests (load-path 4 and 5) did not fulfil the requirement of monotonic loading.

4.6.1 Size effect on strength

In Fig. 56, the peak values measured in the load-path 4 and 6 experiments are plotted for each specimen size. On the horizontal axis the distance between the notches is plotted, on the vertical axis the maximum tensile load P_{max}. In Fig. 56a the results for the load-paths 0 and 4a-c are shown, in Fig. 56b the results for the load-path 6a-c experiments. At first glance, an almost linear increasing peak-load is measured with increasing size. Note that the strength decreases for the load-path 4 experiments when compared to the load-path 0 tests. This is caused by the presence of the lateral shear load at various levels. This point will be elaborated further in the next section. The results for load-path 6 do not show any effect of the ratio δ/δ_s on tensile strength. Note that this ratio δ/δ_s varied and was equal to 1.0, 2.0 and 3.0 for load-path 6a, 6b and 6c respectively. The load-path 5 results are not shown here, but these were completely identical to those of load-path 4 (see [5]).
If the results of Fig. 56 are translated to stress-size plots, hardly any effect of size on strength is found. The data points are almost on a straight horizontal line. The load-path 0 and 6a-c results have been modified in order to allow for a comparison with Bažant's size effect law. The size effect law (equation 4.2) can be translated to a linear plot following

$$Y = AX + C \tag{4.3}$$

where $Y = (f_t'/\sigma_N)^2$, $X = d/d_a$, $C = 1/B^2$ and $A = C/\lambda_0$. The slope A and the Y-intercept C can easily be determined from a regression analysis. This gives an estimate of the two unknown parameters in the size effect law, viz. B and λ_0. At the same time, the errors introduced can be estimated. The coefficient of variation of the deviations from the regression line is $\omega_{y/x} = S_{y/x}/\bar{Y}$, where $S_{y/x}$ is the modified standard error estimate and is equal to $\{\Sigma[y_i - y_{est}]^2/(N-2)\}^{1/2}$. $\bar{Y}$ is the mean value of the experimental Y data. The correlation coefficient r is given by $\{1 - S_{y/x}^2/S_y^2\}^{1/2}$, where S_y is the standard deviation.

The papers published by Bažant do not give information on which values for $\omega_{y/x}$ are r are acceptable.

The results for load-path 0 and 6a are shown in Figs. 57 and 58 respectively. The coefficients A and C as well as the values for $\omega_{y/x}$ and r are plotted in the various figures. In a diagram with linear scales, the size effect law appears as a straight line. For the load-path 0, the results are found to be in agreement with the results of Bažant. In the log-log plot of Fig. 57b, the expected tendency is retrieved. Thus, the size effect law seems to be confirmed by the present load-path 0 results.

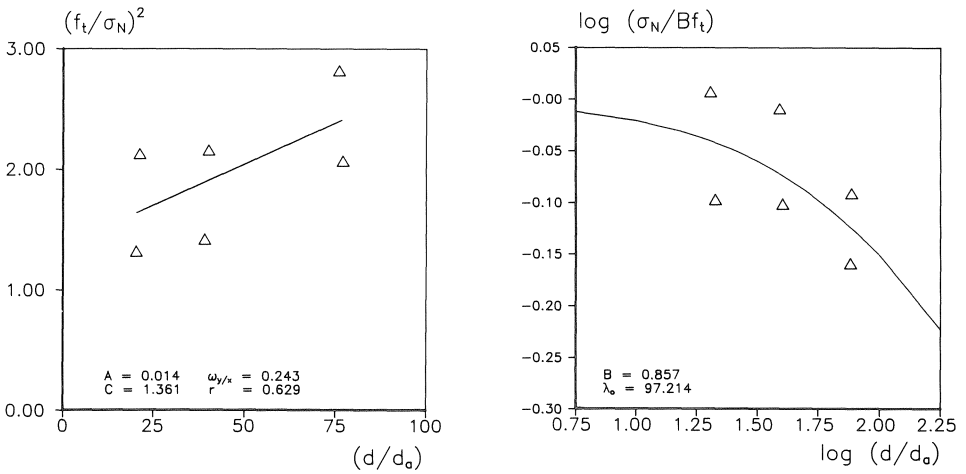

Fig. 57. Fit of size effect law to uniaxial tensile data (load-path 0).

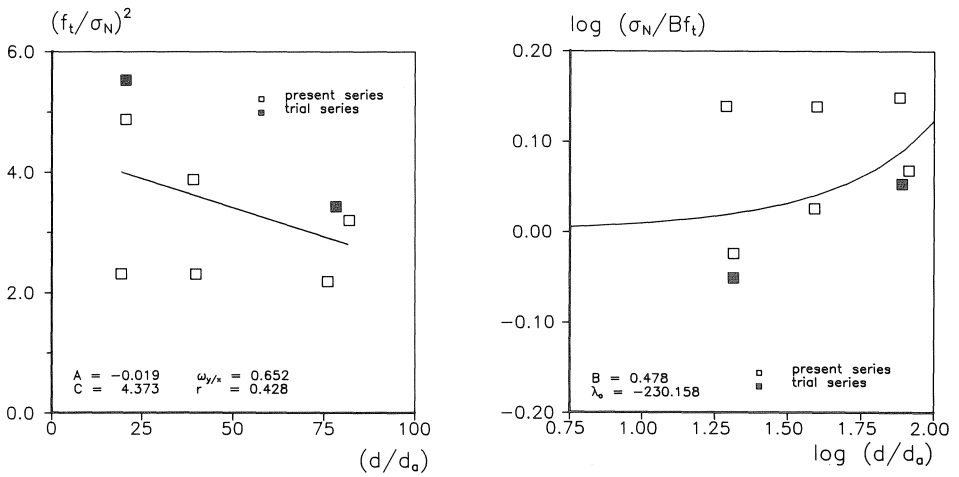

Fig. 58. Fit of size effect law to biaxial results (load-path 6a, $\delta/\delta_s = 1.0$).

Surprisingly, the load-path 6a results gave an opposite trend. The regression yielded a straight line with negative slope (Fig. 58a), and in a log-log plot an upward curved relationship was found. The exact reason is not known. Part may be explained from the fact that in the load-path 6a experiments a number of specimens were of slighlty higher age than the others. More important however seems the fact that the failure modes changes for the load-path 6 experiments for the three different sizes (see section 4.6.3). It is felt that a rigorous micromechanical analysis is required in order to better understand the behaviour of the concrete under these complex load-paths. For example the approaches from [20] and [21] could be adopted. These models gave interesting results on the fracture mechanism of concrete under uniaxial tensile or uniaxial compressive loading (Fig. 8). The same models can likely be used for explaining the size effect.

4.6.2 Load-path 4 results

The load-path 4 results can not be compared with the size effect law because the second condition that loading must be applied monotonically was not fulfilled. The experiments were the first that were carried out without precracking the specimen. This should give some information on mode II (shear) fracture of concrete. Some of the load-path 4 results were discussed in section 4.5.2. Here the effect of varying the specimen size is presented. The load-displacement diagrams for the load-path 4 experiments with three different sizes are shown in Fig. 59, the corresponding crack patterns for three load-path 4b experiments are shown in Fig. 60.

As can be seen from Fig. 59a, the axial peak load P_{max} decreases with decreasing specimen size (see also Fig. 56a) in the presence of a lateral shear load of -5 kN (load-path 4a). Comparison with the uniaxial tensile results of Fig. 28 shows that the presence of the -5 kN lateral confinement has indeed a significant effect. The post-peak P-δ behaviour for load-path 4a did not differ significantly from the uniaxial diagram. The shape of the curve remains essentially the same, yet the impression is that the small specimens respond more ductile, but this can be a visual effect only. When the lateral confinement is increased, the peak values in the P-δ diagrams are even further reduced as shown in Fig. 59b. As soon as the lateral shear load is increased to the peak value ($P_{s,max}$), controlled failure through axial loading can be obtained only when compression is applied, see Fig. 59c. Similar results were presented before in section 4.5.2. Note that the 50 mm specimens were already close to "shear-failure" in load-path 4b (Fig. 59b). For this particular 50 mm experiment also small compressive loads were needed in order to stabilize the fracturing.

It should be mentioned that the experiments on the 50 mm specimens were extremely sensitive to deviations from the exact shape and size. Eccentricities due to glueing or small geometrical deviations caused severe off-sets (see section 4.4.2, page 52) which in several cases led to glue fractures between the specimen and the loading platen. The experiments where this happened are not included in the present report.

The fracture modes for the load-path 4 experiments on specimens with different sizes are surprisingly self-similar [53]. This is shown in Fig. 60 for three load-path 4b experi-

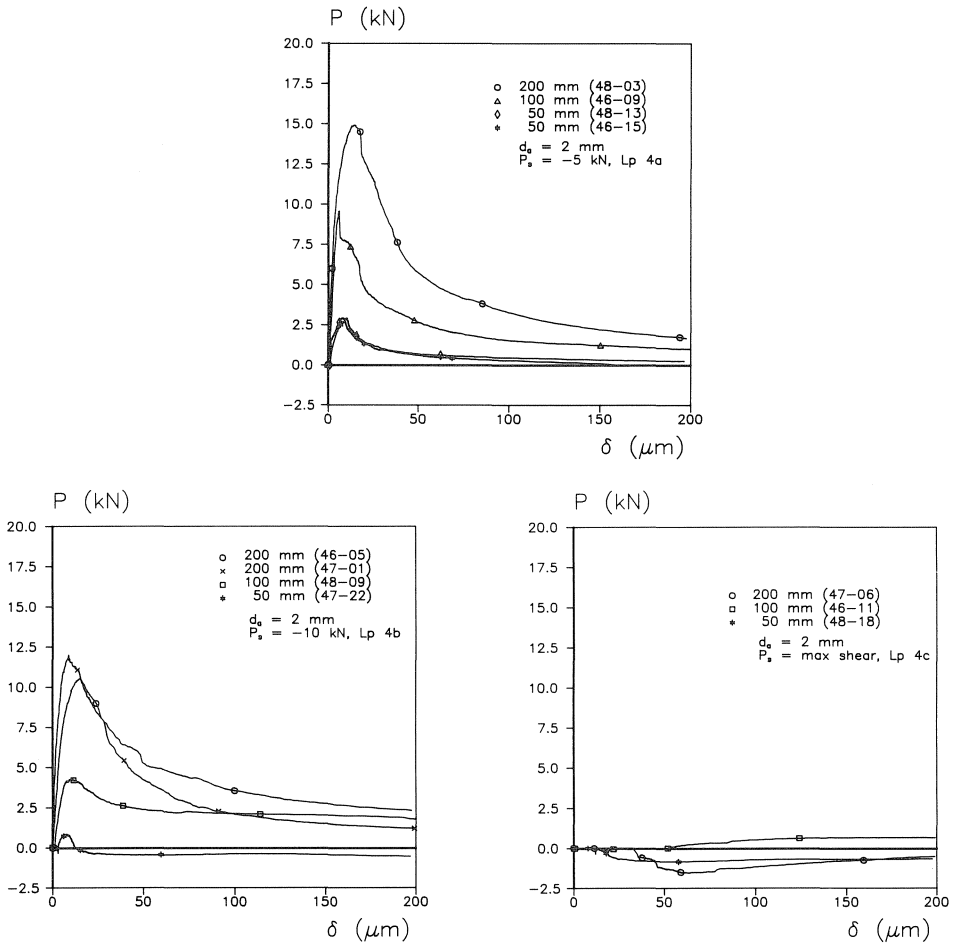

Fig. 59. *P-δ* response for load-path 4a, 4b and 4c for different specimen sizes.

ments. Note that the 50 mm specimen is identified as load-path 4b*. In this case not the −10 kN lateral confinement was reached, but was maintained at −9 kN in order to avoid premature failure of the specimen. In all cases the previously reported set of curved overlapping cracks developed in the specimens. Fig. 60 suggests that the fracture patterns scale with the scaling of the specimen. As mentioned before, the size of the intact ligament between the overlapping cracks increased with increasing lateral shear load (see Fig. 54).

Almost identical results were obtained for the load-path 5 experiments. In these tests the lateral shear confinement was changed to a constant lateral shear displacement. Consequently, the lateral shear load varied somewhat during the application of the axial loading. As shown in [5], this has no effect on the observed behaviour. The *P-δ* response and the failure modes were similar to those presented in Figs. 59 and 60.

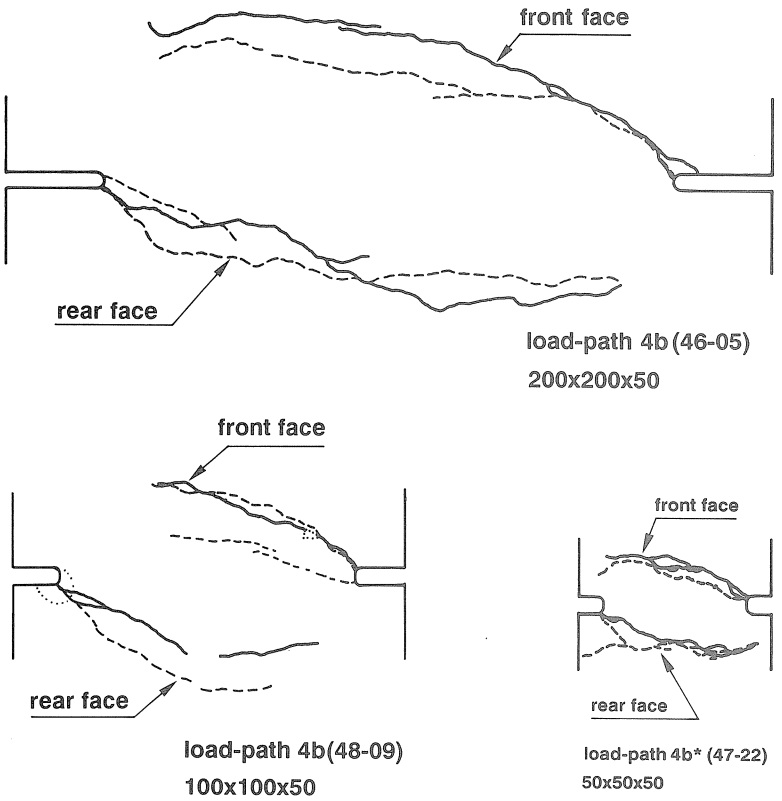

Fig. 60. Crack patterns traced on three load-path 4b experiments on specimens of different sizes.

4.6.3 Load-path 6 results

As mentioned before several specimens were loaded following a proportional path. In this case δ/δ_s was kept constant at 1.0, 2.0 and 3.0 for the load-path 6a, 6b and 6c experiments respectively. Due to partial elastic unloading in the measuring length during softening, the actual ratios δ/δ_s deviated somewhat from the planned values. In addition, rotations of the loading frames may have caused some deviations. These deviations were relatively small. For example for load-path 6b with $\delta/\delta_s = 2$, the angle α in the δ-δ_s plane should be constant and equal to 63.4°. In reality the value of α varied between 65.4 and 68.7°. Similar for load-path 6c, α should be equal to 71.6°, but varied between 72.9 and 78.7°. For load path 6a the values were 45° and only minor variations were observed.

Results for load-path 6a with $\delta/\delta_s = 1.0$ are shown in Fig. 61. In Fig. 61a, the normalised P/P_{max}-δ plots are shown, in Fig. 61b the corresponding P_s-δ_s curves. These latter diagrams could not be normalised because the peak shear load was not reached in all experiments (note: some of the 200 mm and 100 mm experiments were stopped because

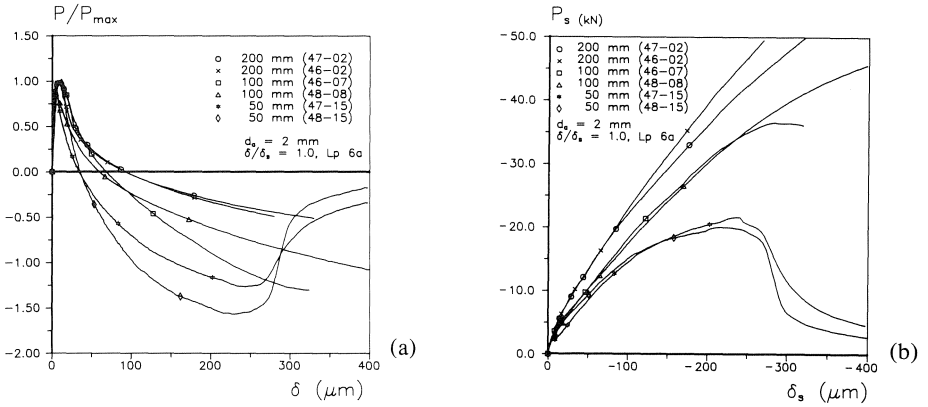

Fig. 61. P/P_{max}-δ plots (a) and P_s-δ_s diagrams (b) for the load-path 6a experiments ($\delta/\delta_s = 1.0$) on specimens of three different sizes.

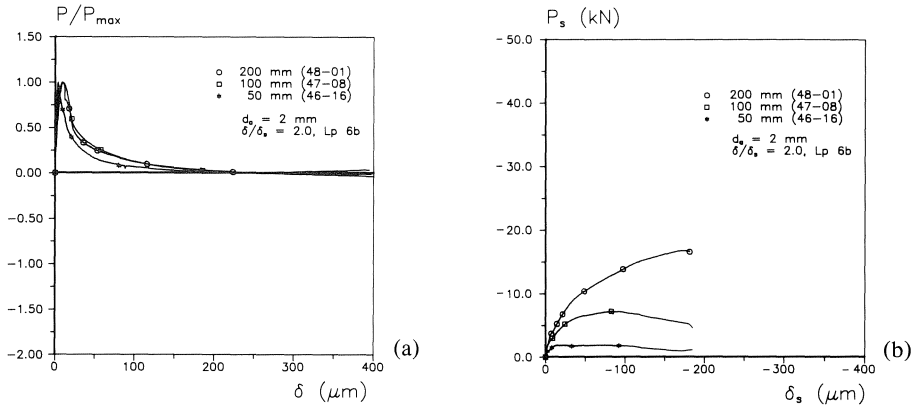

Fig. 62. P/P_{max}-δ plots (a) and P_s-δ_s diagrams (b) for the load-path 6b experiments ($\delta/\delta_s = 2.0$) on specimens of three different sizes.

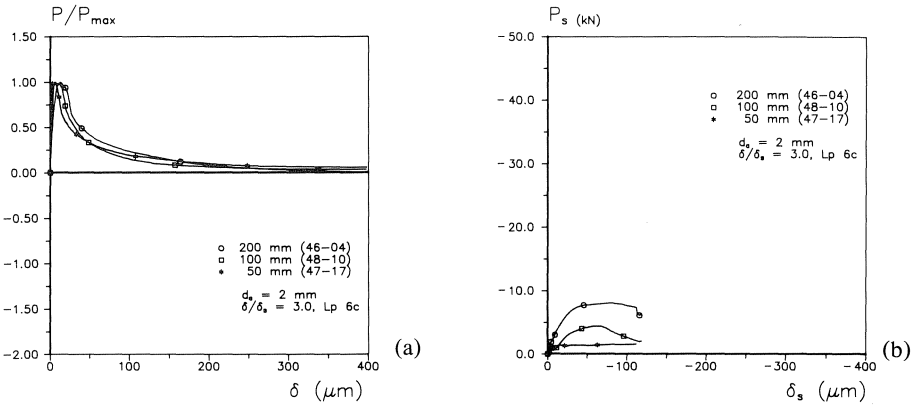

Fig. 63. P/P_{max}-δ plots (a) and P_s-δ_s diagrams (b) for the load-path 6c experiments ($\delta/\delta_s = 3.0$) on specimens of three different sizes.

the maximum capacity of the machine was reached). After a tensile peak was reached, the axial load changed from tension to compression at larger crack openings. Each test was carried out in duplicate and the results were relatively close together. In the 50 mm specimens a compressive peak was reached as well. A compressive peak would probably also have been found for the two other sizes, if these tests were not stopped because the maximum shear deformation of 400 μm was reached. Although the two 200 mm specimens gave an almost identical P-δ response, deviations were found in the crack patterns as shown in Fig. 64a and b. In the experiment 4702 (Fig. 64a) the overlapping crack mode was observed as reported before for the load-path 4 experiments. Note that the crack branches are more straight now. In the other specimen, 4602 (Fig. 64b), the loading was completely identical but now three in stead of two cracks developed. The order of crack growth was A, B and C. The effect may be caused by an eccentricity in the specimen. The same crack patterns developed at the front and back side of the specimen (see the solid and dashed crack patterns respectively).

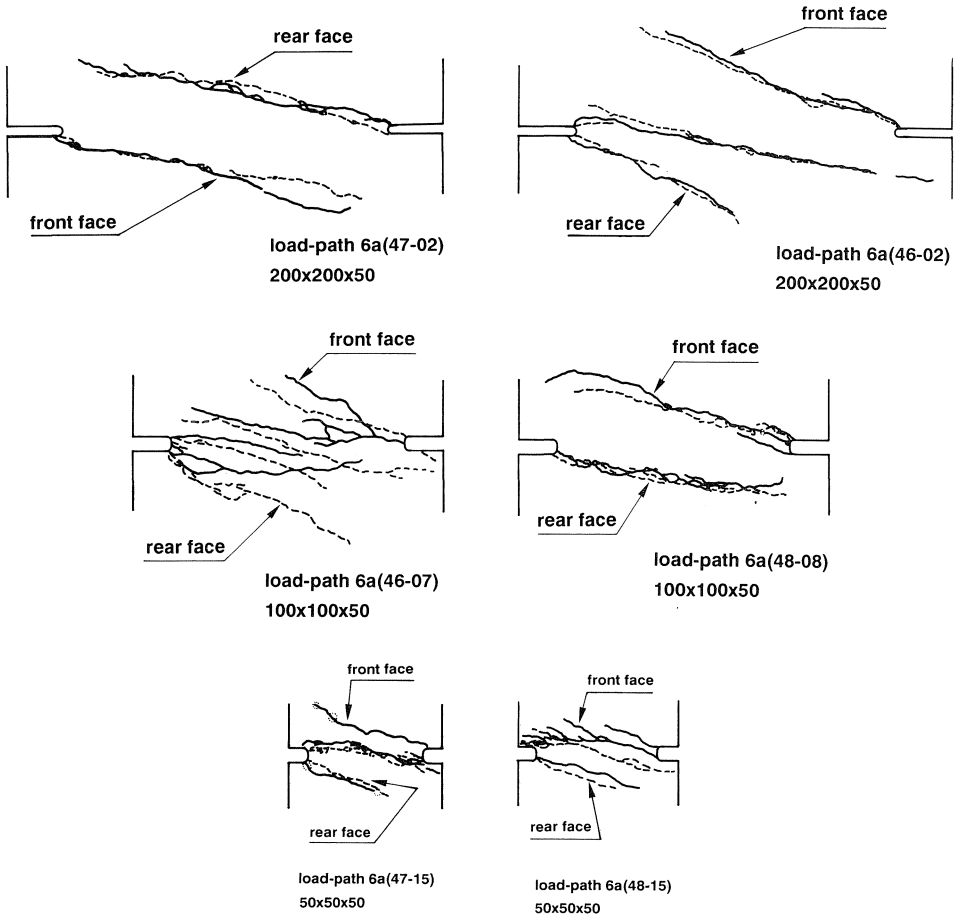

Fig. 64. Crack patterns for duplicate load-path 6a experiments ($\delta/\delta_s = 1.0$) on 200 mm specimens (a, b), 100 mm specimens (c, d), and 50 mm specimens (e, f).

The crack patterns for the 50 and 100 mm experiments are given in Fig. 64c through 64f. For both sizes it was found that two identical loadings yielded different fracture patterns. In two of these specimens a more distributed crack pattern was found, resembling almost the macroscopic shear crack as defined by Bažant and Pfeiffer [25]. Perhaps these experiments are close to the transition between shear fracture and tensile fracture. They give some hope as to the possible existence of shear fracture. The use of the micromechanics models [20, 21] is considered a necessity to come to a better understanding of the observed phenomena.

In the load-path 6b and 6c experiments the effect of shear was less dominant. This can be seen from the respective P/P_{max} and P_s-δ_s curves of Figs 62 and 63. In Load-path 6b, the axial stress changed from tension to compression, but obviously the effect was much smaller here. The maximum shear load decreased considerably.

The load-path 6 experiments can be compared with recently published test results by Hassanzadeh at the Lund Institute of Technology [54]. His experiments were aimed at determining the mixed mode properties of the process-zone, in fact similar to the present effort. In Lund, very small specimens (size 70 × 70 × 60 mm, with a circumferential groove leaving an effective area of 40 × 40 mm) are subjected to a combination of tension and shear. Next to a number of parabolic load-paths, several proportional load-paths were investigated with $\alpha = 30$, 60 and 75°. These values are close to the present load-path 6 experiments where $\alpha = 45$, 63.4 and 71.6°. A comparison between the results from Lund and the 50 mm load-path 6 experiments is shown in Fig. 65. Note that the results have been translated in stress-crack opening diagrams, where the

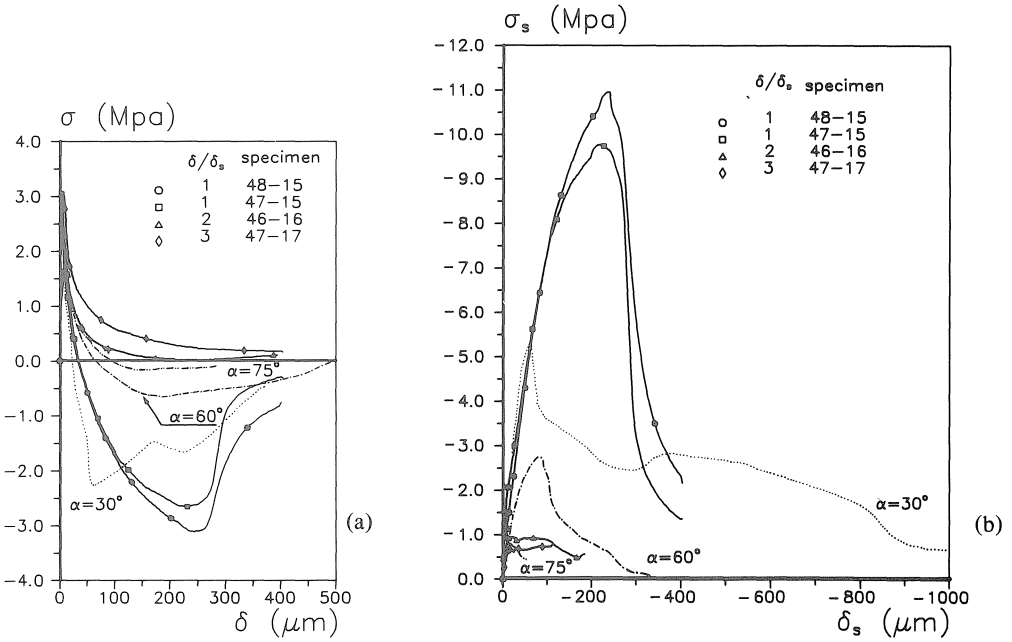

Fig. 65. Comparison of the proportional load-path tests (6a, 6b and 6c) on 50 mm specimens with results from [54]: (a) σ-δ diagrams and (b) σ_s-δ_s diagrams.

(nominal) stress is defined as the load divided by the net cross-section of the specimen. Although the values of α differ, the comparison of the results in Fig. 65 shows that similar trends are found for the two different approaches. The stress changes from tension to compression in the σ-δ diagrams: the effect is most pronounced for small values of α. Deviations may occur because the experimental set-ups are different. The application of both the axial tensile and lateral shear loading is completely servo-controlled in Delft, but must be applied manually in the shear direction in Lund. However, the Lund apparatus is supplied with an axial servo-control. Most unfortunately the circumferential notch in the tests in Lund prevented an accurate tracing of the crack patterns. Therefore the uncertainty about the dominant failure mode in load-path 6 remains, but may likely be resolved by applying the recently developed micromechanical models as mentioned before.

4.7 *Path-dependency*

The experiments in Lund showed that mixed mode I and II fracture is path dependent. This was found from a comparison between linear and parabolic crack opening paths (δ/δ_s) that were tested by Hassanzadeh [54]. The present load-path tests were very extensive and can be used to confirm the path dependency observed in Lund. To this end the load-path 3b, 4, 5 and 6 experiments can be compared. All specimens that were included in the comparison are of size 200 × 200 mm, and the material is a 2 mm mortar. In Fig. 66 the crack opening paths from four experiments are shown: load-path 3b, 4b, 5b and 6b. As can be seen, the various δ-δ_s diagrams intersect in one or more points. If the biaxial loading is path *independent,* then the same point at the δ-δ_s curve should correspond to the same point on the P-P_s curve. Or stated differently, an intersection

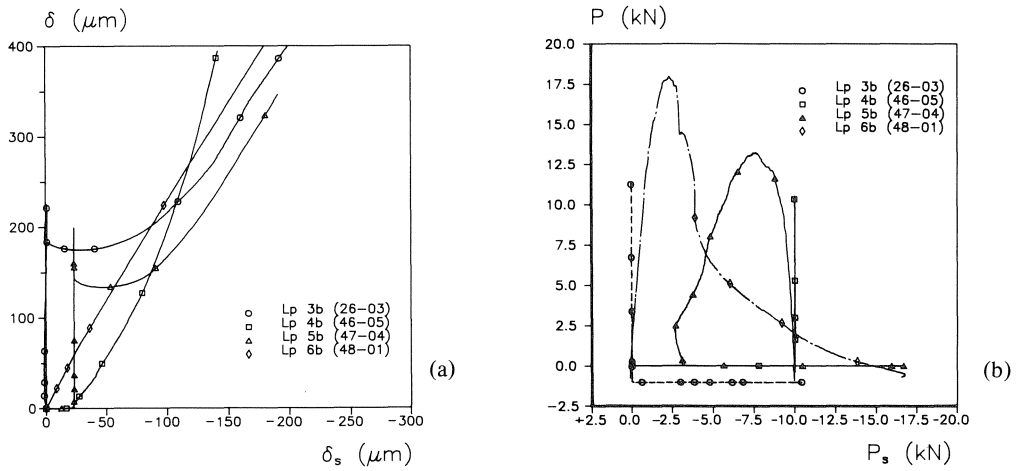

Fig. 66. Comparison of crack opening paths δ-δ_s for load-path 3b, 4b, 5b and 6b experiments (a), and the corresponding P-P_s diagrams (b).

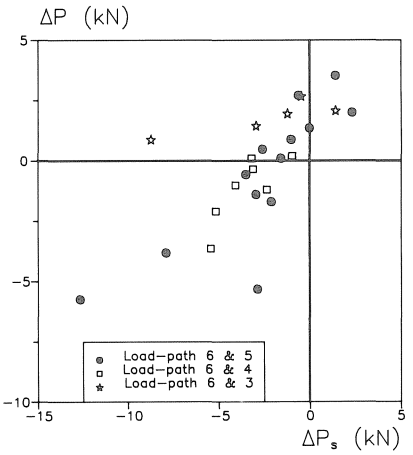

Fig. 67. ΔP-ΔP_s plot: deviations in intersection points in the P-P_s plane.

point between the δ-δ_s curves of two different load-path tests should correspond to an intersection of the respective P-P_s curves. For all the load-path 3b, 4, 5 and 6, the intersections were retrieved from the data-sets, and the deviations in axial and lateral load were calculated. These loading differences were then labeled ΔP and ΔP_s, and plotted in Fig. 67. The behaviour of the specimens would be path independent if $\Delta P = \Delta P_s = 0$, which is clearly not the case in the present experiments. The results confirm the findings of Hassanzadeh. Note that the maximum load P_{max} in a 200 mm experiment is approximately 20 kN, whereas the maximum shear load $P_{s,max}$ varies between 5 and 50 kN. This may indicate that the intersection points are significantly shifted in the P-P_s plane.

The path dependency poses a poblem in the analysis of the results in terms of nominal stress and crack opening. The path dependency implies that the theory must contain a memory, and that the damage sustained to the specimen must be remembered at all stages.

4.8 *Summary of failure modes*

In Table 5, the fracture modes in the various experiments are summarized. Some general remarks can be made. First of all, the shear tests at small crack openings show that secondary cracking may occur under specific boundary conditions. This is an aspect which is completely overlooked in conventional aggregate interlock theories, e.g. [31]. In these theories sliding along crack faces has been modelled for relatively large crack openings. It is common practice to extend the range of application of the models to smaller crack widths, but the present results show that this is not unrestrictedly allowed. If a good agreement is observed between the aggregate interlock theories and the results at small crack openings this would probably be purely accidental. The

experiments that were used to tune the aggregate interlock models were rather rough, and the specimens were not loaded as carefully as is now possible in the newly developed biaxial apparatus. The growth of diagonal secondary cracks was observed mainly under unconfined- and confined-tensile-shear and confined-compressive-shear (viz. load-paths 1a, 1b, 2 and 3b). The unconfined-tensile-shear-tests and the unconfined-compressive-shear-tests showed sliding modes of failure, accompanied by uplift in the crack. The restriction for the unconfined-tensile-shear-tests in this respect is that the crack opening δ_0 should be larger than 250 μm, at least for the 2 mm mortar tested. All load-path 4, 5 and 6 experiments failed through the growth of a set of overlapping cracks. As shown before in paragraph 4.6, the crack shapes were similar for the three specimen sizes investigated. In the case of load-path 4 and 5, the crack branches were curved. For load-path 6, at least for the larger sizes, straight overlapping cracks were found.

Mode II fracture from virgin specimens has not been found. An exception to this rule is that some of the smaller sized plain concrete specimens showed a more distributed

Table 5. Overview of failure modes for plain concrete tests

load-path	pre-cracked	shear	boundary condition during shear	failure mode
0	yes	-	-	tensile cracking
1a	yes	compr.	δ_0=constant	could not be failed in shear
1b	yes	tensile	δ_0=constant	secondary diagonal cracks
2	yes	tensile	$P=0$=constant	- secondary diagnonal cracks ($\delta_0<250$ μm) - sliding ($\delta_0>250$ μm)
3a	yes	compr.	$P=0$=constant	sliding
3b	yes	compr.	$P=-1$ kN=constant	- splitting cracks, lytag - sliding, 2 mm mortar - sliding, 16 mm concrete
4a	no	compr.	$P_s=-5$ kN=constant	overlapping cracks
4b	no	compr.	$P_s=-10$ kN=constant	overlapping cracks
4c	no	compr.	$P_s=P_{s,max}$=constant	overlapping cracks
5a	no	compr.	δ_s=constant*	overlapping cracks
5b	no	compr.	δ_s=constant*	overlapping cracks
5c	no	compr.	δ_s=constant*	overlapping cracks
6a	no	compr.	$\delta/\delta_s=1$=constant	overlapping cracks**
6b	no	compr.	$\delta/\delta_s=2$=constant	overlapping cracks**
6c	no	compr.	$\delta/\delta_s=3$=constant	overlapping cracks**

* In the load-path 5 experiments, a specimen was loaded in displacement control up to a prescribed lateral shear confinement of −5 kN, −10 kN and $P_{s,max}$ respectively. After this, the specimen was failed in axial tension while maintaining δ_s=constant.

** Some of the smaller sized load-path 6 experiments failed through the growth of a system of distributed inclined cracks. This failure mode was however not consistent throughout the complete test series.

crack pattern. These failure modes were however not systematic. Some other exceptions are the SIFCON tests, which will be presented in chapter 5. This observation implies that the mode II fracture tests of Bažant and Pfeiffer [25] should be treated with the utmost care. It seems that a shear crack can only develop when the neighbouring parts of the specimen are very well confined.

The present experiments may be compared with the beam tests of Bažant and Pfeiffer, but also with those of Swartz and Taha [27]. The fracture modes of the unconfined beam tests (that is without prestressing normal to the potential crack plane) of Swartz and Taha was that two overlapping curved cracks developed between the two notches in the beams, see Fig. 10. Although the boundary conditions in the plane normal to the potential shear crack plane differed in the present experiments it is believed that the behaviour of the DEN specimens (especially the load-path 4c and 5c experiments that were first loaded in shear to the maximum shear load $P_{s,max}$) may be compared with the beam tests with narrow shear zone. The load-path 4 and 6 experiments show that the shape of the crack branches may differ depending on the exact boundary condition during shearing, but the essential point is that always a set of overlapping cracks develops from the two notches. Future computations are required to investigate the significance of the boundary conditions in these experiments.

5 Shear fracture in SIFCON

SIFCON is a relatively new construction material, and consequently only limited information is available about the mechanical properties. Recent research has focussed mainly on the properties of SIFCON under static tensile and compressive loading (see [55, 56]). Information on the shear response of the material is almost completely lacking. Therefore, it was decided to use the biaxial test set-up for a number of tension/shear experiments on SIFCON as well. In the following paragraphs the main results are discussed. First however the variables in the investigation are summarized in section 5.1.

5.1 *Variables in the biaxial SIFCON experiments*

The variables selected in the present investigation are two material parameters, and the tensile crack opening before shear was applied. Because the material is highly anisotropic, especially in the way it has been manufactured in the Stevin Laboratory, the loading direction with regard to the main fibre direction was selected as the most important variable. In Fig. 68 the fibre direction is defined through an angle α with the centre line through the two notches. It is emphasized here that the investigation has an exploratory character, and in order to limit the number of experiments only fibre inclinations between 0° and 90° have been studied. The selected angles are 0, 22.5, 45, 67.5 and 90 degrees.

The second variable in the investigation is the fibre type. Specimens were prepared with ZL 30/0.5 and OL 25/0.5 fibres respectively. The different bond properties of the two fibre types were expected to influence the fracture behaviour of the SIFCON.

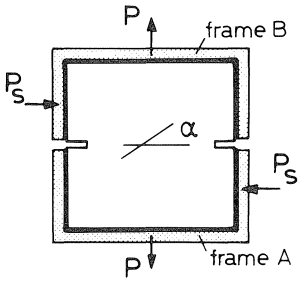

Fig. 68. Orientation of fibres with respect to tensile and shear loading directions.

For comparative reasons, a number of displacement controlled uniaxial tests were carried out on the plain slurry. In these latter tests, the specimens were fixed in the biaxial machine in a similar way as the SIFCON specimens (i.e. with four sides glued, plus the additional steel platens at the free sides, see Fig. 25). Three slurry tests were carried out on specimens cured in the same manner as the SIFCON specimens as described in section 3.2. In addition, because many probles were cause by shrinkage cracking in these specimens, four additional tests on slurry specimens were carried out where the specimens remained in the water until two days before testing.
The third variable is the crack-opening before shearing. The specimens were loaded following load-path 3a (see section 4.1): shear in displacement control after the specimen was pre-loaded in tension to a prescribed axial crack opening. During shear the load normal to the crack plane was kept constant at zero. Specimens were pre-loaded to the following axial crack openings: $\delta = 10, 25, 50, 100, 200, 300$ or 400 μm. The respective loading rates for tension and shear were 1.69 and 1.57 μm/min. In the descending branch the loading rate was normally doubled two times. From a number of preliminary tests it was found that the specimens with fibre orientations of 67.5° and 90° could not be loaded up to crack openings larger than 50 μm because the maximum loading capacity in the biaxial test-rig was reached. Therefore, a number of tests was omitted from the original test scheme. Table 4 gives the overview of all tests carried out. The letter combinations ZL/OL indicate the planned experiments. Where specimen codes appear in the table, the tests have actually been performed. Note that a number of preliminary tests have been carried out and were published in [57]. These results will not be repeated here, but only used as a reference. Furthermore it should be mentioned that by loading specimens according to load-path 3, implicitly the tensile stress-deformation response of the material is measured. Of course these results will be discussed here as well. Because the original test scheme was too time consuming, a number of tests at very small crack openings had to be omitted as well.
In the following paragraphs, the results will be presented. First the effect of the different variables on the load-displacement response in tension and shear will be discussed. Following this exposure the fracture patterns will be shown. In a number of tests, real time crack growth was studied with a motorized high resolution long distance microscope (QUESTAR QM 100, with a resolution up to 1.1 μm).These results will be discussed in section 5.5.

Table 6. Overview of the SIFCON test

α [degree]	0	22.5	45	67.5	90
δ_0 [μm]					
10	ZL/OL	ZL/OL	ZL/OL	ZL/OL 1802/1107*	ZL/OL
25	ZL/OL	ZL/OL	ZL/OL 1902/1106	ZL/OL 1607/1007	ZL/OL
50	ZL/OL 1604/1202	ZL/OL 1801/1005	ZL/OL 1603/1006	ZL/OL 1606/1003	ZL/OL 1608/1108
100	ZL/OL 1702/1104	ZL/OL 1602/1103	ZL/OL 1605/1102 /1205	ZL/OL -/1206	?
200	ZL/OL 1903/1004	ZL/OL 1601/1001	ZL/OL 1901/1002 /1204	?	?
300	ZL/OL 1904/1201	ZL/OL 1701/1203	ZL/OL 1703/1105	?	?
400	ZL/OL	ZL/OL	ZL/OL 1803/1101	?	?

* Specimen code: the first two numbers denote the batch number (see Table 3), the consecutive two numbers show the sequential specimen number for the specific batch.

5.2 *Strength and ductility*

For $\alpha = 0°$, the effect of crack-opening on the shear behaviour of SIFCON is shown in Figs. 69 and 70. In each figure not only the shear-load - shear-displacement diagram ($P_s - \delta_s$) is shown, but also the preceeding load-history ($P - \delta$ plots). In Fig. 75 the results for ZL fibres are shown, in Fig. 70 the OL results.

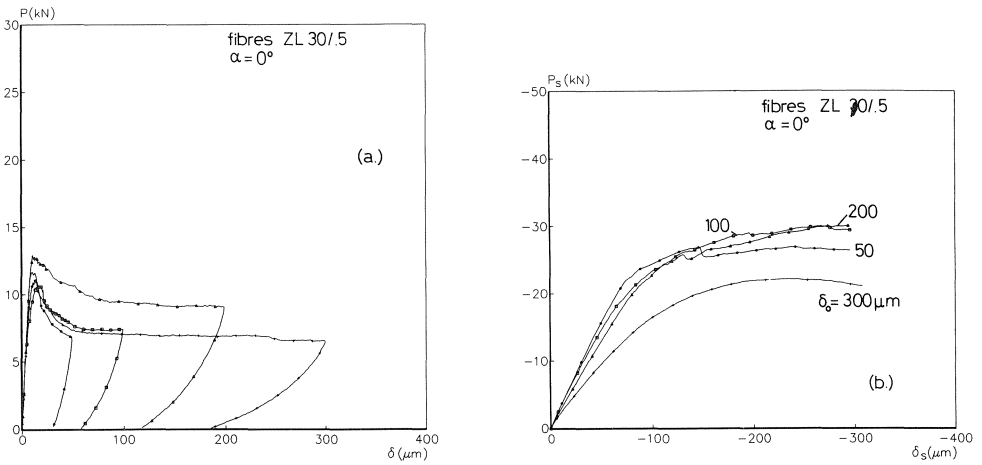

Fig. 69. P-δ plots for experiments with ZL fibres; $\alpha = 0°$ (a) and (b) P_s-δ_s plots for the tests from Fig. (a).

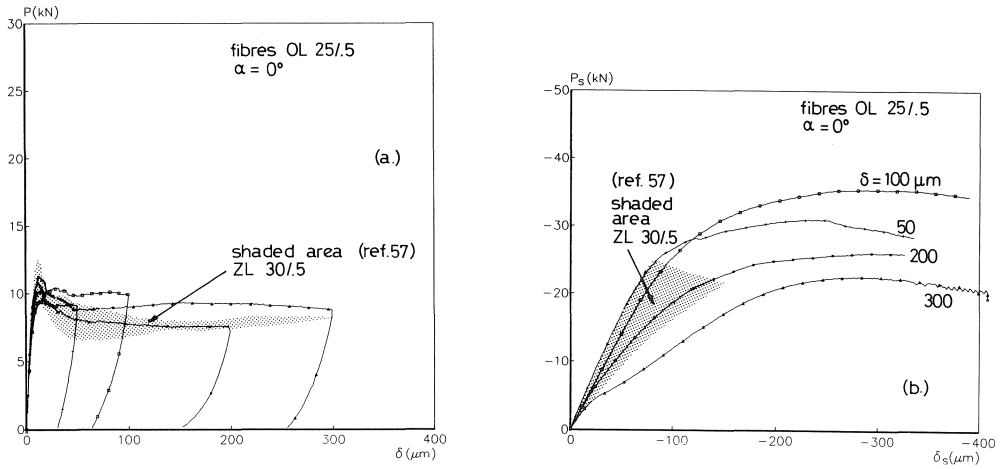

Fig. 70. *P-δ* plots for experiments with OL fibres; $\alpha = 0°$ (a) and (b) P_s-δ_s plots for the tests from Fig. (a). The shaded area is the range of results obtained from preliminary ZL tests (see [57]).

The *P-δ* diagrams (Fig. 69a and 70a) clearly show that the tensile strength of the SIFCON is rather disappointing at fibre orientations of 0°: the average tensile strength $\sigma_t = 2.86$ MPa and 3.09 MPa for the OL and ZL fibre specimens respectively. The strength increase is very moderate in comparison with the strength of the plain slurry (Fig. 71). The average tensile strength of the slurry specimens cured following the normal procedure was $\sigma_t = 3.23$ MPa (average of three tests); whereas allowing the specimens to dry only two days before testing leads to a much lower strength: $\sigma_t = 2.2$ MPa (average of four tests). Obviously there must be a moisture gradient in these latter specimens, causing tensile eigenstresses at the surface of the specimens [58]. As shown before for normal concrete this will generally lead to a reduced strength of the specimen [45, 59], even as much as 30%. The above results for plain slurry should therefore be regarded with some care. In spite of the fact that care was taken to avoid shrinkage cracking in the specimens, the angular crack patterns indicated that still shrinkage cracks appeared, and affected the tensile response. In fact, the tail of the softening diagram of the slurry is rather high, which can be explained from the resistance of the large ligament between the two overlapping cracks that developed in the specimen (see the inset of Fig. 71).

The corresponding shear curves are shown in Figs. 69b and 70b for ZL and OL fibres respectively. The first observation is the decreasing shear stiffness with increasing axial crack opening. This result is straightforward, and was expected on the basis of experiments on plain concrete. The shear strength of the material is very low. If the maximum shear stress τ_s is calculated from the maximum values of P_s, very low values ranging between 6.01 (5.87) and 8.64 (8.01) MPa for the OL (ZL) fibres with crack openings between 50 and 300 μm are found. This means that the shear strength is approximately two to three times larger than the tensile strength of the SIFCON, but in comparison to

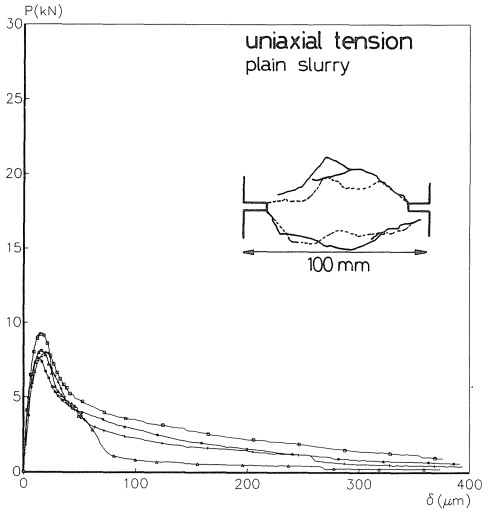

Fig. 71. *P-δ* plots for four tests on plain slurry. The specimens were allowed to dry two days before testing. An example of a crack pattern is shown in the inset.

the compressive strength of the material it is relatively low (see Table 3). The reason for this must again be sought in the anisotropy of the material as will be explained in section 5.4. The present results are too limited to draw a definite conclusion regarding the (expected) relation between shear strength and axial crack opening before shearing. The tendency is that τ_s decreases with increasing axial unloading displacement δ_0. This tendency is more pronounced for the OL tests than for the ZL tests.

5.3 *Effect of fibre type*

In Fig. 72 the *P-δ* plots for the two types of SIFCON and the plain slurry are compared. The post-peak behaviour of the SIFCON is very ductile when compared to the brittle behaviour of the slurry. The SIFCON results shown in Fig. 72 are for $\alpha = 0°$. The differences between the two types of SIFCON are minor. The *P-δ* curves of the tests on ZL fibre specimens showed a slight increase for larger crack openings in the preliminary test series (see Fig. 70a shaded area, after [57], indicating that the pull-out of the fibres is easier for the straight (and somewhat shorter) OL fibres. This should be expected. The more recent results (Fig. 69a) indicate that this increase in carrying capacity for large crack openings must be very small indeed.

The difference in shear response of the two SIFCON mixes is also not very large. As shown in Fig. 73, the only difference seems to be the slope of the ascending branch in the P_s-δ_s diagrams. The initial slope seems to increase for the ZL fibres. This point will be elaborated further in chapter 6. The results indicate that there is no effect of fibre type on maximum shear load. However, a larger test-series would be required to obtain a statistical basis for this statement.

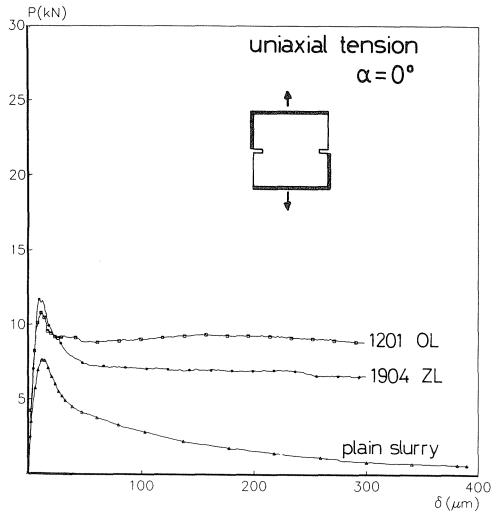

Fig. 72. Comparison of P-δ diagrams for SIFCON with OL and ZL fibres ($\alpha = 0°$), with plain slurry.

The shear stiffness has been analysed for all experiments. These results will be discussed in chapter 6.

5.4 *Effect of fibre orientation*

The most important variable in the SIFCON study was the orientation of the fibres with respect to the biaxial loading. In Fig. 74 five results are shown of experiments loaded to an average axial crack opening of 50 μm, and with varying inclination of the main fibre direction (viz. $\alpha = 0, 22.5, 45, 67.5$ and 90 degrees). The fibres were ZL 30/0.5. Both the

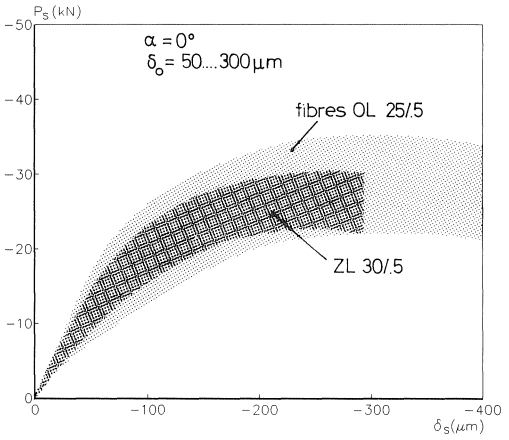

Fig. 73. Comparison of shear load-displacement (P_s-δ_s) response for ZL and OL specimens. The shaded areas show the range of results obtained for each fibre type.

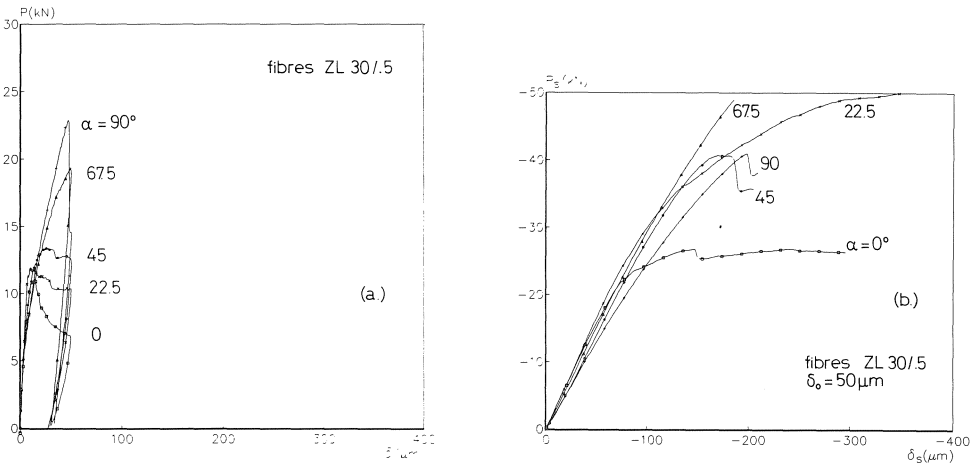

Fig. 74. Effect of fibre orientation on P-δ (a) and P_s-δ_s (b) response; ZL fibres; axial unloading deformation $\delta_0 = 50$ μm.

$P - \delta$ (Fig. 74a) and P_s-δ_s diagrams (Fig. 74b) are shown. In Fig. 75 similar results are presented for the OL 25/0.5 fibres.

The results are comparable, and indicate a similar trend. The P-δ diagrams show a sharp increase with increasing fibre orientation α. The OL test with $\alpha = 90°$ (Fig. 75a) was terminated because the maximum load in the vertical axis of the biaxial machine was reached. The increase of load P with increasing fibre angle α can easily be explained. At $\alpha = 0°$, not many fibres are alligned with the tensile loading direction, and in fact the strength of the slurry layers in between the fibres is tested. As shown in the previous paragraph, the tensile strength σ_t of the SIFCON mixes is equal to the strength of the

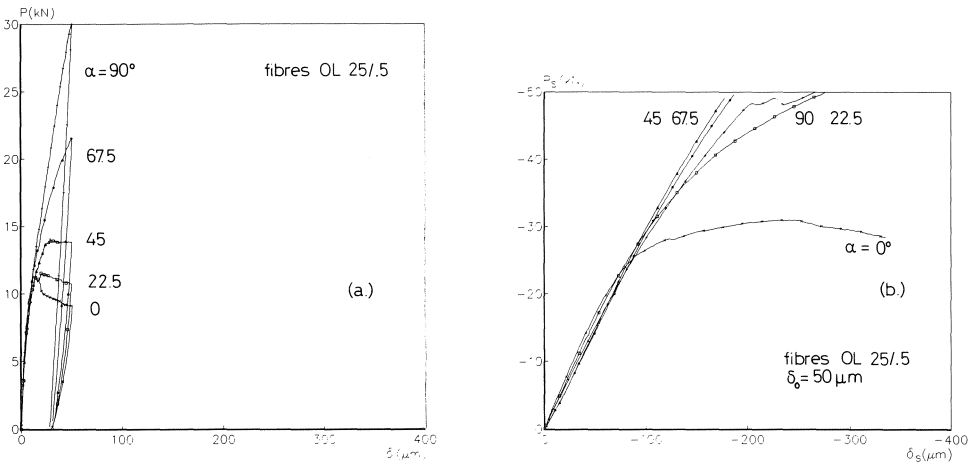

Fig. 75. Effect of fibre orientation on P-δ (a) and P_s-δ_s (b) response; OL fibres; axial unloading deformation $\delta_0 = 50$ μm.

plain slurry. When the fibre direction rotates, an increasingly larger number of fibres intersects the potential crack plane and the strength of the specimen increases considerably. The limit value for the strength is reached for $\alpha = 90°$, when the maximum amount of fibres is alligned with the tensile loading. The effect of fibre direction on shear capacity is significant. Figs. 74b and 75b show that a low shear strength is measured for specimens with $\alpha = 0°$. This is observed both for the ZL and OL fibre systems. At larger inclinations, it is found that the specimen can (generally) not be failed in shear anymore in the present test set-up. Either the maximum load was reached, or glue fractures would occur. For testing the SIFCON with (favourably) alligned fibres, a different test-method is required.

The effect of fibre orientation on tensile and shear behaviour of SIFCON can be deduced from the various tests on specimens pre-loaded to 100 μm axial crack opening as well, see Fig. 76 and 77 for the ZL and OL fibres respectively. The OL results in Fig. 77 show a similar tendency as the previous results for specimens loaded up to 50 μm (Fig. 75). Again a low shear capacity is measured for the specimen with $\alpha = 0°$, whereas the specimens with a more inclined fibre system (viz. 22.5 and 45°) could not be failed in shear. For the ZL fibre system, a somewhat different behaviour is observed, see Fig. 76a, b. In the three test results presented in this figure, first a specimen was pre-loaded to an average axial crack opening of 100 μm. Following this shear was applied, and surprisingly all three specimens could be failed in shear (thus irrespective of the fibre orientation). Close observation of the P-δ diagrams shows that there is quite some scatter in post-peak response. In fact it is believed that the exact number of fibres that intersects the fracture plane determines the post-peak resistance, and a slight increase of the number of fibres can have a significant effect on post-peak carrying capacity. The results indicate - and in view of the number of tests that have been carried out unfortunately no more than that - that the shear capacity of the SIFCON is strongly correlated with the number of fibres that intersect the potential fracture plane.

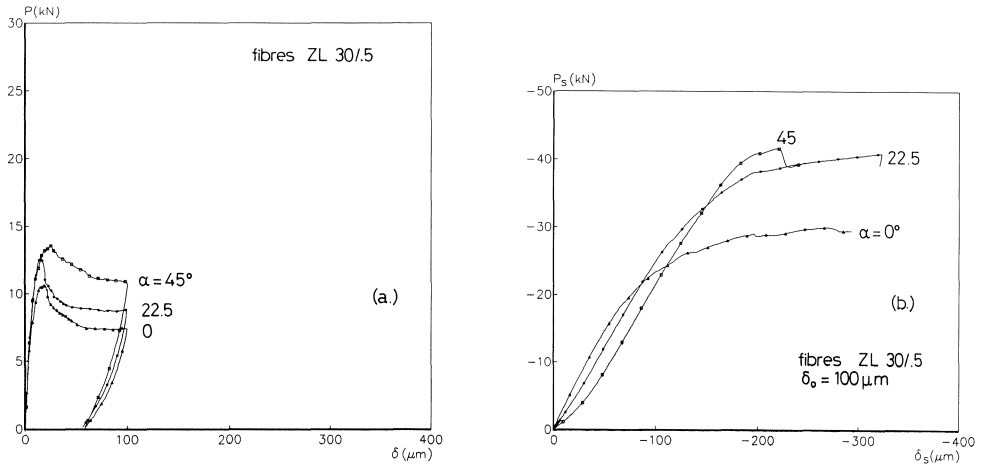

Fig. 76. Effect of fibre orientation on P-δ (a) and P_s-δ_s (b) response; ZL fibres; axial unloading deformation $\delta_0 = 100$ μm.

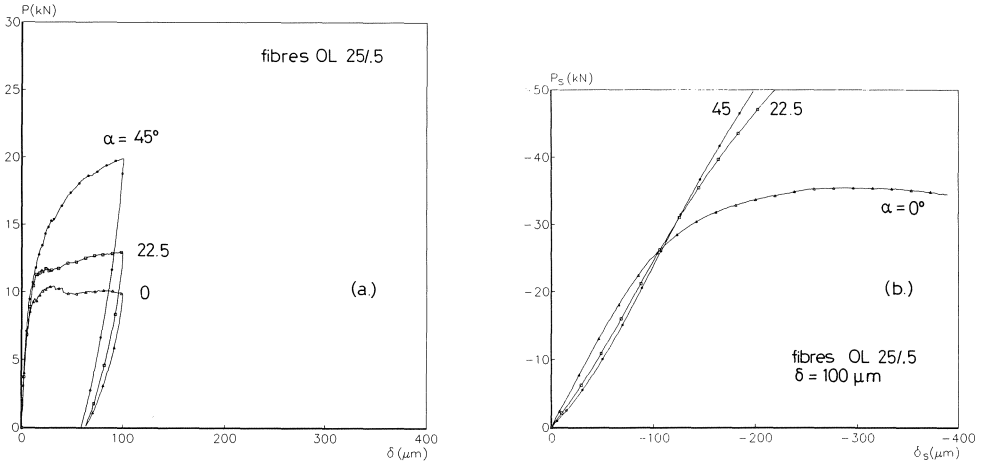

Fig. 77. Effect of fibre orientation on P-δ (a) and P_s-δ_s (b) response; OL fibres; axial unloading deformation $\delta_0 = 100$ μm.

It is interesting to see how the crack patterns developed in the specimens. Anticipating the microscopic observations presented in the following paragraph, global crack patterns traced from the surfaces of specimens after the tests was stopped are shown in Fig. 78. Three different results are shown: (a) a specimen with $\alpha = 0°$, pulled in displacement control up to 50 μm average axial crack opening; (b) a specimen with $\alpha = 22.5°$

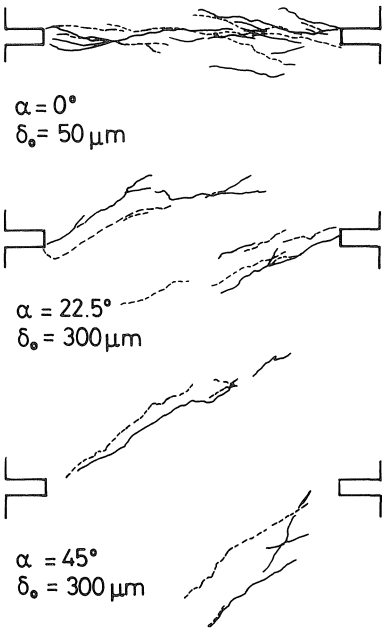

Fig. 78. Global crack patterns for specimens with different fibre orientations.

loaded up to $\delta_0 = 300$ μm, and subsequently sheared to $P_s = 50$ kN; and (c) $\alpha = 45°$, loaded to $\delta_0 = 300$ μm and sheared to $P_s = 50$ kN. The full lines are the cracks detected at the front side of the specimen, the dashed lines are the cracks at the back face.
Of these three specimens, the only one that could be failed in shear (which means that the P_s-δ_s curve has a peak load) is the $\alpha = 0°$ specimen. Initially a set of tensile crack branches developed, more or less perpendicular to the tensile direction. These cracks developed between the notches only. Under shear the different crack branches coalesced, and a number of inclined shear cracks developed between the notches (Fig. 78a). Note that this response resembles the recent results of Arslan et al. [35] on conventional steel fibre and polypropylene fibre reinforced cements, see Fig. 14.
The two other specimens showed that the cracks caused by the tensile loading followed more or less the direction of the steel fibres. In both specimens, inclined tensile cracks developed as shown in Figs. 78b and c. In some of the 45° specimens, the inclined cracks would propagate until they reached the specimen/loading platen interface. Further loading would then normally lead to glue fractures. Under shear, the inclined cracks were simply closed, and even with the QUESTAR long distance crack microscope, no crack initiation and growth was found under shearing. This latter observation is supported by the P_s-δ_s curves for the 45° fibre orientations that are shown in Fig. 79. In this figure results of six 45° tests are shown. The specimens were sheared off at different

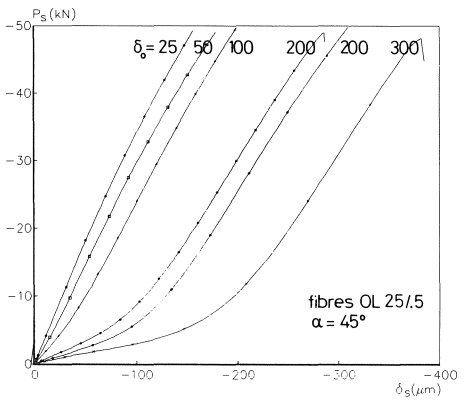

Fig. 79. P_s-δ_s diagrams for 45° OL specimens preloaded to different axial deformations.

axial crack openings, ranging from 25 to 300 μm. The P_s-δ_s curve for $\delta_0 = 25$ μm is almost straight near the origin, and curves gently away from the P_s-axis. When the axial crack opening increases, an increasingly more important contact effect is observed. Especially for the 300 μm test, the initial run in the curve is extremely large, and is correlated to the closure of the inclined tensile cracks (Fig. 78c). The curves of Fig. 80 show that similar phenomena occured in the specimens with ZL fibres. In the ZL tests with $\delta_0 = 50$ and 100 μm, glue fracture occurred. This can be seen from Fig. 80: the respective P_s-δ_s curves show a discontinuity at a relatively small load of -40 kN.

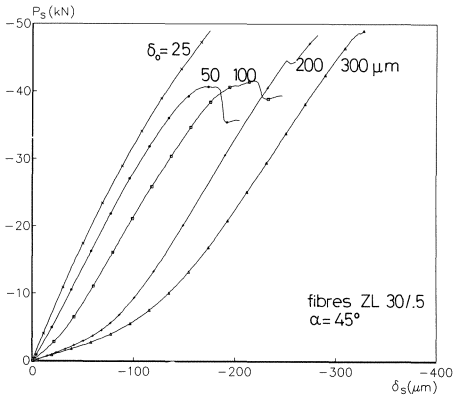

Fig. 80. P_s-δ_s diagrams for 45° ZL specimens preloaded to different axial deformations.

The effect of fibre orientation on the P-δ response (tension, see Figs. 74 through 76) resembles the effect of external confinement in triaxially loaded concrete. In Fig. 81, results obtained by Jamet et al. [60] of displacement controlled triaxial tests on cilinders made of a microconcrete are shown. Increasing the lateral confinement leads to an increase of axial "strength" and an increased ductility. The resemblance with the current experiments is very large, and the steel fibres seem to act as an internal confinement as soon as the concrete is cracked. This was suggested earlier by Yin et al. [36] for explaining the rather ductile response of biaxially loaded conventional steel fibre concrete. The global effect seems similar, irrespective of the presence of an internal or an external confinement. Of course, the agreement is based on a global comparison only but seems promissing enough to elaborate further in future.

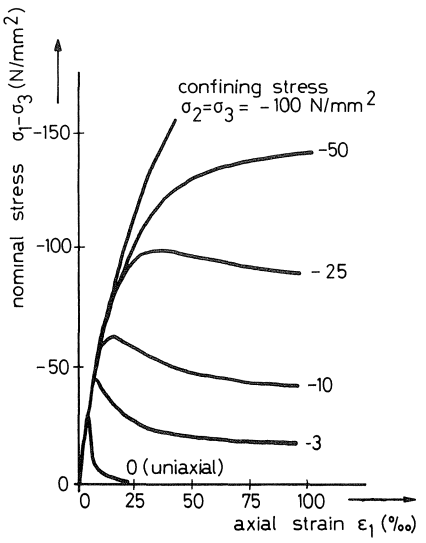

Fig. 81. Results of displacement controlled triaxial compression tests of Jamet et al. [60].

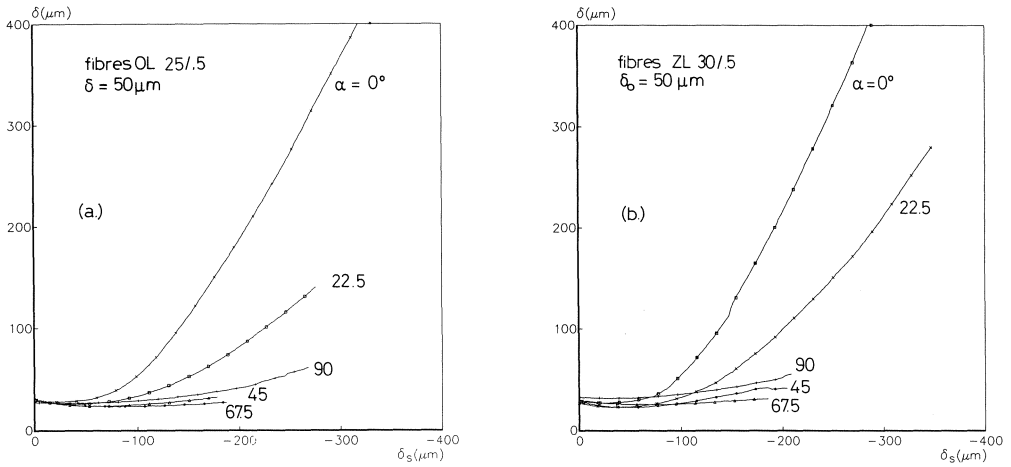

Fig. 82. δ-δ_s plots for experiments with different fibre orientations; $\delta_0 = 50$ μm; (a) OL fibres; (b) ZL fibres.

The resemblance between the tensile behaviour of SIFCON with inclined fibres and concrete loaded under confined conditions in compression is also observed in dilatancy plots $\delta - \delta_s$. The curves of Figs. 82a and b are qualitatively very much in agreement with the $u_1 - u_2$ and $u_1 - u_3$ plots observed in displacement controlled true triaxial compression tests (see Fig. 83, after [33]).

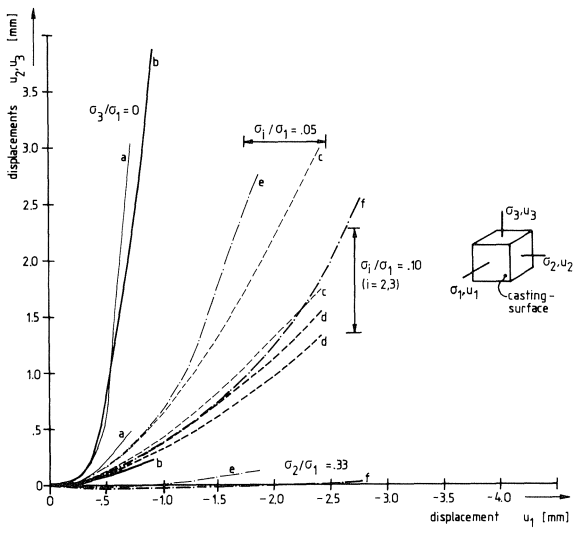

Fig. 83. Dilatancy plots (u_1-u_2 and u_1-u_3) obtained from displacement controlled true triaxial cube tests, after [33]. u_1, u_2 and u_3 are the displacements in the three principal loading directions.

5.5 *Crack patterns*

Next to the global crack patterns, crack growth was monitored under load in a few tests. To this end the recently acquired QUESTAR Remote Controlled Measurement System of the Stevin Laboratory was used. It consists of a high resolution optical microscope on a heavy stable floor stand. The microscope is fixed to a craddle which can be moved with stepper motors in three orthogonal directions. Connected to the microscope (QM-100) is a SONY 77-CE CCD-camera and a high resolution monitor. The CCD technique allows for digital conversion of the images. The maximum resolution is 1.1 μm. The total set-up is shown in Fig. 84. Up till now the microscope has been used successfully in

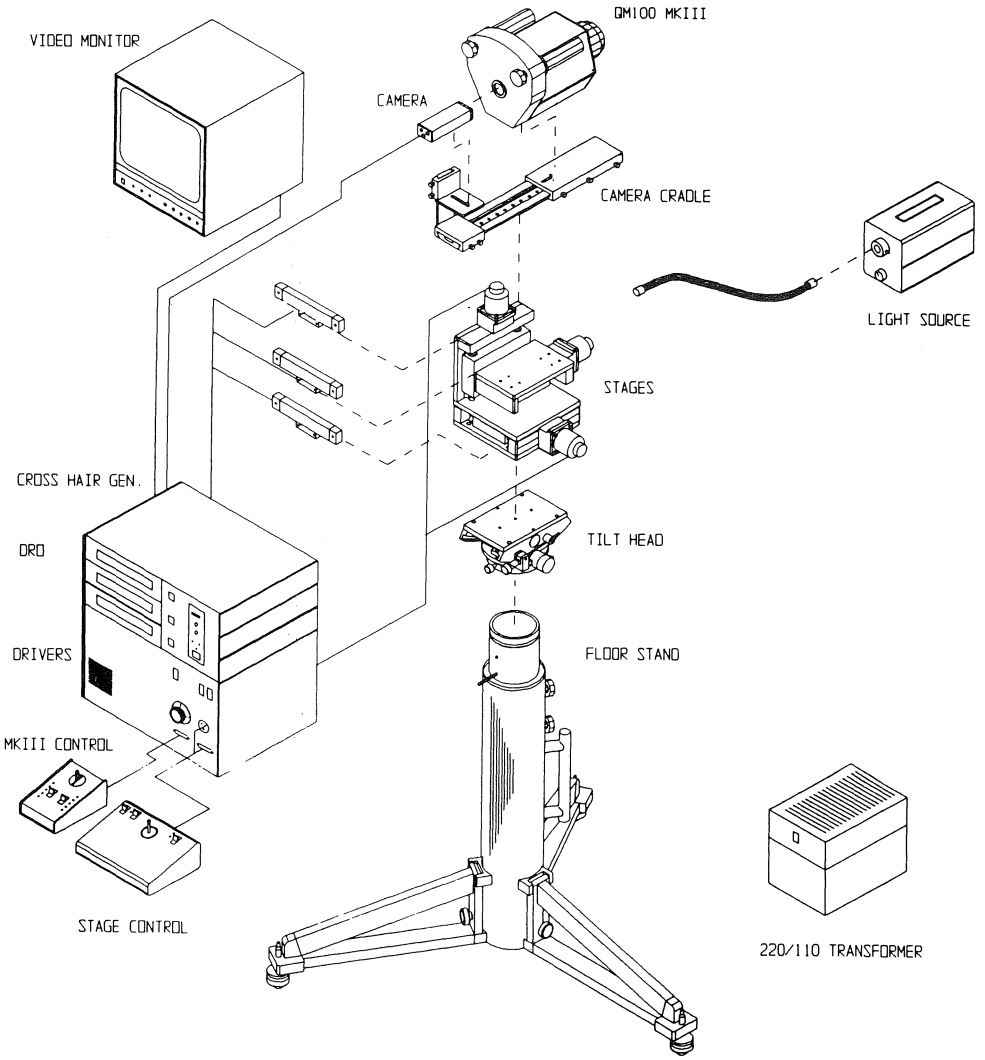

Fig. 84. Overview of the QUESTAR long distance microscope QM 100.

monitoring crack growth in uniaxially loaded concrete specimens (see [19, 20]). More specifically the failure of crack face bridges has been observed under loading. Before viewing a specimen, it is carefully polished. The surface is lit by two flexible light sources as shown in Fig. 84. In order to identify the scan area, small markers are glued to the surface before a test. These are then used as reference points, for example for deformation measurements.
The same technique has been used for the SIFCON specimens. Not the maximum resolution was used, but rather a somewhat smaller resolution of appr. 5 μm, which allowed a somewhat larger field of view. Several specimens were viewed under load, a summary of these tests is given in Table 7.

Table 7. Crack detection experiments

specimen No.	fibre type	δ [μm]	α [deg]	type of detection	number of surface scans
0502	ZL	10	0	global	2
0501	ZL	150	0	near notch	3
1205	OL	100	45	near notch	3
1602	ZL	100	22.5	local (4 spots)	5

The results of the first three tests are most interesting and are shown below. The fourth test confirmed the other observations.

5.5.1 Shear cracks

The first test, No. 0502, was one of the specimens of the preliminary series on ZL fibres, see [57]. This particular specimen was sheared off at a very small axial crack opening of 10 μm. The P-δ and P_s-δ_s diagrams of this experiment are shown in Fig. 85. The load-displacement diagrams are compared to a similar specimen loaded monotonically to failure (0901). A large part of the specimen was scanned at two different moments: (a) at a shear deformation of – 135.9 μm, and (b) at a shear deformation of – 261.4 μm. The crack patterns are shown in Fig. 86. The two photoscans are near the right notch of the specimen, and each of them was assembled from 36 individual photographs. The crack patterns were traced from the photomosaic. Note that the photographs contained much more information. For example sand particles, pores and fibres could easily be identified at the surface. For the sake of clarity all this information is retained here; only the contours of fibres and pores are shown. Note that the surface was carefully polished before a test. Because of this polishing, even suface uplift due to cracking was observed. In Fig. 86, the tensile loading direction is vertical. Shear was applied in the horizontal direction. Pulling the specimen to an average axial deformation of 10 μm caused no observable cracking. The inclined cracks of Fig. 86a and b all developed during shear loading. The second steps lead to a more dense crack pattern, but the inclination of the cracks remained unchanged. In the lower part of the figures crack arrest due to steel

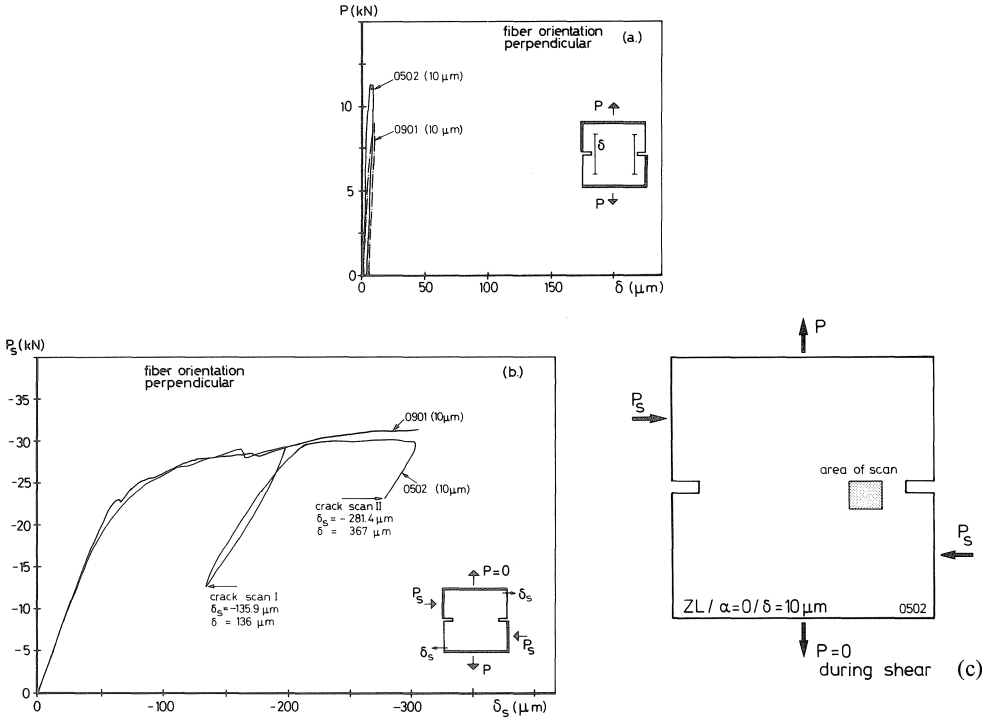

Fig. 85. P-δ (a) and P_s-δ_s (b) plots for two ZL tests with $\delta_0 = 10$ μm. In the experiment labeled 0502 cracking was monitored with the QUESTAR system. At the two points indicated in Fig. b crack scans were made; the area of scan is given in Fig. c.

fibres is observed. The lower inclined crack extended until it reached the fibre. Subsequently it propagated further in the direction of the fibre and finally extended in the original direction in the slurry.

These figures show *for the first time* the development of a "macroscopic shear crack" defined as an array of inclined tensile cracks in a narrow zone [25]. The presence of the fibres prevented the gowth of secondary cracking in other parts of the specimen, and the shear crack remained between the notches. Undoubtedly the redistribution of stresses caused by the fibres is the reason for this behaviour.

5.5.2 Crack coalescence

Another interesting crack mode was found in a ZL specimen loaded intension up to an average axial crack opening of 150 μm before shearing. The P-δ and P_s-δ_s diagrams of this experiment (0501) are shown in Fig. 87. Two crack patterns are shown in Fig. 88. In Fig. 88a, the specimen is loaded in displacement control to $\delta = 147.3$ μm. At this stage a large number of tensile cracks had developed between the notches. Fig. 88a shows a number of these crack branches near the right notch of the specimen. The lower right

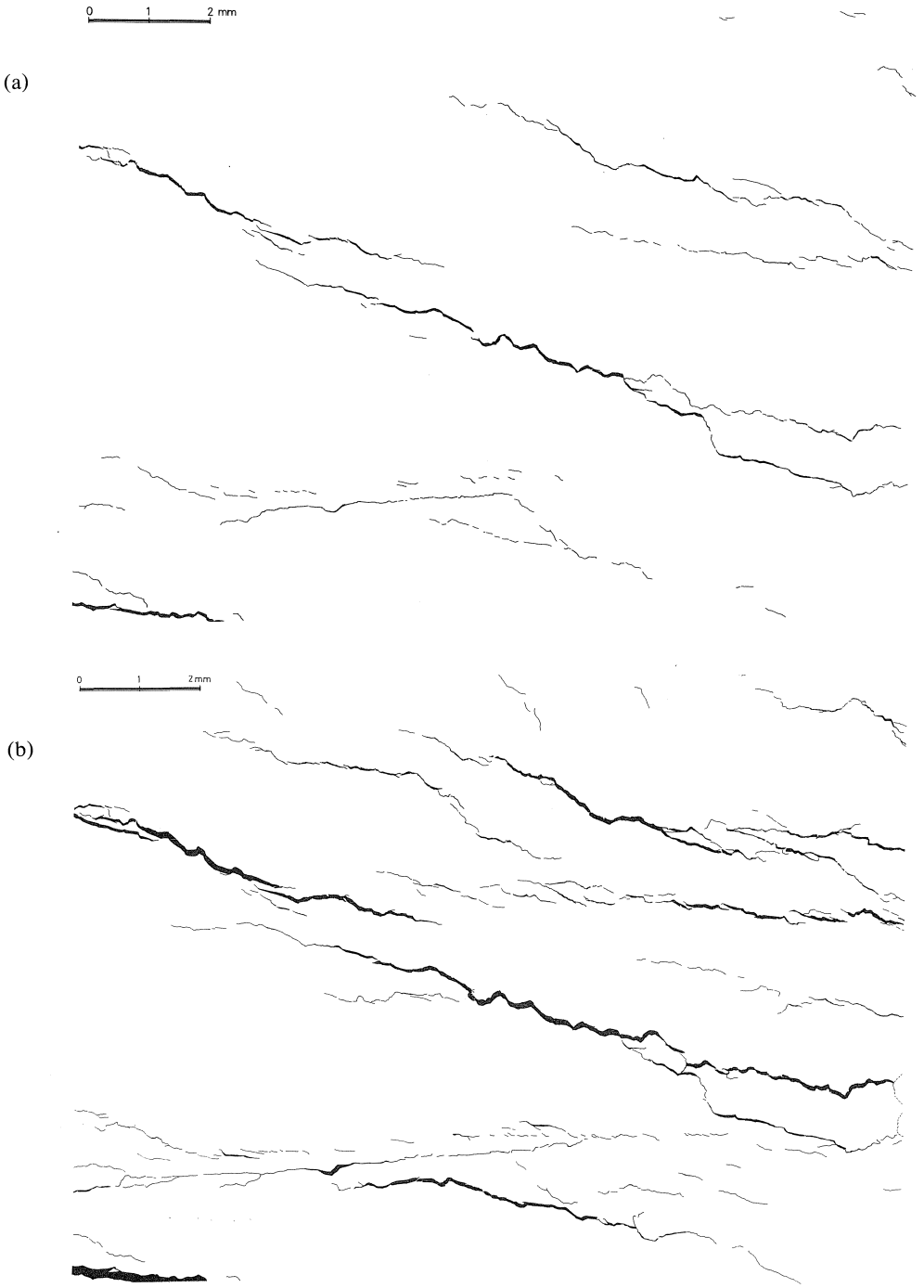

Fig. 86. (a) Cracking in ZL test 0502 ($\delta_0 = 10$ μm) after shearing to $\delta_s = -135.9$ μm, $\delta = 136$ μm; (b) idem after shear to $\delta_s = -261.4$ μm and $\delta = 367$ μm.

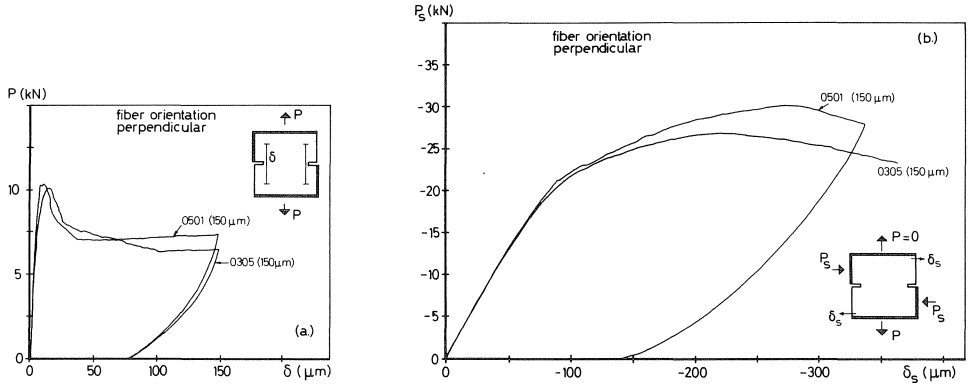

Fig. 87. P-δ and P_s-δ_s plots for two ZL tests with $\delta_0 = 150$ μm. In the experiment labeled 0501 cracking was monitored with the QUESTAR system.

crack passed through two pores. Also the figure contains a good example of crack growth along a fibre near the surface. When shear was applied (Fig. 88b), several of the tensile cracks closed, and an inclined crack developed through coalescence of the individual tensile crack branches. Several of these examples were found in the specimen. At some stage during the shearing crack closure is accompanied by sliding. The crack in Fig. 88b closed partly ($\delta = 127.5$ μm). This behaviour can be observed from the dilatancy plots as well.

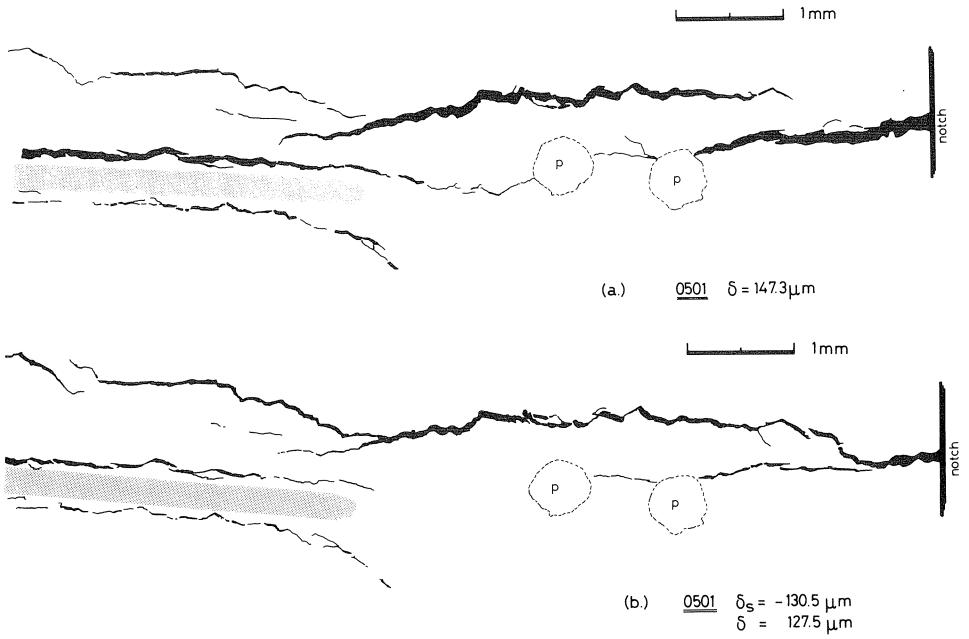

Fig. 88. (a) Crack patterns in specimen 0501 after tensile unloading ($\delta = 147.3$ μm); and (b) idem after shearing to $\delta_s = -130$ μm and $\delta = 127.5$ μm.

5.5.3 Crack closure

The last example of crack monitoring is shown in Fig. 89. In these three crack scans, taken at different stages of loading, the development and closure of an inclined crack in a ZL specimen with a 45° fibre system was followed. The crack pattern of Fig. 89a was taken when the specimen was unloaded after the tensile pre-loading to 100 μm (specimen No. 1205, the P-δ and P_s-δ_s diagrams are similar to the one presented in Fig. 76 for the 45° specimen). The other two crack graphs show the closure of the inclined crack when shear load was applied, respectively at $\delta_s = -49.4$ and -109.1 μm. During this shearing absolutely no cracking was detected in other parts of the specimen. Note that the surface was scanned continuously with the QUESTAR during the entire test. This point is confirmed by the almost straight P_s-δ_s diagram (Fig. 76b), indicating that no energy release due to cracking can have taken place.

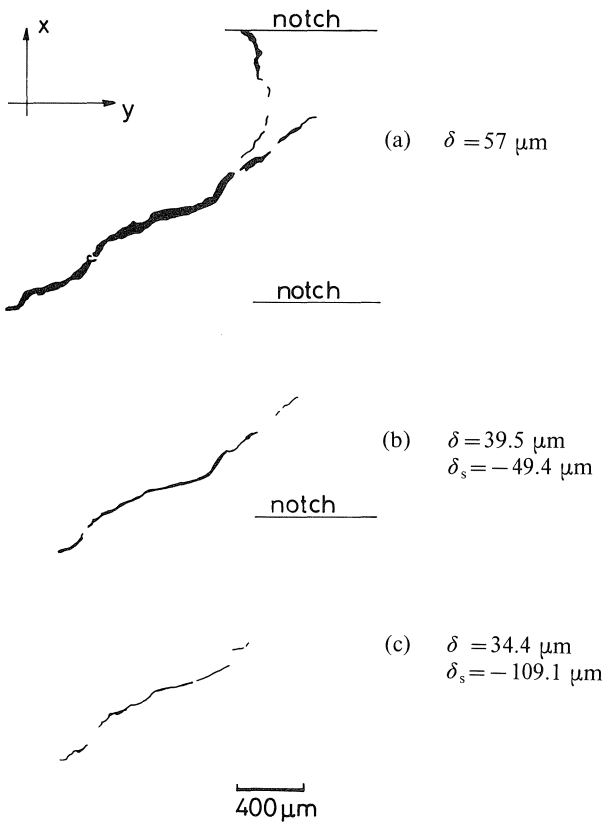

Fig. 89. Crack growth in a ZL specimen with 45° inclined fibres (specimen 1205, $\delta_0 = 100$ μm); (a) after tensile unloading, $\delta = 57$ μm; (b) after shear to $\delta_s = -49.4$ μm; and (c) after shear to $\delta_s = -109.1$ μm.

6 Shear stiffness

In this chapter the first steps in analysing the shear behaviour of concrete specimens with narrow cracks is given. The analysis is far from complete. A comparison is made between the present experimental results and conventional aggregate interlock tests. The shear stiffness results of the plain concrete and SIFCON experiments are presented, and debated in relation to formulations frequently used in smeared crack analyses of concrete structures.

6.1 *Comparison with aggregate interlock experiments*

Shear transfer in rough cracks through aggregate interlock has been thoroughly investigated in the late seventies. Shear forces can be transmitted over a tensile crack due to interlocking of protruding aggregates from the crack interfaces. A fairly large amount of experiments has been carried out in the past, and several models have been developed which can describe the observed phenomena, e.g. [31, 61]. Several of the models were recently implemented in the DIANA finite element code and tested by Feenstra et al. [62]. One of their conclusions was that the models are in reasonable agreement with experimental results. However the scatter was relatively large, especially at small crack openings.

In the conventional aggregate interlock experiments, researchers have maintained the following boundary conditions in their experiments: (1) constant restraining stiffness normal to the crack plane, (2) a constant restraining force normal to the crack plane, and (3) a constant crack width. According to Millard and Johnson [63, 64], maintaining a constant restraint stiffness normal to the crack resembles the situation in reinforced concrete structures. Conducting tests with a constant restraining force would lead to an unrealistic amount of dilatancy. Also they mention that the third boundary condition, constant crack width, would be unrealistic because crushing of the crack interfaces in contact would prevail. Especially the cement matrix surrounding the stiff aggregate particles would be susceptible to crushing when the crack width is kept constant.

The present load-path 3 experiments can be used for a comparison with the aggregate interlock tests conducted under boundary condition 2. Both plain concrete and SIFCON double edge notched square plates were loaded according to load-path 3. In these tests, either a constant confinement of 0 kN or -1 kN (-0.13 MPa) was kept normal to the cracks during shear. The specimens were pre-cracked in displacement control, before applying the shear load. The present tests provide for an important extension of the conventional aggregate interlock experiments. The main difference is that in the present experiments, extremely narrow cracks are studied that are still able of transfer of tensile stresses normal to the crack plane. In the conventional aggregate interlock experiments [31, 65], the crack was made in a rather uncontrolled manner, and after splitting, the crack width was adjusted to the prescribed value. After this splitting procedure, the exact lateral boundary condition was set, and the specimen was sheared off. Results of two aggregate interlock experiments from [31] are shown in Fig. 90. The loading history before shearing is not known in detail. This part has been shown as a

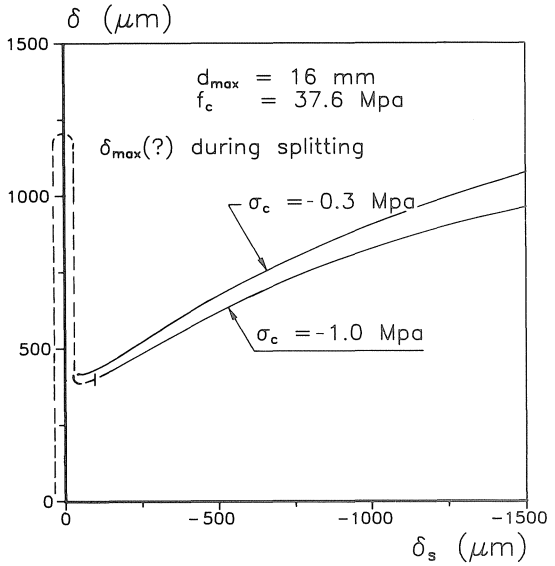

Fig. 90. Crack opening paths for two aggregate interlock experiments with external restraining bars, after [31].

dashed loop along the δ-axis. In the experiments of Fig. 90, the confinement normal to the crack plane was applied through a device with external restraining bars. The restraint was introduced by prestressing the bars. The results of Fig. 90 indicate that sliding is accompanied by crack opening. This dilatant effect is larger for smaller confining stresses.

The specimens in the biaxial machine were precracked in displacement control. This allowed for controlled shear testing of specimens that were still in the softening regime. As discussed in chapter 4, load-path 3 experiments were carried out on three different materials. One of these materials was a 16 mm normal concrete, almost identical to the 16 mm mix that was tested by Walraven (see Fig. 90). Therefore, a comparison of crack opening paths is allowed, and Fig. 91 shows the δ-δ_s paths for two load-path 3 experiments with 0 and -0.13 MPa axial confinement respectively. Comparison with Walraven's experiments shows that the loading range is extremely small in the present tests. Yet, the tensile capacity of the crack is exactly known. Note that in Walraven's experiments no information is available at small values of shear slip. For the experiment with -1 MPa confinement, no information regarding the crack opening during slip up to 70 μm was given. This is the range which can be tested now.

The experiments of Fig. 90 showed an increase of axial crack opening with decreasing confinement. The present load-path 3 results should therefore fall above the results of Walraven. Instead, an opposite trend was observed, which may be caused by differences in shear transfer in the conventional aggregate interlock tests and the present carefully controlled experiments. The above differences may explain why Feenstra et al. [62] found a relatively large scatter for small cracks. Clearly the conventional theories were derived for larger stress free cracks (no softening), and the assumed physical mecha-

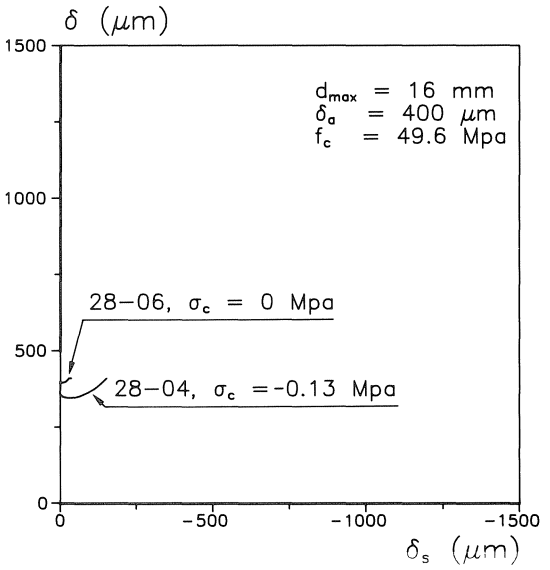

Fig. 91. Crack opening paths δ-δ_s from two load-path 3 experiments on 16 mm normal concrete.

nisms cannot be simply transfered to narrow cracks. For example the occurrence of splitting tensile cracks and secondary diagonal cracking are phenomena which are completely overlooked in the conventional models. Of course, the insight has increased over the years and the models must be adjusted.

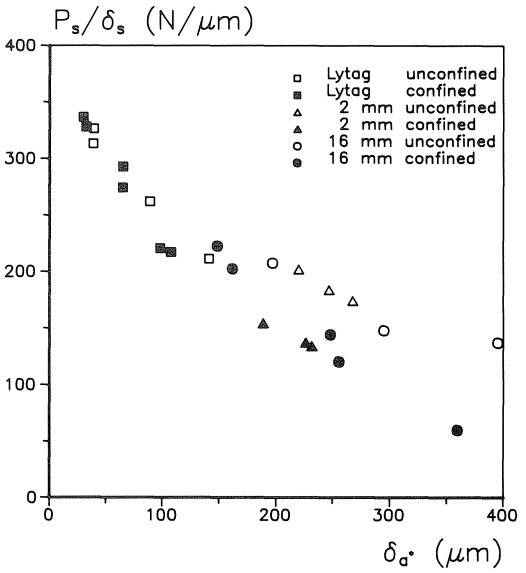

Fig. 92. Decrease of shear stiffness with increasing axial crack opening for the three plain concretes tested.

6.2 *Shear stiffness reduction*

6.2.1 Plain concrete

In Fig. 92, the decrease of shear stiffness P_s/δ_s is shown as a function of the axial crack opening after unloading (denoted as δ_0^*). The shear stiffness is defined as the secant modulus between 10 and 30% of the maximum shear load $P_{s,max}$. Note that the δ_0^* values are smaller than the δ_0 values, which lie on the descending branch of the *P*- δ curves. In Fig. 92, the results of all successful tests are included (see Table 4), thus irrespective of the material composition. A decreasing shear stiffness is observed with increasing crack opening. The difference between the three different materials seems not very pronounced. All tests follow the same trend, except that the secant shear modulus seems to decrease with increasing confinement normal to the crack plane, especially at larger crack openings. Part of this may be explained from the fact that the unloading displacement δ_0^* decreases with an increase of confining stress. Therefore the data points for the confined tests are shifted to the right side of the graph.

6.2.2 SIFCON

For SIFCON only unconfined experiments have been carried out (load-path 3a). Note however that now fibres are present, which may be regarded as an internal confinement as argued before in chapter 5. The problem is of course to determine the level of this internal confinement. In Fig. 93, the shear stiffness is defined as

$$G = \tau/\gamma = (P_s * h)/(A * \delta_{sc}) \tag{6.1}$$

where h is the width of the crack band, and δ_{sc} the shear displacement of the crack-zone. The shear displacement in the crack band is equal to the total shear displacement δ_s

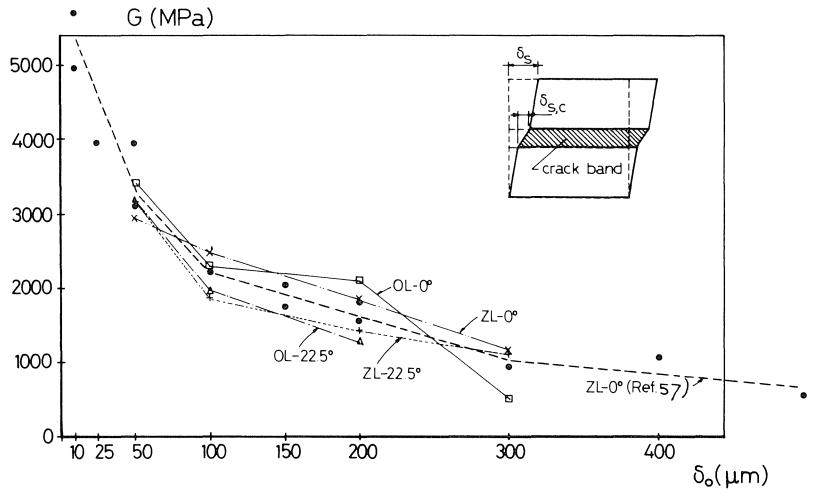

Fig. 93. Shear stiffness of SIFCON at various axial crack openings.

measured in the experiments minus the elastic shear deformations outside the crack band. In the present analysis, the crack band width was taken $h = 15$ mm, which corresponds to the average width of the crack zone observed in the experiments with $\alpha = 0°$. Note that a continuum formulation seems possible for the SIFCON, whereas this is not allowed in the case of plain concrete where cracking leads to localised deformations. This latter point poses an extremely difficult problem for smeared crack approaches as will be discussed in section 6.3

In Fig. 93, the shear stiffnesses for all SIFCON experiments that were presented in chapter 5 are included. Note that only those results for $\alpha = 0°$ and $\alpha = 22.5°$ are included. In these experiments the notion of a crack band seemed to make some sense, whereas the specimens with higher values of α, failed through diagonal cracking (see Fig. 78). The bold dashed line connects the data points that were obtained from the preliminary SIFCON experiments that were published in [57]. The same tendency as observed before for plain concrete is found: the shear stiffness decreases with increasing crack opening. The shear stiffness is however much higher than in the case of plain concrete, which can be explained from fibre bridging in the crack. The type of fibre (viz. Dramix OL or ZL) had no significant effect on the shear stiffness, as was mentioned before. Fig. 93 shows clearly that this parameter has no effect. Likely, the type of fibre will be more important when fibres are pulled out of the matrix. Obviously, this stage was not reached in the present experiments.

6.3 *Shear retention factor*

In computational models based on finite element method, often the smeared crack concept is used for analysing the behaviour of reinforced concrete structures. In these smeared models, a shear retention factor β is introduced to adapt the shear stiffnesss of cracked concrete. Based on the aggregate interlock experiments of Paulay and Loeber [66], Rots [67] derived the following expression for the shear retention factor β:

$$\beta = 1/1 + 4447\varepsilon_{nn} \tag{6.2}$$

where ε_{nn} is the crack strain normal to the crack plane. This relation was derived for small shear displacements, viz. not exceeding 200 μm. A similar equation was derived by Bažant and Gambarova [61]:

$$\beta = 1/(4762\varepsilon_{nn}) - 1/(1346\sqrt{\varepsilon_{nn}}) \tag{6.3}$$

The two expressions are not very different as they were both tuned on Paulay and Loeber's experiments.

More recently, Pruijssers [68] derived an expression for β which is dependent not only on the normal crack strain ε_{nn}, but also on the ratio ε_{nn}/γ:

$$\beta = 1/(P * \varepsilon_{nn} + 1) \tag{6.4a}$$

where

$$P = 2500/[D_{max}^{0.14}(0.76 - 0.16\varepsilon_{nn}/\gamma(1 - \exp(-6\gamma/\varepsilon_{nn})))] \tag{6.4b}$$

where D_{max} is the maximum aggregate size. The shear retention factor according to equation (6.4) is shown in Fig. 94 for different ratios ε_{nn}/γ. For $\varepsilon_{nn}/\gamma = 3$, the formulation of Rots is retrieved.

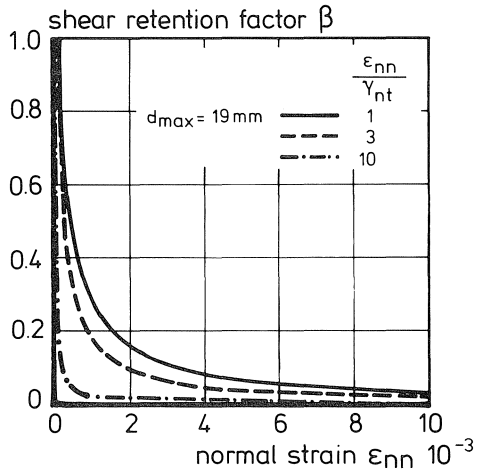

Fig. 94. Shear retention factor β for different values of ε_{nn}/γ, after [68].

A direct comparison between β-values predicted by the above formulations and values obtained from experiments seems however impossible. In the plain concrete experiments, a localized crack forms, which is subjected to shear. The definition of a normal crack strain ε_{nn} and a shear crack strain γ depends on a definition of the crack band width h. This value is not constant during the fracturing process as shown both experimentally, [17, 18], and numerically [20]. In continuum formulations for localized cracking, such as for example the non-local theory [69], different values of h are proposed ranging between 1.88 and 3. In view of the above formulations, any value of β can be obtained by selecting a particular value of h (see [5]). Therefore a comparison between the present plain concrete experiments and the existing formulations of β seems not very valuable.

Then what to do? The experimental technique has now been brought to a sufficiently high level. This has taken the past four years, and in order to come to a better understanding of the shear behaviour, and the development of a new theory which includes all observed phenomena, further research is required. A promising tool which can be used is the recently developed lattice model [20]. Using this model, the micromechanisms of mode I fracture (see Fig. 8), as well as the growth of curved mixed mode cracks can be simulated very well (see [30]). Problems encountered in conventional smeared crack models are circumvented and it would be interesting to extend the existing formulation for shear friction. The model, if successfully extended, could well be used for developing a macroscopic theory for aggregate interlock, and perhaps also for shear fracture. This latter aspect can likely be handeled because at a lower level shear fracture seems merely a mode I problem.

7 Conclusions

Biaxial tension/shear experiments have been carried out on plain concrete and SIFCON mixes. The experiments were conducted on square plates with a constant thickness of 50 mm, but with varying dimensions. A unique feature of the test technique is that specimens can be loaded independently in displacement control both in the tensile and shear direction in the biaxial machine. The experiments can broadly be subdivided into two catagories. First, experiments have been carried out on specimens that were carefully precracked in displacement control. This allowed for the determination of the shear stiffness of concrete containing narrow cracks that were still capable of transferring tensile stresses normal to the crack. The second catagory are experiments where a combination of shear and tension is applied to uncracked specimens. These latter experiments were carried out in order to come to a better understanding of mode II (shear) fracture in concrete. The following conclusions can be drawn.

1. The complicated testing technique has been developed to a sufficient level where reliable results are obtained.
2. The shear experiments on plain concrete specimens containing narrow cracks showed the occurrence of secondary diagonal cracking and splitting under a variety of boundary conditions. True sliding has been observed only in a number of tests where both the crack width was sufficiently large ($\delta = 250$ μm) and where no confinement was present normal to the crack plane. These results show that the conventional aggregate interlock theories developed in the late seventies, cannot be used anymore in this regime. This conclusion is supported by recent numerical analyses by Feenstra et al. [62].
3. The shear experiments on uncracked plain concrete showed that no true shear failure defined as an array of short inclined cracks can be obtained in the larger specimens. Reducing the specimen size seemed to have a significant effect on the failure mode of the specimen, and in several proportional load-path tests ($\delta/\delta_0 =$ constant) distributed cracking as defined above was observed. These results indicate that an intricate relationship between fracture mode and specimen geometry exists.
4. The dominant failure mode in specimens where shear was applied first was the growth of a set of overlapping (curved) cracks from the two notches. This failure mode occurred probably also in the shear fracture tests of Bažant and Pfeiffer, but can only be found under very well controlled conditions.
5. The shear stiffness of the material decreases with increasing crack opening. The effect seemed independent on the type of material tested: 2 mm mortar, 12 mm lytag and 16 mm normal concrete. The effect of confinement on the shear stiffness of a partly open crack was minimal, at least for the range investigated.
6. The fracturing of plain concrete and mortar under biaxial tension and shear is path dependent.
7. The material structure of the SIFCON was highly ansisotropic. Consequently, shear tests were carried out on specimens with fibre systems that were oriented at various angles to the biaxial loading. True shear failure (defined as an array of short

inclined tensile cracks) has been observed in SIFCON specimens where the fibres are oriented parallel to the shear direction. The shear fractures could develop here because the anisotropic material structure contained oriented weak planes.

8. When the orientation of the fibres is changed, no sliding failures could be obtained in the SIFCON, but rather a set of diagonal cracks would develop from the notches in the main fibre direction. In general these specimens could not be failed in shear in the present experimental set-up.
9. A similar shear stiffness reduction as found for plain concrete was observed for SIFCON. A rapid decrease of shear stiffness is observed for narrow cracks, whereas the decrease diminishes at larger crack openings. The shear stiffness is somewhat higher than that for plain concrete, which may be explained from the fibre bridging.
10. The tensile strength and the shear strength of SIFCON vary significantly with varying fibre orientation. The highest tensile strength is found when the fibres are oriented parallel to the tensile direction; the lowest tensile strength (approximately equal to the tensile strength of the slurry) when the fibres are oriented perpendicular to the tensile loading. The highest shear strength is measured in specimens containing fibres prependicular to the shear loading, a much lower shear strength (appr. 10–12% of f_{cc}) is measured when the fibres are alligned with the shear load.
11. The SIFCON behaves considerably more ductile than the plain slurry or plain concrete. The fibres can be regarded as an internal confinement, and the response resembles the behaviour of confined plain concrete.
12. The results for SIFCON show that all effort should be stored in obtaining randomly oriented fibres in the material. As mentioned in the previous paragraph, the increase in strength in the weakest direction is nil or only moderate in comparison with plain concrete.
13. For further interpretation of the results at small crack openings, and verification and extension of existing aggregate interlock theories, further research is required. Numerical micromechanics [20, 21] seems a useful tool for further developing these macroscopic theories. Main advantage is that machine/specimen interactions can be taken into account in a very simple and straightforward manner.

Acknowledgement

This research was sponsored by the Air Force Office of Scientific Research (AFSC) under contract number F49620-88-C-0135. The United States Government is authorized to reproduce and distribute reprints for governmental purposes notwithstanding any copyright notation hereon. The support of AFSC is gratefully acknowledged.

Notation

a notch depth
d specimen size
f_{cc} compressive strength (150 mm cubes)

f_{spl}	splitting tensile strength (150 mm cubes)
G	shear modulus
P	axial load
P_s	shear load
α	main fibre orientation in SIFCON
β	shear retention factor
δ	global average crack opening (65 mm gauge length)
δ_i	local crack opening (35 mm gauge length)
δ_s	global shear displacement
ε_{nn}	normal crack strain
γ	shear crack strain

References

1. SHAH, S. P., SWARTZ, S. E. and BARR, B. (eds.), Fracture of Concrete and Rock: Recent Developments, Elsevier Applied Science Publishers, London/New York, 1989.
2. SHAH, S. P., SWARTZ, S. E. and Wang, M. L. (eds.), Micromechanics of Fracture of Quasi-Brittle Materials, Elsevier Applied Science Publishers, London/New York, 1990.
3. ELFGREN, L. and SHAH, S. P. (eds.), Analysis of Concrete Structures by Fracture Mechanics, Chapman & Hall, London/New York, 1991.
4. VAN MIER, J. G. M., ROTS, J. G. and BAKKER, A. (eds.), Fracture Processes in Concrete, Rock and Ceramics, (2 Volumes), Chapman & Hall, London/New York, 1991.
5. NOORU-MOHAMED, M. B., PhD Thesis, Delft University of Technology (in preparation).
6. KAPLAN, M. F., Crack Propagation and the Fracture of Concrete, Journal of the American Concrete Institute, Vol. 58, No.5 , 1961, pp. 591-610.
7. HILLERBORG, A., MODEER, M. and PETERSSON, P.-E., Analysis of Crack Formation and Crack Growth in Concrete by means of Fracture Mechanics and Finite Elements, Cement & Concrete Research, Vol. 6, 1976, pp. 773-782.
8. PETERSSON, P.-E., Crack Growth and Development of Fracture Zones in Plain Concrete and Similar Materials, Report TVBM-1006, Lund Institute of Technology, Sweden, 1981.
9. CORNELISSEN, H. A. W., HORDIJK, D. A. and REINHARDT, H. W., Experimental Determination of Crack Softening Characteristics of Normalweight and Lightweight Concrete, HERON, Vol. 31, No. 2, 1986, pp. 45-56.
10. KARIHALOO, B. L. and NALLATHAMBI, P., An Improved Effective Crack Model for the Determination of the Fracture Toughness of Concrete, Cement & Concrete Research, Vol. 19, 1989, pp. 603-610.
11. MINDESS, S., Fracture Process Zone Detection, in Fracture Mechanics Test Methods for Concrete (eds. S. P. Shah and A. Carpinteri), Chapman & Hall, London/New York, 1991, pp. 231-261.
12. VAN MIER, J. G. M. and NOORU-MOHAMED, M. B., Geometrical and Structural Aspects of Concrete Fracture, Engineering Fracture Mechanics, Vol. 35, No. 4/5, 1990, pp. 617-628.
13. HU, X. A. and WITTMANN, F. H., An experimental Method to Determine the Extension of the Fracture Process Zone, Submitted to ASCE, Journal of Materials in Civil Engineering, 1990.
14. BASCOUL, A., KHARCHI, F. and MASO, J. C., Concerning the Measurement of the Fracture Energy of a Micro-Concrete According to the Crack Growth in a Three Points Bending Test on Notched Beams, in Fracture of Concrete and Rock (eds. S. P. Shah and S. E. Swartz), Springer Verlag, New York, 1989, pp. 396-408.
15. SWARTZ, S. E. and REFAI, T., Cracked Surface Revealed by Dye and its Utility in Determining Fracture Parameters, in Fracture Toughness and Fracture Energy (eds. H. Mihashi, H. Takhashi and F. H. Wittmann), Balkema, Rotterdam, 1989, pp. 509-520.
16. VAN MIER, J. G. M., Internal Crack Detection in Single Edge Notched Concrete Plates Subjected to Uniform Boundary Displacement, in Micromechanics of Failure of Quasi-Brittle Materials (eds. S. P. Shah, S. E. Swartz and M. L. Wang), Elsevier Applied Science Publishers, London/New York, 1990, pp. 33-42.
17. VAN MIER, J. G. M., Mode I Fracture of Concrete: Discontinuous Crack Growth and Crack Interface Grain Bridging, Cement & Concrete Research, Vol. 21, No. 1, 1991, pp. 1-15.
18. VAN MIER, J. G. M., Fracture Process Zone in Concrete: A Three Dimensional Growth Process, in Proceedings ECF8 Fracture Behaviour and Design of Materials and Structures (ed. D. Firrao), Vol. 2, EMAS Publishers, UK, 1990, pp. 567-572.
19. VAN MIER, J. G. M., Crack face Bridging in Normal, High Strength and Lytag Concrete, in Fracture Processes in Concrete, Rock and Ceramics (eds. J. G. M. van Mier, J. G. Rots and A. Bakker), Vol. I, Chapman & Hall, London/New York, 1991, pp. 27-40.
20. SCHLANGEN, E. and Van Mier, J. G. M., Experimental and Numerical Analysis of Micromechanisms of Fracture of Cementbased Composites, Report 25.5-91-1/VFC, Delft University of Technology, 1991; also to appear in Cement and Concrete Composites, Special Issue on Micromechanics of Fracture of Cementitious Composites (V.C. Li guest editor), 1991 (in print).

21. VONK, R. A., RUTTEN, H. S., VAN MIER, J. G. M. and FIJNEMAN, H. J., Micromechanical Simulation of Concrete Softening, in Fracture Processes in Concrete, Rock and Ceramics (eds. J. G. M. van Mier, J. G. Rots and A. Bakker), Vol. I, Chapman & Hall, London/New York, 1991, pp. 129–138.
22. GDOUTOS, E. E., Problems of Mixed Mode Crack Propagation, Martinus Nijhoff Publishers, The Hague/Boston/Lancaster, 1984.
23. CARPINTERI, A. and SWARTZ, S. E., Mixed-Mode Crack Propagation in Concrete, Chapter 3 in Fracture Mechanics Test Methods for Concrete (eds. S. P. Shah and A. Carpinteri), Chapman & Hall Publishers, London/New York, 1991, pp. 129–191.
24. HORDIJK, D. A., VAN MIER, J. G. M. and REINHARDT, H. W., Material Properties, Chapter 4 in Fracture Mechanics of Concrete Structures From Theory to Applications (ed. L. Elfgren), Chapman & Hall Publishers, London/New York, 1989, pp. 67–127.
25. BAŽANT, Z. P. and PFEIFFER, P. A., Shear Fracture Tests of Concrete, Materials and Structures (RILEM), Vol. 19, No. 110, 1986, pp. 111–121.
26. INGRAFFEA, A. R. and PANTHAKI, M. J., Analysis of Shear Fracture Tests of Concrete Beams, in Finite Element Analysis of Reinforced Concrete Structures, Tokyo, Japan, 1985, pp. 151–173.
27. SWARTZ, S. E. AND TAHA, N. M., Mixed Mode Crack Propagation and Fracture in Concrete, Engineering Fracture Mechanics, Vol. 35, No. 1/2/3, 1990, pp. 137–144.
28. CARPINTERI, A., FERRARA, G., MELCHIORRI, G. and VALENTE, S., The Four Point Shear Test on Single Notched Specimens: an Experimental and Numerical Analysis, in Fracture Behaviour and Design of Materials and Structures (ed. D. Firrao), EMAS Publishers, UK, 1990, pp. 667–675.
29. SCHLANGEN, E. and VAN MIER, J. G. M., A FE-supported Investigation of Mixed Mode Fracture in Concrete, in Proceedings of the 9th International Conference on Experimental Mechanics, Technical University of Copenhagen, Aaby Trick Publishers, 1990, pp. 1403–1412.
30. SCHLANGEN, E. and VAN MIER, J. G. M., Boundary Effects in Mixed Mode I and II Fracture of Concrete, in Fracture Processes in Concrete, Rock and Ceramics (eds. J. G. M. van Mier, J. G. Rots and A. Bakker), Vol. II, Chapman & Hall Publishers, London/New York, 1991, pp. 705–716.
31. WALRAVEN, J. C., Aggregate Interlock. A Theoretical and Experimental Analysis, PhD Thesis, Delft University of Technology, 1980.
32. DAVIES, J., Numerical and Experimental Study of Development of Fracture Path under Mixed Mode Loading, in Fracture Processes in Concrete, Rock and Ceramics (eds. J. G. M. van Mier, J. G. Rots and A. Bakker), Vol. II, Chapman & Hall Publishers, London/New York, 1991, pp. 717–726.
33. VAN MIER, J. G. M., Fracture of Concrete under Complex Stress, HERON, Vol. 31, No. 3, 1986, pp. 1–90.
34. LUONG, M. P., Measuring Toughness Indices on Brittle Materials, in Fracture Processes in Concrete, Rock and Ceramics (eds. J. G. M. van Mier, J. G. Rots and A. Bakker), Vol. II, Chapman & Hall Publishers, London/New York, 1991, pp. 727–736.
35. ARSLAN, A., HUGHES, T. G. and BARR, B. I. G., Mixed Mode Fracture Including Torsion in a New Compact Test Specimen Geometry, in Fracture Processes in Concrete, Rock and Ceramics (eds. J. G. M. van Mier, J. G. Rots and A. Bakker), Vol. II, Chapman & Hall Publishers, London/New York, 1991, pp. 737–746.
36. YIN, W. S., SU, E. C. M., MANSUR, M. A. and HSU, T. T. C., Fibre Reinforced Concrete under Biaxial Compression, Engineering Fracture Mechanics, Vol. 35, No. 1/2/3, 1990, pp. 261–268.
37. VAN MIER, J. G. M. and TIMMERS, G., Shear Fracture in Slurry Infiltrated Fibre Concrete (SIFCON), in Pre-Proceedings RILEM/ACI Workshop on High Performance Fiber Reinforced Cement Composites (eds. H. W. Reinhardt and A. E. Naaman), University of Stuttgart, 1991, pp. 253–265.
38. VAN MIER, J. G. M., Strain Softening of Concrete under Multiaxial Conditions, PhD Thesis, Eindhoven University of Technology, 1984.
39. REINHARDT, H. W., CORNELISSEN, H. A. W. and HORDIJK, D. A., Mixed Mode Fracture Tests

on Concrete, in Fracture of Concrete and Rock (eds. S. P. Shah and S. E. Swartz), Springer Verlag, New York, 1989, pp. 119–130.
40. HORDIJK, D. A. and REINHARDT, H. W., Macro-Structural Effects in a Uniaxial Tensile Test on Concrete, in Brittle Matrix Composites 2 (eds. A. M. Brandt and I. H. Marshall), Elsevier Applied Science Publishers, London/New York, 1989, pp. 486–495.
41. FANPING ZHOU, Some Aspects of Tensile Fracture Behaviour and Structural Response of Cementitious Materials, Report TVBM 1008, Lund Institute of Technology, Lund, Sweden, 1988.
42. VONK, R. A., Uniformity of Deformations in Compression Tests on Concrete, Report TUE/BKO-89.17, Eindhoven University of Technology, Eindhoven, The Netherlands, 1989.
43. NOORU-MOHAMED, M. B., SCHLANGEN, E. and VAN MIER, J. G. M., Fracture of Concrete Plates Subjected to Rotating Biaxial Stress, in Fracture Behaviour and Design of Materials and Structures (ed. D. Firrao), EMAS Publishers, UK, 1990, pp. 682–687.
44. HORDIJK, D. A., REINHARDT, H. W. and CORNELISSEN, H. A. W., Fracture Mechanics Parameters of Concrete from Uniaxial Tensile Tests as Influenced by Specimen Length, in Proceedings SEM/RILEM Conf. on Fracture of Concrete and Rock (eds. S. P. Shah and S. E. Swartz), Houston (TX), SEM, Bethel, 1987, pp. 138–149.
45. VAN MIER, J. G. M. and SCHLANGEN, E., On the Stability of Softening Systems, in Fracture of Concrete and Rock - Recent Developments (eds. S. P. Shah, S. E. Swartz and B. Barr), Elsevier Applied Science Publishers, London/New York, 1989, pp. 387–396.
46. LANKARD, D. R. and NEWELL, J. K., Preparation of Highly Reinforced Steel Fibre Reinforced Concrete Composites, in Fiber reinforced Concrete (ACI-SP81), American Concrete Institute, Detroit, 1984, pp. 286–306.
47. VAN MIER, J. G. M., Mode I Behaviour of Concrete: Influence of the Rotational Stiffness outside the Crack-Zone, in Analysis of Concrete Structures by Fracture Mechanics (eds. L. Elfgren and S. P. Shah), Chapman & Hall Publishers, London/New York, 1991, pp. 17–30.
48. WATKINS, J. and LIU, K. L. W., A Finite Element Study of the Short Beam Specimen under Mode II Loading, Int. Journal of Cement Composites and Lightweight Concrete, Vol. 7, No. 1, 1985, pp. 39–47.
49. KUPFER, H., Das Verhalten des betons unter mehrachsiger Kurzzeitbelastung unter besonderer Berücksichtigung der zweiachsiger Beanspruchung, Deutscher Ausschuss für Stahlbeton, Heft 229, Teil I, Berlin, 1973.
50. VAN MIER, J. G. M., Fracture Study of Concrete Specimens Subjected to Combined Tensile and Shear Loadings, in Proceedings Int'l. Conference on Measurement and Testing in Civil Engineering, (ed. J. F. Jullien), Lyon-Villeurbanne, September 13–16, 1988, Vol. 1, pp. 337–347.
51. NOORU-MOHAMED, M. B. and VAN MIER, J. G. M., Fracture of Concrete under Mixed Mode Loading, in Fracture of Concrete and Rock - Recent Developments (eds. S. P. Shah, S. E. Swartz and B. Barr), Elsevier Applied Science Publishers, London/New York, 1990, pp. 33–42.
52. BAŽANT, Z. P., Size Effect in Blunt Fracture: Concrete, Rock, Metal, J. Eng. Mech. (ASCE), Vol. 110, No. 4, 1984, pp. 518–535.
53. MANDELBROT, B. B., The Fractal Geometry of Nature, W. F. Freeman and Company, New York, 1983.
54. HASSANZADEH, M., Determination of Mixed Mode Properties of Concrete, in Fracture Processes in Concrete, Rock and Ceramics (eds. J. G. M. van Mier, J. G. Rots and A. Bakker), Chapman & Hall, London/New York, 1991, pp. 685–694.
55. HOMRICH, J. R. and NAAMAN, A. E., Stress-Strain Properties of SIFCON in Uniaxial Compression and Tension, Air Force Weapons Laboratory, Final Report AFWL-TR-87-115, August 1988.
56. REINHARDT, H. W. and FRITZ, C., Optimization of SIFCON Mix, in Fibre Reinforced Cements and Concretes - Recent Developments, (eds. R. N. Swamy and B. Barr), Elsevier Applied Science Publishers, London/New York, 1989, pp. 11–21.
57. VAN MIER, J. G. M., Fracture of SIFCON under Combined Tensile and Shearlike Loading, in Proceedings Symposium "O" Fiber Reinforced Cementitious Materials (eds. S. Mindess and J. P. Skalny), Mater. Res. Soc. Fall Meeting 1990, MRS Pittsburgh, Vol. 211, 1991, pp. 215–220.

58. WITTMANN, F. H. and ROELFSTRA, P. E., Constitutive Equations for Transient Conditions, in Proceedings IABSE Colloquium on Computational Mechanics of Concrete Structures - Advances and Applications, Delft, The Netherlands, June 1987, Published by IABSE, Zurich, Vol. 54, 1987, pp. 239–259.
59. HORDIJK, D. A. and REINHARDT, H. W., Fracture of Concrete in Uniaxial Tensile Experiments as Influenced by Curing Conditions, Engineering Fracture Mechanics, Vol. 35, No. 4/5, 1990, pp. 819–826.
60. JAMET, P. MILLARD, A. and NAHAS, G., Triaxial Behaviour of a Microconcrete Complete Stress-Strain Curves for Confining Pressures Ranging from 0 to 100 MPa, in Proceedings RILEM/CEB Symposium Concrete under Multiaxial Conditions, Vol. 1, INSA Toulouse, 1984, pp. 133–140.
61. BAŽANT, Z. P. and GAMBAROVA, P., Rough Cracks in Reinforced Concrete, ASCE, J. Struct. Div., Vol. 106, 1980, pp. 819–842.
62. FEENSTRA, P., DE BORST, R. and ROTS, J.G., Numerical Study on Crack Dilatancy I: Models and Stability Analysis, J. Eng. Mech., ASCE, Vol. 117, No.4, April 1991, pp. 733-769.
63. MILLARD, S. G. and JOHNSON, R. P., Shear Transfer across Cracks in Reinforced Concrete due to Aggregate Interlock and to Dowel Action, Magazine of Concrete Research, Vol. 36, No. 126, 1984, pp. 9–21.
64. MILLARD, S. G. and JOHNSON, R. P., Shear Transfer in Cracked Reinforced Concrete, Magazine of Concrete Research, Vol. 37, No. 130, 1985, pp. 3–15.
65. LAIBLE, J. P., WHITE, R. N. and GERGELY, P., Experimental Investigation of Seismic Shear Transfer across Cracks in Concrete Nuclear Containment Vessels, in ACI Special Publication SP53-9, pp. 203–226.
66. PAULAY, T. and LOEBER, P. S., Shear Transfer by Aggregate Interlock, in Shear in Reinforced Concrete, American Concrete Institute SP-42, Vol. 1, 1974.
67. ROTS, J. G., KUSTERS, G. M. A. and NAUTA, P., Variable Shear Retention Factor for the Shear Resistance of Cracked Concrete, Research Report, Institute TNO for Building Materials and Structures, No. BI-84-33/68.8.2001, 1984 (in Dutch).
68. PRUIJSSERS, A. F., Description of the Stiffness Relation for Mixed-Mode Fracture Problems in Concrete using the Rough-Crack Model of Walraven, TU-Delft Report, Department of Civil Engineering, No. 5-85-2, 1985.
69. BAŽANT, Z. P. and PIJAUDIER-CABOT, G., Measurement of Characteristic Length of Non-local Continuum, J. Eng. Mech. (ASCE), Vol. 115, 1989, pp. 755–767.